## Florida International University
# FIU Digital Commons

10-26-2016

# Improving Current-Asymmetry of Metal-Insulator-Metal Tunnel Junctions

Aparajita Singh
*Florida International University*, asing044@fiu.edu

FLORIDA INTERNATIONAL UNIVERSITY

Miami, Florida

IMPROVING CURRENT-ASYMMETRY OF METAL-INSULATOR-METAL TUNNEL

JUNCTIONS

A dissertation submitted in partial fulfillment of the

requirements for the degree of

DOCTOR OF PHILOSOPHY

in

ELECTRICAL ENGINEERING

by

Aparajita Singh

2016

To:     Interim Dean Ranu Jung
        College of Engineering and Computing

This dissertation, written by Aparajita Singh, and entitled Improving Current-Asymmetry of Metal-Insulator-Metal Tunnel Junctions, having been approved in respect to style and intellectual content, is referred to you for judgment.

We have read this dissertation and recommend that it be approved.

_____
Nezih Pala

_____
Frank Urban

_____
Sakhrat Khizroev

_____
Irene Calizo

_____
Dinesh Sood

_____
Shekhar Bhansali, Major Professor

Date of Defense: October 26, 2016

The dissertation of Aparajita Singh is approved.

_____
Interim Dean Ranu Jung
College of Engineering and Computing

_____
Andrés G. Gil
Vice President for Research and Economic Development
and Dean of the University Graduate School

Florida International University, 2016

DEDICATION

To my parents, Mrs. Kiran Singh and Dr. Shamsher B. Singh

And, my little brother, Sneh Vardhan.

ACKNOWLEDGMENTS

ABSTRACT OF THE DISSERTATION

IMPROVING CURRENT-ASYMMETRY OF METAL-INSULATOR-METAL TUNNEL

JUNCTIONS

by

Aparajita Singh

Florida International University, 2016

Miami, Florida

Professor Shekhar Bhansali, Major Professor

In this research, Ni–NiOx–Cr and Ni–NiOx–ZnO–Cr metal-insulator-metal (MIM) junction based tunnel diodes have been investigated for the purpose of a wide-band detector. An MIM diode has a multitude of applications such as harmonic mixers, rectifiers, millimeter wave and infrared detectors. Femtosecond-fast electron transport in MIM tunnel diodes also makes them attractive for energy-harvesting devices. These applications require the tunnel diodes to have high current-asymmetry and non-linear current-voltage behavior at low applied voltages and high frequencies. Asymmetric and non-linear characteristics of Ni–NiOx-Cr MIM tunnel diodes were enhanced in this research by the addition of ZnO as a second insulator layer in the MIM junction to form metal-insulator-insulator-metal (MIIM) structure.

Electrical characteristics were studied in a voltage range of $\pm 0.5 V$ for the single-insulator Ni–NiOx–Cr and double-insulator Ni–NiOx–ZnO–Cr tunnel diodes. Since the electrical characteristics of the diode are sensitive to material selection, material arrangement, thickness, deposition techniques and conditions, understanding the diode behavior with respect to these factors is crucial to developing a robust diode structure. Thus, ZnO insulator layer in MIIM

junction was deposited by two different techniques: sputtering and atomic layer deposition (ALD). Also, the optical properties were characterized for the sputter deposited NiOx insulator layers by ellipsometry and the impact of annealing was explored for the NiOx optical properties.

The Ni–NiOx–Cr MIM tunnel diodes provide low resistance but exhibit a low (~1) current-asymmetry. Asymmetry increased by an order of magnitude in case of Ni–NiOx–ZnO–Cr MIIM tunnel diode. The sensitivity of the MIM and MIIM diodes was 11 $V^{-1}$ and 16 $V^{-1}$, respectively. The results suggest that the MIIM diode can provide improved asymmetry at low voltages. The tunneling behavior of the device was also demonstrated in the 4-298K temperature range. It is hypothesized that the improved performance of the bilayer insulator diode is due to resonant tunneling enabled by the second insulator. Finally, the MIM and MIIM devices were investigated for wide-band detection up to 50GHz (RF) and 0.3THz (optical).

TABLE OF CONTENTS

LIST OF FIGURES

# 1. INTRODUCTION

A renewed interest in thin film metal-insulator-metal (MIM) tunnel diodes is there for high frequency applications. The tunnel diodes exceeded regular diodes at low voltages due to their high frequency switching speeds and high rate of change of conductance. Metal–insulator–insulator–metal (MIIM) tunnel diode technology is an advancement of the pre-existing MIM technology. MIIM devices have recently shown great potential for rectifiers [1–3], millimeter wave wireless communication [4], and terahertz electronics [5] over the current MIM diodes. These existing applications take advantage of the femtosecond fast transport in MIM tunnel diodes. The efficiency of the MIM diode is crucial to the choice of metals, insulators, material configuration, and diode geometry. A thin film (<10 nm) insulator layer stacked between two metal electrodes forms an MIM tunnel junction. Rectification takes place when electrons tunnel between asymmetric electrodes through the insulator. A current asymmetry can be introduced in the current-voltage response of an MIM by choosing metals with maximum work-function difference. However, achieving the maximum work-function difference cannot be the only reason for the choice of metals, since the metal-insulator interfaces significantly influence the conduction of electrons. Issues such non-uniformity, surface roughness, and pinholes in the insulator alone can lead to non-repeatability in devices. Therefore careful fabrication of the successive metal and insulator layers is vital to the repeatability of the MIM diode's performance. Inconsistencies and complications during thin film deposition parameters, liftoff, and etch can cause non-repeatable device performance.

Despite investigations by many research groups, commercialization of MIM-based electronics has been hindered by a lack of a repeatable, high yield process. In particular, metal-insulator interfacial roughness and oxide stoichiometry has slowed down the technology. Additionally, even with high-quality smooth interfaces, the achievable current asymmetry is limited due to the built in voltage arising from different work functions of the materials at the

1

interface. It has been shown that there is a compromise between the conductivity and current asymmetry in a simple MIM configuration [5]. The addition of another insulator layer, to form metal-insulator-insulator-metal (MIIM) structure, provides improved nonlinearity and asymmetry [6,7] when each insulator has different band gaps and electron affinities. This improvement is due to the different tunneling effects at different bias polarities across the tunnel diodes. Most of the work in literature has focused on resonant tunneling effect. Resonant tunneling can result in greater conductivity while non-linearity is maintained [8]. Step-tunneling is a recent concept which is increasingly being explored [9]. Step-tunneling arises under the opposite bias polarity as compared to that of resonant tunneling and results in a large asymmetry with a sharp turn on. The dominant quantum tunneling defines the nonlinearity under different biases [10].

Despite the various other constraints, such as impedance matching and antenna response, in advancing MIM-based technology for detection in terahertz (THz), infrared (IR), and optical regions; the objective of this research focuses on enhancing the current-asymmetry and optimizing the deposition of thin insulating films which significantly impact the reliability of the MIM tunnel diodes. In an effort to produce tunnel junction devices that exhibit a very high degree of non-linearity and current-asymmetry, the possibility of combining a p-type NiOx film and an n-type ZnO film to form an MIIM has been investigated. In this research, the intrinsic operation of the single-insulator NiOx [11-15] has been compared with double-insulator NiOx/ZnO as a tunneling barrier. The NiOx/ZnO bilayer combination in an MIIM was chosen since it can function as a resonant tunneling diode at high frequencies and as a regular p–n junction tunnel diode at low frequencies. The rectification capabilities of ZnO have been shown to be appropriate for constructing ZnO based p–n and Schottky junctions [16]. The n-type charge carriers in the ZnO layer are known to accumulate at the interface to form a sheet with high conductance [18]. The polar discontinuities at the interfaces aid in generating or removing charge carriers [19]. Such

2

an MIIM produced by other techniques has been reported to give asymmetric and non-linear characteristics [20–23].

## 1.1 Motivation and objectives

The main motivation of this research was to obtain an MIM device with a high efficiency. The specific objectives towards this goal, are as follows:

i.  Characterization of optical properties of thin insulating layers in the growth direction via ellipsometer measurements. Ellipsometer analysis enabled tuning of the dielectric properties and facilitated the characterization of deposition conditions.

ii.  Understand the effect of post-deposition annealing on thin films under oxygen rich environment. The difference in oxygen concentration and depth profile affects the conduction through the thin insulating barrier.

iii.  Current-voltage (I-V) and capacitance-voltage (C-V) measurements to investigate the electrical characteristics of the MIM and MIIM devices. Results of the I-V measurements are fitted with different tunneling models to determine the tunneling mechanism.

iv.  Determine the performance of the MIM tunnel diodes integrated with co-planar waveguide feed and antenna for millimeter wave and THz detection, respectively. The diode performance is a measure of how efficiently it converts an input AC signal to usable DC output.

## 1.2 Dissertation organization

In chapter 2, current state-of-the-art of MIM and MIIM tunnel diodes are presented, with a review of their advantages, shortcomings, and different tunneling mechanisms. The theory of operation of MIM and MIIM diodes is also discussed in the chapter.

Chapter 3 presents the various fabrication methods of MIM diodes including different characterization techniques. The actual diode design and fabrication steps are also elaborated in chapter 4 followed by the detailed description of the measurement.

In chapter 4, all the results and discussion are presented categorically. In section 4.1, comparison of the electrical properties of the MIM and MIIM devices are presented. A detailed discussion on their electrical performance (4.1.1) is provided which is supported by theoretical modeling (4.1.2). Comparison of MIIM devices fabricated via sputtering and ALD is presented in section 4.1.3. The RF responses of the two devices are presented in section 4.1.4. Results of ellipsometery analysis of thin films are discussed in section 4.2. In section 4.2.1, the effect of annealing on the optical properties of thin $NiO_x$ films is discussed. Current-voltage characteristics and device performance of the devices with annealed films is presented in section 4.2.2. Capacitance-voltage measurements are presented in section 4.2.3 to provide in-depth analysis of the annealed thin films. Section 4.3 presents an optimized MIM-based rectifying antenna for frequencies up to 0.4THz.

Chapter 5 summarizes the development of the various devices in this research work. Future directions of the current research work are also suggested in subsection 5.1.

## 2. LITERATURE REVIEW

### 2.1 MIM tunneling diode

#### 2.1.1 MIM device structure overview

The metal-insulator-metal (MIM) junction can primarily be used as a tunnel diode or a capacitor. For an MIM to behave as a capacitor to prevent leakage currents, the breakdown voltage is typically high, and thus it is desired that the insulator between the metals should be close to an ideal insulator [1, 2]. On the other hand, MIM tunnel diodes work on the principle of quantum tunneling, where the insulating layer between the metals is very thin, typically 5nm or less. On application of a bias voltage, current flows between the two metal electrodes due to electron tunneling across the thin insulating barrier. The current-voltage characteristics are non-linear. Due to this behavior, MIM diodes were considered for harmonic mixing and detection of microwaves and infrared radiation [3-5]. The femtoseconds response time of MIM diodes [6] enables it to be used as a mixer and detector at such high frequencies. Point-contact diodes can be regarded as earlier forms of MIM diodes. Prior to the point contact diodes, infrared detectors such as bolometric detectors and thermopile detectors were made from narrow bandgap semiconductors. The output of these detectors is highly sensitive to thermal noise. They required helium cooling to subdue the thermally generated current [7]. The susceptibility to thermal noise leads to low signal to noise ratio resulting in poor sensitivity [8]. However, the antenna-coupled diode rectifiers such as the Schottky diodes [9, 10] and the MIM diodes or previously the point contact diodes [11-13] are fast. They also do not require cooling. This started the concept of uncooled IR detectors. MIM-based sensors have been proposed for replacing the pixel of the focal plane arrays for detection of radiation in the low-IR and THz region [14]. MIM-based sensors have also shown the capability to operate in the millimeter wave region for detection of signals under adverse weather conditions [15]. In the later sections, the operation of an MIM tunnel junction and the governing equations are discussed upon in detail.

### 2.1.2　　　Single-insulator layer

Schematic representation of a typical MIM structure is shown is shown in Figure 2.1, where electrons tunnel from one metal to another when a voltage is applied across the two metal electrodes. The thin insulating barrier can a native oxide, thermally grown oxide, or deposited via chemical or physical vapor deposition techniques. In a conventional semiconductor tunnel diode, tunneling takes place across a heavily doped thin p-n junction when electrons in the n-side align with holes in the p-side. A current flow is generated when electrons tunnel to the p-side on application of a low bias voltage. In case of an MIM tunnel diode, electrons tunnel across the thin insulating barrier at voltages even lower than that of a conventional tunnel diode. The faster transport characteristics in an MIM junction allows it to be used at very high frequencies [16]. The current flow across an MIM tunnel diode is determined by the flux of electrons on the metal-insulator interface where the probability of tunneling depends upon the voltage, temperature, available final states, and shape of the tunnel barrier. Variations in the shape of the tunnel barrier can arise due to contact potentials, surface photo-voltage effects, induced AC voltages due to laser irradiation, etc. Factors such as material, geometrical, thermal asymmetry, and photo-stimulated changes in the electron flux distribution can change the current asymmetry i.e. a high forward current to reverse current ratio [16]. The performance efficiency of an MIM diode is defined by its sensitivity. Sensitivity of the device is defined as the current rectified by the device per unit of incident RF power [16]. It is defined mathematically as the ratio of the non-linearity to the differential conductance of the device and is given by $I''/I'$ where $I'$ is the differential conductance calculated as $dI/dV$ and $I''$ is the non-linearity calculated as $d^2I/dV^2$. For an MIM to be used for rectification of high frequency electromagnetic waves with small amplitudes, it must exhibit higher performance in terms of high sensitivity, nonlinearity, and current asymmetry [17-19]. In MIMs, the operation mostly depends on the difference in work function, $\Delta\psi$, of the metals. However, $\Delta\psi$ alone is not sufficient to overcome the limitations of MIM as a detector or

6

energy harvester. An overview of engineering the insulator layers to overcome this limitation is given in the next section.

Various MIM diodes with similar and dissimilar metal electrodes have been investigated thus far for their tunneling behavior. The current asymmetry of these MIM diodes with respect to voltage is listed in Table 2.1. The various growth and deposition techniques of the insulator is also mentioned. Among the various research groups, only a few have reported the performance of MIM diodes for millimeter wave, THz, and IR detection.
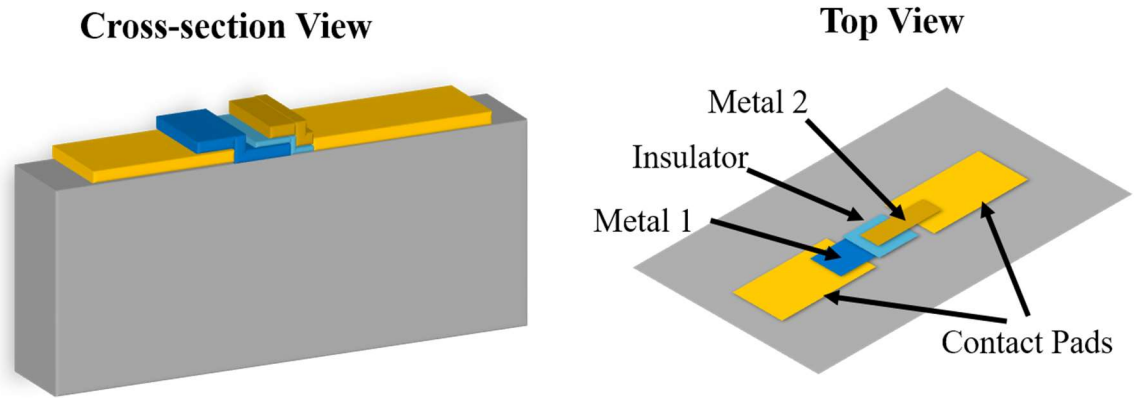


Figure 2.1: Cross-sectional view and top-view of a MIM device

Table 2.1: Current-asymmetry of MIM diodes

| MIM Structure | Asymmetry | Bias | Insulator growth or deposition | Reference |
|---|---|---|---|---|
| Cr-Cr oxide-Au | ~2 | 10V | Native | [13] |
| Ni-Ni oxide-Au | ~2 | 0.15V | Native | [13] |
| Al-Al$_2$O$_3$-Ag | ~1 | 1.5V | Atomic layer deposition (ALD) | [17] |
| Nb-Nb oxide-Ag | ~2 | 0.5V | Native | [17] |
| Cr-Cr$_2$O$_3$-Pd | ~1 | 0.5V | Oxidation | [17] |

| | | | | | |
|---|---|---|---|---|---|
| Cr-$Cr_2O_3$-Mg | ~3 | 0.75V | Oxidation | | [17] |
| Ni-NiO-Au | ~1 | 0.8 V | Oxidation | | [20] |
| Ni-NiO-Ni | 1 | 0.4V | Sputtering-etching and oxidation | | [21] |
| Ni-NiO-Ni | ~1 | 0.25V | Sputtering | | [22] |
| Ni-NiO-Ni | ~1 | 0.4V | Sputtering | | [23] |
| Ni-NiO-Pt | ~3 | 0.3V | Oxidation | | [24] |
| Al-$Al_2O_3$-Al | 1 | 1V | Oxidation | | [24] |
| Ni-NiO-Cr | ~1 | 0.5V | Sputtering | | [25] |
| Ni-NiO-Ni | ~1 | 0.4V | Oxidation | | [26] |
| ZrCuAlNi-$Al_2O_3$-Al | 1500 | 4V | ALD | | [27] |
| ZrCuAlNi-$ZrO_2$-Al | ~10 | 3V | ALD | | [27] |
| ZrCuAlNi-$HfO_2$-Al | ~10 | 4V | ALD | | [27] |
| ZrCuAlNi-$SiO_2$-Al | ~5 | 8V | PEALD | | [27] |
| ZrCuAlNi-$Ta_2O_5$-Al | ~2 | 1.5V | ALD | | [27] |
| ZrCuAlNi-$Nb_2O_5$-Al | ~1 | 1V | ALD | | [27] |
| Pt-$HfO_2$-Ti | ~1 | 0.6V | ALD | | [28] |
| Pt-$TiO_2$-Ti | ~1 | 0.3V | ALD | | [28] |
| Al-$Al_2O_3$-Ni | 1.18 | 1V | Native | | [29] |
| Cr-$Cr_2O_3$-Ni | 1.13 | 1V | Native | | [29] |
| Ti-$TiO_2$-Ni | 2.76 | 1V | Native | | [29] |
| Nb-$Nb_2O_5$-Ni | 3.47 | 1V | Native | | [29] |
| $SrRuO_3$-$SrTiO_3$-Nb | 2.16 | 1V | Pulsed laser deposition (PLD) | | [29] |
| $SrRuO_3$-$LaAlO_3$-Nb | 1.44 | 1V | PLD | | [29] |

### 2.1.3        Double-insulator layer

As mentioned earlier, the MIM tunnel diode is limited by $\Delta\psi$ and the dielectric properties for rectification at high frequencies. Metal–insulator–insulator–metal (MIIM) tunnel diode, an advancement of the traditional MIM technology, is an effort to enhance the MIM diode efficiency. They have recently shown great potential for rectifiers [30-32], millimeter wave wireless communication [33], and terahertz electronics [34] over the traditional MIM diodes. Despite investigations by many research groups, commercialization of MIM-based electronics has been hindered by lack of repeatable, high yield process. In particular, metal-insulator interfacial roughness and oxide stoichiometry has slowed down the technology. Additionally, even with high-quality smooth interfaces, the achievable current asymmetry is limited due to the built in voltage arising from different work functions of the materials at the interface. It has been shown that there is a compromise between the conductivity and current asymmetry in a simple MIM configuration [34]. The addition of another insulator layer, to form metal-insulator-insulator-metal (MIIM) structure, provides improved nonlinearity and asymmetry [16, 35] when each insulator has different band gaps and electron affinities. This improvement is due to the different tunneling effects at different bias polarities across the tunnel diodes. Most of the work in literature has focused on resonant tunneling effect. It is most frequently known as resonant tunneling diode (RTD) and was established by Esaki in 1974 for the heavily doped p-n junction tunnel diode [36]. RTDs proved to be very useful for amplifiers and high-frequency triggers due to its negative differential resistance in its I-V response. In MIIM, resonant tunneling effect can result in greater conductivity while non-linearity is maintained [17]. Step-tunneling is a recent concept which is increasingly being explored [37]. Step-tunneling arises under the opposite bias polarity as compared to that of resonant tunneling and results in a large asymmetry with a sharp turn on. The dominant quantum tunneling defines the nonlinearity under different biases [19].

The theory is elaborated in section 2.2.2. Table 2.2 lists the current-asymmetry of various MIIM diodes in literature along with the deposition technique of the insulator layers.

Table 2.2: Current-asymmetry of MIIM diodes

| MIIM Diode Configuration | Asymmetry | Bias | Deposition | Reference |
|---|---|---|---|---|
| $Cr-Cr_2O_3-Al_2O_3-Ag$ | >280 | 0.4-0.5V | ALD | [17] |
| $Pt-HfO_2-ZrO_2-Pt$ | ~1 | 2-5 MV/cm | Sputter | [38] |
| Pt-NiO-ZnO-Pt | ~1 | 5-6 MV/cm | Sputter | [38] |
| Cr-Al2O3-HfO2-Cr | ~9 | 3V | ALD | [30] |
| $W-Nb_2O_5-Ta_2O_5-W$ | >10 | 0.5V | ALD | [19] |
| ZCAN-Al2O3-HfO2-Al | ~1 | 2.5V | ALD | [37] |
| ZCAN-HfO2-Al2O3-Al | >10 | 0.8V | ALD | [37] |
| Cr-TiO2-Al2O3-Ti | 1, 3 | 1V, 1.6V | ALD | [31, 32] |
| Cr-TiO2-Al2O3-Cr | ~2 | 2V | ALD | [32] |
| Cr-TiO2-Al2O3-Al | ~2 | 1V | ALD | [32] |
| Cr-TiO2-Al2O3-Pt | 1 | 0.5V | ALD | [32] |
| $Pt-HfO_2-TiO_2-Ti$ | 7-12 | 0.8V | ALD | [28] |
| $Pt-Al_2O_3-TiO_2-Ti$ | ~17 | 5V | ALD | [28] |
| $SrRuO_3-LaAlO_3-SrTiO_3-Nb$ | 1.59 | 1V | PLD | [29] |
| $SrRuO_3-SrTiO_3-LaAlO_3-Nb$ | 1.22 | 1V | PLD | [29] |
| Ni-NiO-ZnO-Cr | 16 | 0.5V | Sputter | This work [39] |

## 2.2 MIM device theory

Quantum tunneling occurs due to various physical processes in a MIM junction. The conduction mechanism in MIM can be mainly attributed to: field-assisted tunneling (cold-field electron emission) and thermally-assisted tunneling (Schottky emission) which was extensively explored by Schottky [40], Millikan [41, 42], Fowler and Nordheim [43, 44] in the 1920s. Fowler-Nordheim described that on application of high electric fields electrons, which are initially in thermodynamic equilibrium, escape the emitter side by tunneling across the rounded triangular potential barrier as shown in Figure 2.2 [44]. The potential barrier height reduces and appears "triangular" because of the external electric field. The corner of the potential barrier is rounded off by the charge-image effect.



(a)                                                                (b)
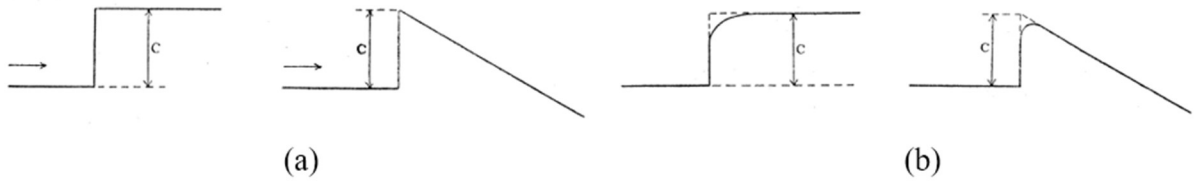
Figure 2.2: (a) Potential barrier appears triangular on high electric field application and (b) corners of the potential barrier are round due to charge-image effect.

In Schottky emission, electrons reach higher energy states due to the increased phonon interaction at higher temperatures. Therefore, in Schottky emission, electrons gain enough kinetic energy and get transported from well above the fermi-level of the emitter to overcome the barrier. This is unlike in Fowler-Nordheim tunneling where electrons tunnel from the electron states close to the emitter's fermi level. At higher temperatures thermally assisted transport is more dominant and field emission is more dominant at lower temperatures. However, at intermediate temperatures electrons first excite to higher energy levels and then tunnel across the potential barrier. Another possible tunneling mechanism that can occur in MIM diodes is photon-assisted tunneling where electrons reach higher energy levels due to photo-excitation.

### 2.2.1 Single-insulator device physics

The Wentzel-Kramers-Brillouin (WKB) approximation method estimates the solution to the Schrödinger equation taking a semiclassical approach. It is often applied to 1-D problems but can be applied to 3-D problems as well. It is a standard approximation used in deriving tunneling current in tunneling diodes. In tunneling diodes, electrons with very low energies cross barrier heights which require much higher energies. These barrier heights depict the walls of the potential well or the potential energy (U) of the barrier (Figure 2.3). The electron is considered to have a wave nature which allows it to traverse across the barrier (region II).
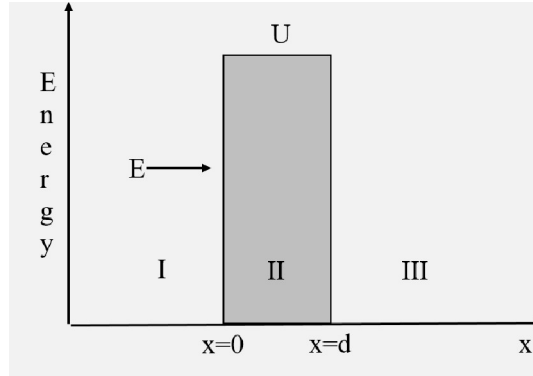


Figure 2.3: An electron with low energy (E) is incident in region I and it can tunnel across a potential barrier, U (region II) to region III.

The wave nature of the electron is given by [45]:

$$\Psi(x) = Ae^{\pm ikx} \tag{2.1}$$

where A is the amplitude of the wave and "$kx$" is the phase. The wavenumber $k$ is inversely proportional to the de Broglie wavelength, $k = \frac{2\pi}{\lambda}$.

The transmission coefficient (T), which is the probability of a particle to tunnel through region (II) and continue to travel to region (III) of Figure 2.3, can be calculated using the normalized Schrödinger's time-independent wave equation [45]:

$$-\left(\frac{\hbar^2}{2m}\right)\frac{d^2\Psi(x)}{dx^2} + U(x)\Psi(x) = E\Psi(x) \tag{2.2}$$

where $\hbar = \frac{h}{2\pi}$, h is the Planck's constant, m is the mass of the electron, E is the total energy of the

particle, and $k$ becomes a constant: $\sqrt{\frac{2m(E-U(x))}{\hbar^2}}$ for (E>U(x)) and $-i\sqrt{\frac{2m(U(x)-E)}{\hbar^2}}$ (for E<U(x)).

Using the Schrödinger's equation in case of a rectangular barrier (i.e. a constant potential

barrier height), $U_o$, and barrier width, d, the transmission coefficient can be calculated as:

$$T = \left(1 + \frac{U_o{}^2}{4E(U_o-E)}\, sinh^2\left(\frac{d}{\hbar}\sqrt{2m(U_o-E)}\right)\right)^{-1} \quad (\text{E<U}_o) \qquad (2.3)$$

WKB approximation states that with a slowly varying potential, U(x), the amplitude and

phase of the exponential wavefunction ($\Psi(x)$) varies as compared to the de Broglie wavelength

($\lambda$). In case of a constant U(x), the phase changes linearly with x. So as per WKB approximation,

with a slowly varying U(x), the phase slowly varies from the linear case of $\pm kx$.

Therefore, the wavefunction does not assume a constant $k$. Only the shape of the

potential is required to estimate the wave function and it is expressed as [46]:

$$\Psi(x) = exp\left(i\left[\pm \int k^2(x) \pm i\frac{\partial k}{\partial x}dx + C1\right]\right) \qquad (2.4)$$

where $C_1$ is a constant. However, WKB approximation neglects the detailed shape of the potential

barrier and the reflected waves with the barrier [17]. With these considerations, the transmission

coefficient with WKB approximations has been simplified to [47]:

$$T \approx exp\left(-\frac{2}{\hbar}d\sqrt{2m(U(x)-E)}\right) \qquad (2.5)$$

where E<U(x) and d is the width of the barrier. The transmission probability is exponentially

sensitive to the width of the barrier and can be measured in terms of particle flow through a

barrier (e.g. electrical current through a thin barrier film). This makes it a great tool for measuring

barrier widths such as in case of tunneling devices for barrier thickness and tunneling microscopy

for tunneling distance.

### 2.2.1.1 Tunneling current between similar electrodes

The WKB model set the ground for other tunneling models for MIM junctions. Simmon's model for electric tunnel effect in MIM junctions is widely accepted today. He derived the current density formulae for MIM junctions based on the WKB approximation. It was Sommerfeld and Bethe who first reported the theory of quantum tunneling in MIM junctions for very low and very high voltages [47]. Their equations were derived for a rectangular barrier which they later improved to a symmetric parabola to account for the image charge potential. The same theory was elaborated upon by Holm to include the intermediate voltages. In 1963, Simmons reported a general theory for the rectangular barrier case which was based on Sommerfeld, Bethe, and Holm's theoretical study [47]. His model, which includes the image-charge potential, predicts a more accurate current-voltage relation for all voltage ranges.

Figure 2.4 shows the energy band diagram of metal-insulator-metal junction without any bias voltage, where both metals are similar.
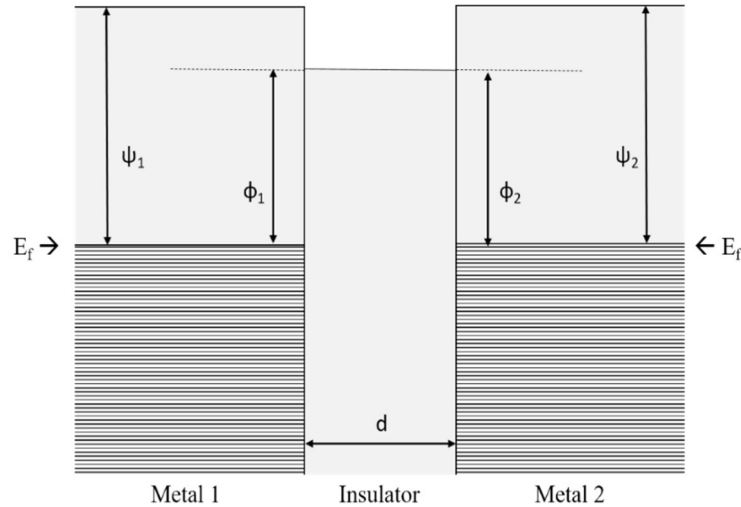


Figure 2.4: Energy band diagram of metal-insulator-metal junctions with similar metals at zero voltage.

Here, $\psi_1$ and $\psi_2$ are the work functions of metal-1 and metal-2. Work function is the minimum energy required to remove an electron from the metal surface to vacuum. The barrier

height at the metal-insulator interface is the minimum energy required to move an electron from the fermi level of the metal to the conduction band of the insulator. The barrier heights of metal-1 and metal-2 are represented by $\phi_1$ and $\phi_2$. The relation between the barrier height and work function is given by:

$$\phi_1 - \phi_2 = \Delta\phi = \psi_1 - \psi_2 = \Delta\psi \qquad (2.6)$$

Therefore, if the barrier height of one metal is known, the other can be calculated. However, the potential energy barrier $\phi_0$, as seen by electrons in both metals is not a constant barrier as depicted by

Figure 2.4 above. As mentioned in section 2.1, due to the charge-image effect the barrier edges are rounded off. It is because the electron attract the positive charges at the barrier interface which induce an image charge. Due to this image within the layer, the barrier becomes narrower and with a reduced height (Figure 2.5).
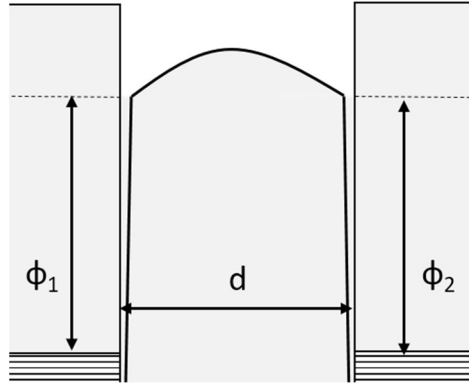


Figure 2.5: Potential barrier becomes narrower and with a reduced height due to image forces.

With these considerations in mind, Simmons modeled the current-voltage relationship for a generalized MIM junction. As per the Simmon's model, the current density equation is [47]:

$$J = J_o\{\phi exp(-A\sqrt{\phi}) - (\phi + e\ )exp[-A\sqrt{\phi + eV}]\} \qquad (2.7)$$

where $J$ is the current density (A/cm²),

$J_o$ is a constant ($J_o = e/[2\pi h(\beta d^{\ 2}])$,

d is the effective barrier thickness (Å) ,

A is a constant $(A = [(4\pi\beta d)/h]\sqrt{2m})$,

$$\beta = 1 - [\frac{1}{8\phi^2 d}] \int_0^d [U(x) - \phi]^2 dx$$

(all the cases have been derived with β=1 for an error of only 1%), and

$\phi$ is the mean barrier height ($\phi = (\phi_1 + \phi_2)/2$ eV).

From the current voltage characteristics of the MIM tunnel junction, the mean barrier height can be calculated. In the above current density equation, the first part of the equation $(J_o\{\phi exp(-A\sqrt{\phi})\}$ represents the current density from electrode 1 to electrode 2. The second part $(J_o\{(\phi + eV)exp[-A\sqrt{\phi + eV}]\})$ represents the current density from electrode 2 to electrode 1. Equation 2.7 can be simplified for the different bias voltage ranges as below [47]:

a) Low-voltage range ($V_{bias} \cong 0$):

$$J = J_L\{\sqrt{\phi}V exp(-A\sqrt{\phi})\}, \text{ where } J_L = \frac{\sqrt{2m}}{d}\left(\frac{e}{h}\right)^2 \qquad (2.8)$$

For very low bias voltage, $\phi \gg V_{bias}$ i.e. $\phi$ is the zero voltage barrier height and hence independent of the bias voltage. Thus, $J$ is linearly proportional to V (i.e. ohmic) for very low voltage range.

b) Medium-voltage range ($0 < V_{bias} \leq \phi_0/e$):

When the V$_{bias}$ is greater than zero but less than the potential barrier.

$$J = J_M(V + \gamma V^3) \qquad (2.9)$$

where $J_M = J_L = \frac{\sqrt{2m}}{d}\left(\frac{e}{h}\right)^2$ and $\gamma = [\frac{(Ae)^2}{96\phi}] - [\frac{Ae^2}{32\phi^{3/2}}]$.

c) High-voltage range ($V_{bias} > \phi_0/e$):

When the V$_{bias}$ is greater than the potential barrier then the tunneling current is explained by the fowler-nordheim equation [48]:

$$J = J_H E^2 exp(-E_0/E) \qquad (2.10)$$

16

where $E$ is the field between the electrodes (V/d), $E_0$ is a constant ($E_0 = \frac{8\pi\sqrt{2m}}{2.96he}\phi_0{}^{3/2}$), and $J_H = \frac{1.1e^3}{4\pi h\phi_0}$.

### 2.2.1.2 Tunneling current between dissimilar electrodes

Simmon's extended his generalized model for a MIM junction with dissimilar electrodes. As per the Sommerfeld's free electron theory, the density of states in momentum space is constant and independent of energy in metal electrodes [49]. This allowed the same model to be used in case of similar or dissimilar metals. The current-voltage characteristics in the case of dissimilar metals are not only dependent upon the bias voltage but also on the polarity of the voltage. As a convention, the MIM junction is considered forward biased if the metal with the lower function is positively biased and the metal with the higher work function is negatively biased. It is reverse biased when the lower work function metal is negatively biased as depicted below in Figure 2.6.



Figure 2.6: Band bending in a MIM junction with dissimilar metal electrode under different bias conditions.

When an insulator forms junctions with two different metals, an intrinsic field exist within the insulator due to contact to the different work function metals. This is said to the set the initial asymmetry in the potential barrier (Figure 2.7). The intrinsic field is [48]:

$$E_i = (\psi 1 - \psi 2)/ed, \text{ where } \psi 1 - \psi 2 \text{ is the barrier height.} \tag{2.11}$$
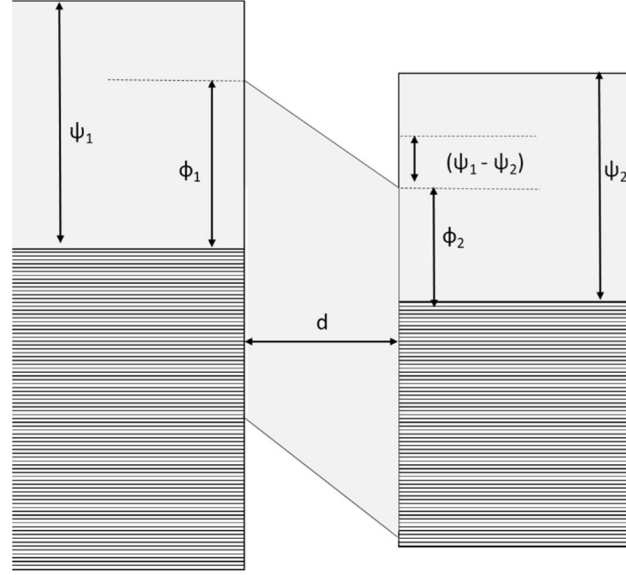
Figure 2.7: Energy-band diagram of a MIM junction with dissimilar metal electrode with zero bias.

In case of dissimilar electrodes, the current density equations for different bias voltage ranges is simplified as below [48]:

a) Low-voltage range ($V_{bias} \cong 0$):

The current density equation remains the same as in case of similar metal electrodes i.e. equation 2.8.

$$J = J_L\{\sqrt{\phi}V exp(-A\sqrt{\phi})\} \qquad \text{(same as equation 2.8)}$$

where $J_L = \frac{\sqrt{2m}}{d}\left(\frac{e}{h}\right)^2$ ($J$ is linearly proportional to V (i.e. ohmic) for very low voltage range i.e. $\phi \gg V_{bias}$, where $\phi$ is the mean barrier height at zero bias voltage.

b) Medium-voltage range ($0 < V_{bias} \leq \phi_{1,2}/e$):

When the $V_{bias}$ is greater than zero but relatively low, the current density can be expressed as:

$$J = J_M(V + \theta V^3) \qquad (2.12)$$

$$\text{where } J_M = \left(\frac{e}{h}\right)^2 \frac{\sqrt{m(\phi_1 + \phi_2)}}{d} exp\left(-A\sqrt{\frac{\phi_1 + \phi_2}{2}}\right) \text{ and}$$

$$\theta = \left[\frac{(Ae)^2}{48(\phi_1 + \phi_2)}\right] - \left[\frac{Ae^2}{32}\left(\frac{2}{\phi_1 + \phi_2}\right)^{3/2}\right]$$

The energy band diagram of MIM junction with dissimilar electrodes under medium voltage range is shown in Figure 2.8.

    c)  High-voltage range ($V_{bias} > \phi_1/e$):

When the $V_{bias}$ is greater than the potential barrier difference (i.e. $V \gg \Delta\phi$ )then the tunneling current is explained by the fowler-nordheim equation [48]:

$$J = J_H E^2 exp(-E_0/E) \tag{2.13}$$

where $E$ is the field between the electrodes (V/d), $E_0$ is a constant ($E_0 = \frac{23\pi\sqrt{m}}{6he}\phi_{1,2}{}^{3/2}$), and

$J_H = \frac{1.1e^3}{4\pi h\phi_{1,2}}$.

    If $\Delta\phi \cong 0$, then the current density equation can be reduced to the high voltage equation (equation 2.10) of the similar electrode model. The energy band diagram of MIM junction with dissimilar electrodes under high voltage range is shown in Figure 2.9.
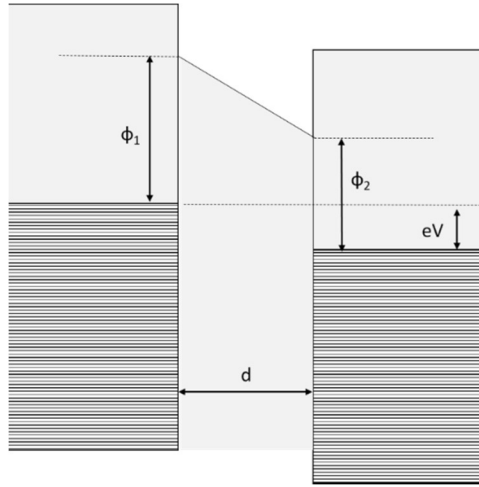


Figure 2.8: Energy-band diagram of a MIM junction with dissimilar metal electrode with medium voltage range.
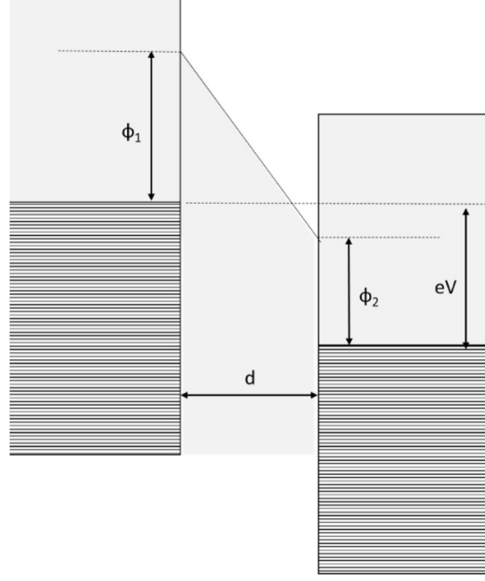
Figure 2.9: Energy-band diagram of a MIM junction with dissimilar metal electrode with high voltage range.

Another model for dissimilar metal electrodes was proposed by Brinkman, Dynes, and Rowel (BDR) in 1969, stating that conductance-voltage is roughly parabolic at low voltages ($\leq 0.4V$) including the image charge forces [50]. They also stated that the conductance minimum is not at zero unless the barrier is symmetrical (i.e. identical metals electrodes). The conductance minimum offset from 0V implies that tunneling occurs even when no bias voltage is applied. As per their theory, the large conductance minimum offset that is observed experimentally is due to organic impurities in the insulator of the junction. However, they failed to explain the large offset but stated that image charge forces cannot dramatically modify the shape of the conductance-voltage curve.

The current density given by the BDR model is [50]:

$$J = \frac{2e}{h}\sum_{k_t}\int_{-\infty}^{\infty} exp\left(-\frac{4\pi}{h}\int_0^d \sqrt{2m[\phi(x,V) - E_x]}\,dx\right) \times [f(E) - f(E - eV)]dE_x \qquad (2.14)$$

where $\phi(x,V) = \phi_1 + \frac{x}{d}(\phi_2 - eV - \phi_1)$, is the barrier height profile without including the image charge forces.

The equation for the barrier height profile (barrier shape) including the image forces proposed by Simmons earlier in the year 1969 [51]:

$$\phi(x,V) = \phi_0 + (E_F - E_t)\left[1 - \frac{\cosh\delta(x-\frac{1}{2}d)}{\cosh\frac{1}{2}\delta d}\right] - \frac{eVx}{d} \tag{2.15}$$

where $\phi_0$ is the interfacial barrier height opposing the transfer of electron from one electrode to the other, $E_F$ is the fermi energy of the metal, $E_t$ is an energy in the insulator less than its conduction band energy, $\delta$ is a constant ($\delta = \frac{e^2 N_t}{\epsilon\epsilon_0}$), $\epsilon_0$ is the permittivity of free space, $\epsilon$ is the insulator dielectric constant, and $N_t$ is the density of traps within the insulator per unit volume per unite energy

was revised in the BDR model to [50]:

$$\phi(x,V) = \phi_1 + \frac{x}{d}(\phi_2 - eV - \phi_1) - \frac{1.15\lambda d^2}{x(d-x)} \tag{2.16}$$

This is the barrier height profile including the image forces, where $\lambda = \frac{e^2 \ln 2}{8\pi\epsilon_0\epsilon d}$.

### 2.2.2 Double-insulator device physics

Addition of another insulator layer in the MIM configuration (i.e. MIIM) provides more current asymmetry in current-voltage (I-V) characteristics of the MIM [16, 35]. This is due to the different tunneling effects at different bias polarities across the tunnel diodes. The importance of asymmetry will be discussed later in section 2.2.3. The two tunneling mechanisms dominant in MIIM are resonant-tunneling and step-tunneling. Resonant tunneling can result in greater conductivity while maintaining the non-linear I-V characteristics [17]. While resonant tunneling is the most reported in literature, step-tunneling is relatively a recent concept. Step-tunneling results in high asymmetry with a sharp turn on and it is dominant under the opposite bias polarity to that of resonant tunneling [37]. The dominant quantum tunneling defines the non-linearity under different biases [19].

Resonant tunneling in semiconductor double barriers was the pioneering work of Chang, Esaki and Tsu in 1974 [52]. It is distinguishable from simple tunneling process due to the presence of quasibound states in the quantum well formation between the two potential barriers. The transmission coefficient is now obtained by solving for the schrodinger's wave equation in the regions shown in Figure 2.10. The transmission probabilities and current densities in case of double barrier junctions were calculated by Schulz in 1988 using the following equation [53]:

$$J = \frac{4\pi e m^* kT}{h^3} \int_0^\infty T(E) \times \ln\left(\frac{1+\exp[\frac{E_F-E}{kT}]}{1+\exp[(E_F-E-eV)/kT]}\right) dE \qquad (2.17)$$

where $m^*$ is the effective mass of particle, k is the Boltzmann constant, and T(E) is the transmission probability.
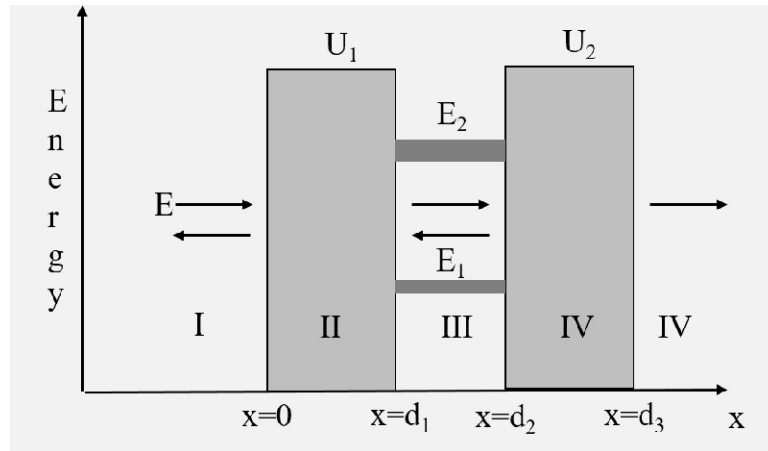


Figure 2.10: An electron with low energy (E) is incident in region I and has to tunnel across two potential barriers, $U_1$ (region II) and $U_2$ (region IV). Electron tunneling probability is unity if the electron energy, E corresponds to the quasi energy states of the quantum well.

The tunneling probability is unity for particles with energies corresponding to the quasi states of the quantum well. As depicted in case of an asymmetric MIIM junction in Figure 2.11 below, Schulz reported resonant tunneling in the forward bias and zero current or resonance under the reverse bias (up to -1V) [53]. In the MIIM structure, energy quantization occurs between the two insulating barrier layers under forward bias (Figure 2.11).
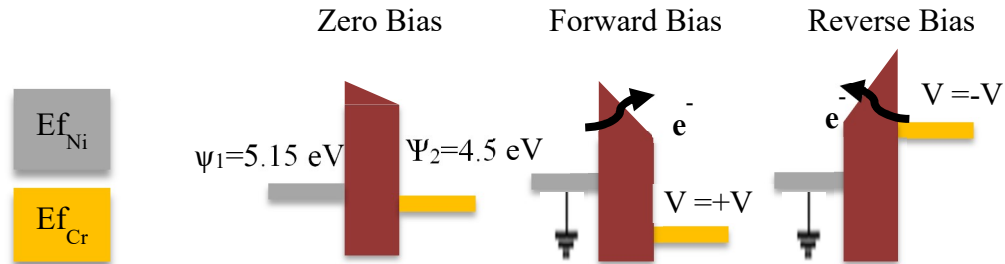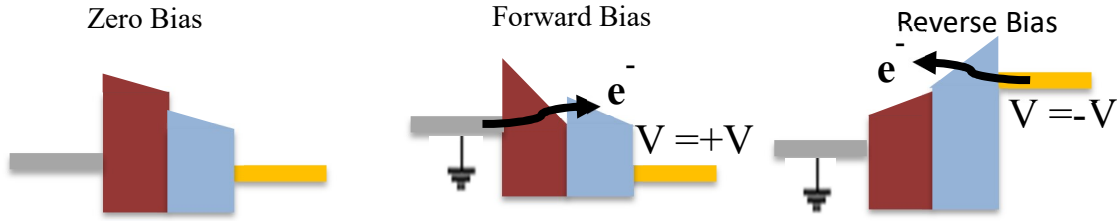
Figure 2.11: Band bending in a MIIM junction with dissimilar metal electrode under different bias conditions.

Later in 1996, Ventra et. al. reported resonant tunneling under forward bias in a multi-barrier quantum structure and simple tunneling in reverser bias at voltages as low as -0.5V [54]. This "simple tunneling" can be considered as "step tunneling" in case of double barrier or multi-barrier. This is because the secondary potential barrier(s) is(are) lowered to an extent (stepped down) under reverse bias that it appears as tunneling is across only a single barrier (Figure 2.11). This way the tunneling distance is reduced, hence step-tunneling. This phenomena was later experimentally explored for double barrier MIIM structures [37].

### 2.2.3 High frequency rectification

MIM and MIIM tunnel diodes have various advantages over current use Metal-Semiconductor tunnel diodes; they are easy to manufacture, inexpensive, use low power, generate low noise, and can operate at high temperatures. These advantages make them perfect components for future uses in terahertz electronics [16, 23], millimeter wave wireless communication [25, 33], low-frequency rectifiers, and rectifying antenna (rectenna) solar cells. The main function of an antenna is to take in time varying electric and magnetic fields and radiate them into space as transverse electro-magnetic waves [55]. A rectenna is a popular method of harvesting energy from the excess of electromagnetic (EM) energy created by contemporary wireless applications. MIM tunnel diode based rectennas have been studied since the 1970s. Four characteristics of features of the MIM diode which are crucial to its optimized operation are asymmetry, non-linearity, resistivity, and sensitivity [16]. The features are interdependent upon

one another and also upon the choice of metal electrodes, insulator, geometry, and process parameters. The sensitivity of the MIM device determines whether the device can be used as a linear rectifier, detectors or energy harvester [56]. In a rectenna, electrons are able to resonate within the full length of the EM spectrum. Therefore, designing an antenna element that resonates at a particular frequency enables the electrons in the fermi level of the metal to oscillate at that frequency without almost any loss, provided the impedances are matched. When the antenna is coupled with a diode, it forms a rectifying circuit to produce usable direct current [16, 17, 57]. The incident ac oscillations on a rectenna is collected and channeled by the antenna to the rectifying element (MIM junction in this case) to generate a signal which is useful for detection. The signal generation is possible due to the tunneling phenomenon in the MIM junction (section 2.2). Conduction takes place due to the femtosecond-fast transport between the two metal electrodes via an ultra-thin (<5nm) insulating layer. For this reason, rectennas have been viewed as promising devices for millimeterwave (30-300GHz) [33, 58], THz (0.3-3 THz) [18], and IR (3-430 THz) detection [59, 60]. The schematic representation of the rectenna is given in Figure 2.12 [18]:
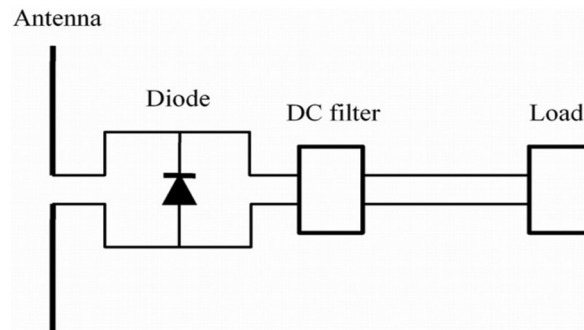


Figure 2.12: Schematic of a rectifying antenna: Rectenna

The equivalent circuit model of the rectenna is given in Figure 2.13 [60]. Here the MIM diode is described by parallel combination of the capacitance ($C_D$) of the MIM junction and resistance ($R_D(V)$) with a non-linear voltage dependency. The parallel combination is in series

with resistance (r) which represent the metal contact between the antenna and diode. The antenna is represented here as an alternating current source ($V_{IR}\cos(\omega t)$) in series with impedance $R_A+jX_A$. Here $R_A$ and $X_A$ are the real and imaginary part of the impedance. The imaginary part is zero at resonant frequencies. The time constant of the circuit is product of diode capacitance ($C_D$) and equivalent resistance (Req) which is $R_D$ in parallel with $R_A+ r$ [60]. For its use as a detector, the impedance of an MIM has to be significantly low so that it can be matched with the antenna. For high frequency performance, cut-off frequency is an important consideration. The cutoff frequency must be higher than the frequency of the incident electromagnetic wave.
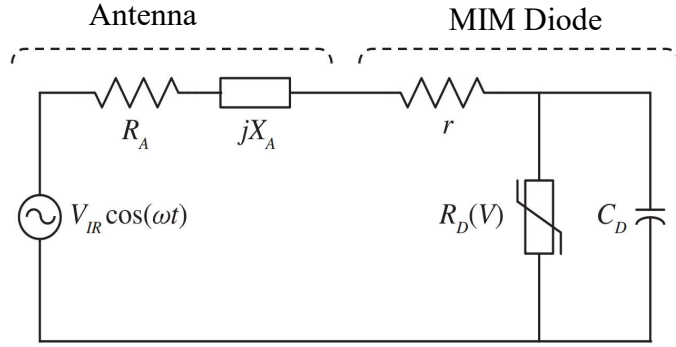


Figure 2.13: Equivalent circuit model of a rectifying-antenna: rectenna.

The cut-off frequency of a MIM diode is given by:

$$f_c = \frac{1}{2\pi R_{eq} C_D} = \frac{R_A+r+R_D(V)}{2\pi(R_A+r)R_D(V)C_D} \tag{2.18}$$

where, $C_D = \frac{\epsilon_o \epsilon_r A}{d}$, where A is the contact area of the diode, d is the oxide thickness between the two electrodes, and $\epsilon_r$ is the permittivity of the oxide material. From these equations it is clear that raising the cutoff frequency can be achieved by lowering the capacitance with all other factors the same. The capacitance can be lowered by decreasing the area, A, or by increasing the oxide thickness, d. However, increasing d has the unwanted effect of reducing the tunneling current. Another option is using oxide materials with higher permittivity.

# 3. EXPERIMENTAL PROCEDURE

## 3.1 Thin-film deposition techniques

Thin layers of metals and dielectrics for MIM diodes are deposited via physical vapor deposition and chemical vapor deposition techniques. In this research work, NiOx thin films were deposited using reactive DC sputtering and thin ZnO films were deposited using thermal atomic layer deposition. Sputtering is a high-energy process where the target material is physically removed via energized argon ions. Atomic layer deposition (ALD) is a chemical process where reactive gases are introduced on the surface sequentially for deposition of target material. The choice of deposition technique was due to the availability of materials.

### 3.1.1 Sputtering

#### 3.1.1.1 DC sputtering

Sputtering is a form of physical vapor deposition where a target material which is to be deposited is bombarded by fast moving ions to eject target atoms onto the substrate. The ions hit the surface of the target and eject the top most atoms of the target. The atom's binding energy determines the motion of its diffusion onto the substrate. The atoms combine with other atoms on the substrate to form nucleation sites [15]. Agglomeration of such nucleation sites turns into an island growth. After a certain period the islands expand to touch each other. This agglomeration continues until a continuous film is formed [61]. The sputtering chamber used for this project is shown in Figure 3.1(a). During sputter deposition, target of the material of interest is placed in a vacuum chamber. Next, a plasma is generated by using Argon, an inert gas, to physically etch the material target. Etching is possible due to the ion bombardment of Argon ions on the target (cathode). The sputtered atoms of the target material deposit on the substrate and walls of the chamber (anode), as depicted in Figure 3.1(b). Sputtering can either be DC (diode) or AC (radiofrequency) where the chamber walls act as the counter electrode. The deposition rate depends on the plasma concentration which is dependent upon pressure inside the chamber and

power. The spacing between the target and substrate effects the deposition rate as well as the uniformity in the film. In this work, a sputtering system was setup with an RF gun, a DC gun, and a DC gun for magnetic materials. For this research work, nickel and nickel oxide were sputtered using the DC gun for magnetic materials. ZnO was deposited using the RF gun. The substrate-target distance was 30cm.
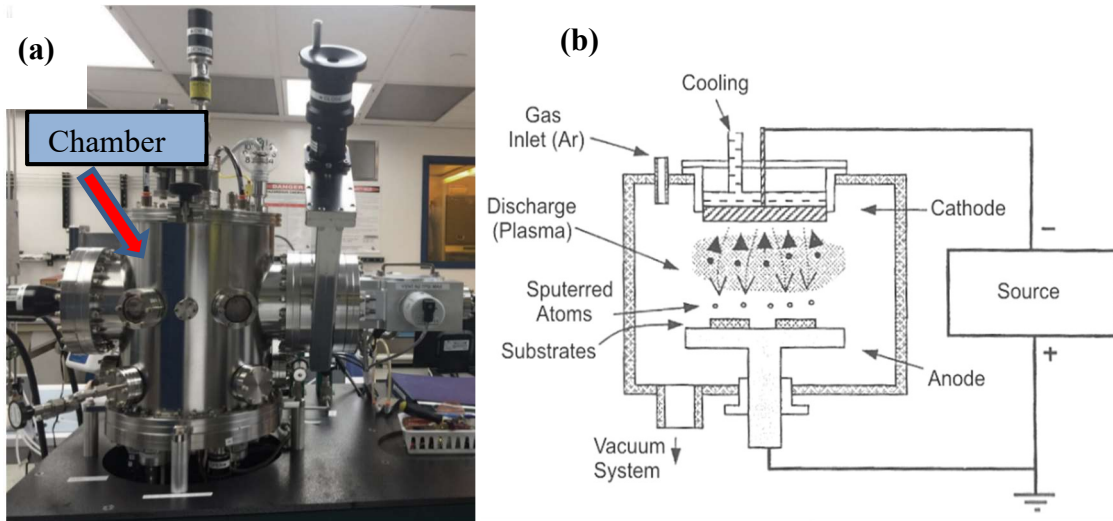


Figure 3.1: (a) Sputtering chamber used in this work; (b) illustration of DC sputtering [61]

### 3.1.1.2 RF sputtering

RF sputtering is primarily used for sputtering insulating materials. In RF sputtering, the potential on the target is periodically reversed at frequencies above 50 KHz such that the Ar ions do not have enough mobility to form DC-diode like discharge [61].  This way the applied potential is felt across the space between the cathode and anode instead of just the cathode. An alternating positive-negative cycle of potential is applied to the cathode. During one half-cycle, ions are accelerated towards the surface with enough energy to etch away the target material and in the other half-cycle electrons reach the surface to nullify the charge build-up [62]. The deposition rate during RF sputtering is characteristically low.

### 3.1.1.3 Reactive sputtering

Combination of an inert gas (Argon) and a reactive gas (such as oxygen) to create plasma during DC sputtering results in reactive sputtering. Here the reactive gas, not only participates in etching the target material but also chemically reacts with the deposited atoms to form compounds [62]. This is also called plasma oxidation. This is an alternate way of depositing insulators besides RF sputtering. However, the role of each process depends greatly on the pressure and the chemical activity of the reacting species. It is also to note, that the reactive gas also etches the deposited films on the substrate. As shown in

Figure 3.2 below, the target material (for e.g. zinc) is made the cathode while the chamber is anode. Once the chamber is under high vacuum (<10 X $10^{-6}$ Torrs), high purity argon is pumped into the chamber to maintain a process pressure of <10mTorrs. A large DC bias is maintained between the cathode and anode which ignites the plasma. The plasma is composed of the argon ions and other radicals. These large argon ions are accelerated towards the negatively biased targets resulting in removal of Zn atoms. Zinc oxide can result from reactive DC sputtering, where the Zn target will be bombarded by Ar+ ions in the presence of reactive $O_2$ gas which will chemically react with the sputtering Zn atoms resulting in ZnO compound.
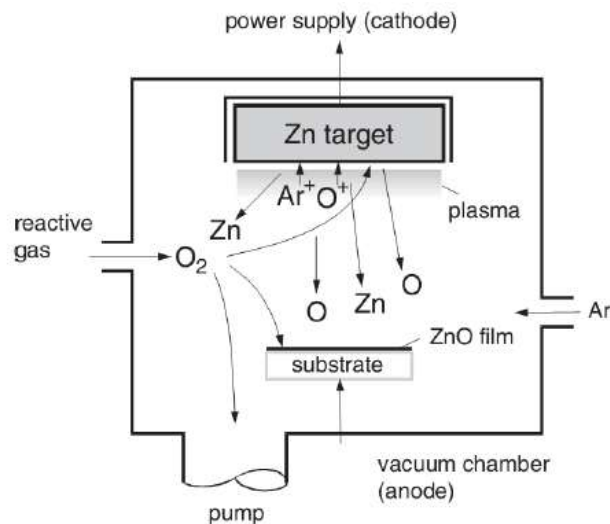


Figure 3.2: Illustration of reactive sputtering [63]

### 3.1.2    Atomic layer deposition

Atomic layer deposition (ALD) technique offers unparalleled advantages of defect-free deposition, conformal coverage, ultra-thin film (<5nm) deposition with precision in control, and low deposition temperatures. ALD process involves alternating the exposure of a substrate to the precursor vapors which chemically react at the surface of the substrate (Figure 3.3). Due to the self-limiting nature of the precursor reactions on the substrate, the heterojunction films will be extremely uniform, conformal, and continuous (Figure 3.3). This simple yet unique deposition technique has improved production of many micro- and nano- electronic devices. We've setup a home-built ALD deposition tool for deposition of the oxide films (Figure 3.4).
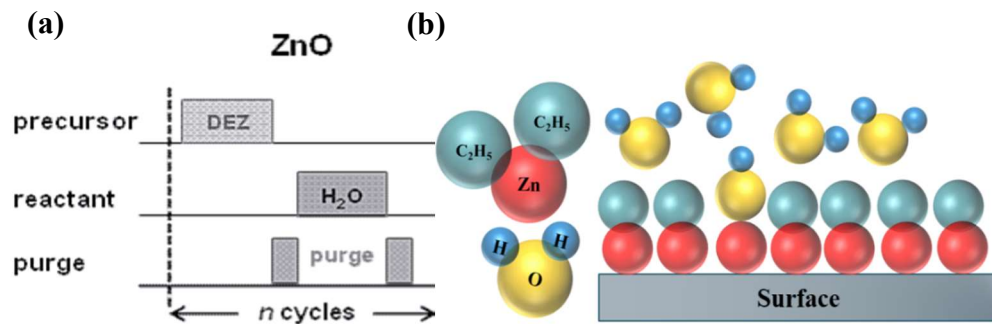


Figure 3.3: (a) A single ALD cycle and (b) Illustration of self-limiting ALD reaction
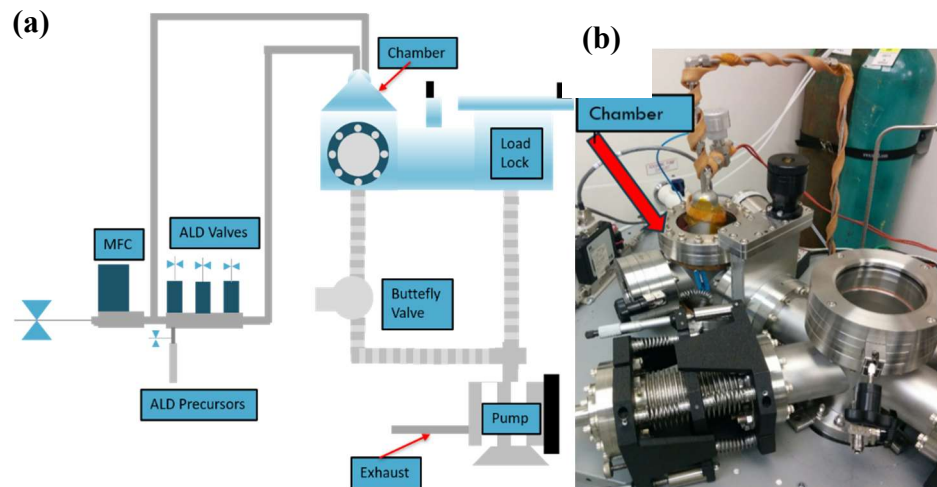


Figure 3.4: (a) Illustration of the home-built thermal ALD setup and (b) ALD system used for deposition

### 3.1.2.1 Precursor chemistry

The crystallization behavior of ALD grown thin films strongly depends on precursor chemistry. ALD precursors need to satisfy several requirements, most importantly: sufficient volatility, thermal stability, and high reactivity. A high volatility is a must since ALD is a gas-phase method and high volatility is required to deliver high precursor flux. Gaseous and liquid precursors are preferred over the low volatile solid precursors. In contrast to the CVD-type growth, if the precursor thermal decomposes at a given deposition temperature, then the self-limiting growth of ALD films will not take place (Figure 3.5). Therefore, the thermal stability of a precursor helps determine the higher end of the ALD temperature process window. ALD is a surface reaction-limited process rather than diffusion-limited and thus maintains film uniformity and conformity. The lower end of the ALD process temperature range is also an important in case of certain applications such as coating on polymers and biomaterials. Therefore, rapid reactions are desired which will ensure fast completion of the surface reaction. The growth reaction should not produce reactive byproducts since reactive by-products can etch the film material and hence provoke non-uniformity and low growth per cycle (GPC) [64, 65].
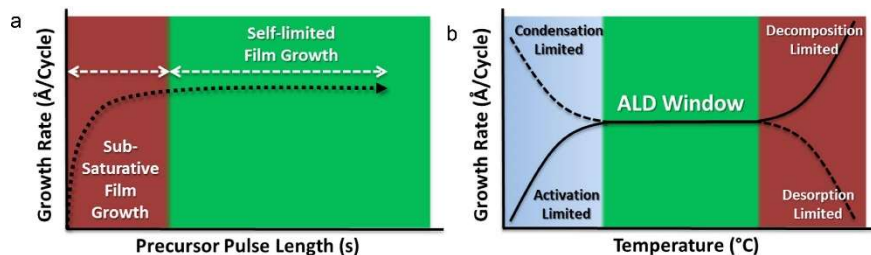


Figure 3.5: ALD growth window [64]

### 3.1.2.2 Oxygen sources and plasma-enhanced ALD

Reactive oxygen sources play an important role in the formation of oxides, gate oxides, and high-k dielectric films by ALD technique. Oxygen sources, such as $H_2O$, $O_3$, $O_2$, $H_2O_2$ as well as oxygen plasma, have been used in the ALD of transition metal oxide thin films. Once again, like the choice of precursors, the choice of the oxygen source depends on the targeted

application. For example, in case of high-k materials deposition, the oxidative power of the oxygen source towards the bare Si surface should be low to minimize the additional growth of low-k SiOx interfacial layer [66].

Water and ozone are the most common oxygen precursors. Ozone is a strong oxidizer and causes the formation of $\geq$1nm thick interfacial layer on H-terminated silicon substrate. Therefore, ozone is not the most suitable oxygen source for high-k oxides for CMOS transistor applications. On the other hand ozone efficiently burns out the ligands during ALD the process leaving lower amounts of impurities. Thus producing cleaner and denser films with improved electrical properties compared to those deposited with water as the oxygen source. Another good reason to prefer ozone over water is the long purging time required in case of water due to the strong interaction between the polar water molecule and oxide surfaces. Water-based processes are depended upon the presence of hydroxyl groups on the surface and on the high reactivity of water towards the chemisorbed metal precursor. When water is used as the oxidizer, the ligand-exchange reaction breaks the metal-ligand bonds of the precursor and also an O-H bond, which forms both a M-O bond and a L-H bond [67].

PEALD is an energy-enhanced method that has recently received increasing attention. Usually $O_2$ is found inert in thermal ALD and is used as a radical source in PEALD. In PEALD, during the reactant step, the surface is exposed to the species generated by oxygen plasma discharge. PEALD allows lower deposition temperature as compared to thermal ALD. Further, PEALD has been employed successfully for the deposition of several metal thin films that cannot be deposited by thermal ALD. PEALD, however, also faces certain challenges such as the development of suitable equipment for the industrial scale-up of the processes, batch reactor in particular, plasma-induced damage to the surface, and often lower conformity on non-planar substrates [64, 67].

### 3.1.2.3 Influence of temperature

Temperature affects the phase transition in films from amorphous to crystalline, in the development of ALD film deposition processes. This leads to changes in film crystallinity and other changes in their film composition. With increasing process temperature, mass transport kinetics in the film increases with changes with the reaction. Choice of process temperature also governs the choice of available ALD reactants leading to their decomposition. This also largely determines the impurity content in the film. It has been seen that with increase in process temperature though, the impurity contents change in the film, which leads to a decrease in the temperature [68].

### 3.1.2.4 Influence of substrate

The outermost surface of the substrate has a strong influence on ALD growth, since it determines how the growth starts. Suitable adsorption sites are needed for growth to occur else no growth occurs. The film thickness also plays a role in determining the crystalline or amorphous nature of the film. For significantly thicker films, an amorphous film may turn to crystalline. The substrate also plays an important role in determining the grain size and growth orientation [68].

### 3.1.2.5 Nucleation of transition metal oxide films

Nucleation of ALD is critical for continuous and pinhole-free ultrathin films. If the reaction of ALD precursors with the initial substrate is not effective, the ALD film may either nucleate only at particular defect sites on the initial substrate or may not nucleate at all [69]. This would lead to island growth as in Volmer-Weber growth mechanism [70]. With many cycles, these islands may grow together to form a film that is continuous. For ultrathin films though, the ALD films are coarse and do not conform to the initial substrate. For a uniform layer-by-layer ALD film growth as described by the Frank van der Merwe mechanism [70], it is necessary for the ALD precursor to react with the initial surface species in the first cycle of deposition. This kind of efficient nucleation is seen for metal oxide ALD on oxide substrates and usually for metal

nitride ALD on oxide substrates [69]. Metal ALD on oxide surfaces also can face some nucleation challenges since metals do not generally wet oxide surfaces. Studies in heterogeneous catalysis indicate that metals prefer to form clusters on oxide surfaces [69, 71].

### 3.1.3 Electron-beam evaporation

Electron-beam evaporation is another common physical vapor deposition technique for deposition of thin film metals and oxides. An electron beam is focused on solid pellets of the material in a tungsten or graphite crucible to evaporate the material onto the substrate. Since evaporation is a line of sight process, the substrates need to be rotated for a uniform surface coverage [15]. In this project e-beam evaporation has been used for depositing of chrome and gold metals as the contact pads and the top electrode. The schematic of the e-beam evaporation is depicted in Figure 3.6(a) [72] and a picture of the actual e-beam system used for this work is shown in Figure 3.6(b).



(a)                                                      (b)
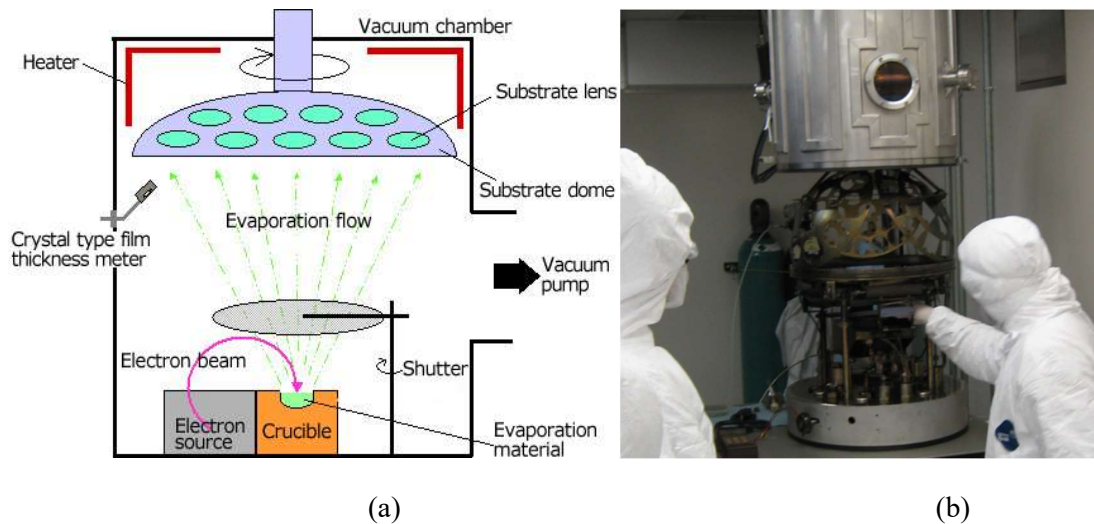
Figure 3.6: (a) Schematic of the e-beam evaporation [72]; (b) E-beam system used for this work.

## 3.2 Thin film characterization

### 3.2.1 Ellipsometry

Ellipsometry is an optical measurement technique which determines a film's thickness and optical constants (refractive index, n and coefficient of extinction, k). In this technique a light is incident on the sample at an angle. Here the light, simultaneously reflects and transmits through the thin film and then again transmits and reflects at the next interface (if possible). The light that reflects through the upper and lower boundaries of the film with interfere with one another and form a new wave that is sent back to the detector (Figure 3.7(a)). The detector measures the change in polarization state of light reflected from the surface. The values are measured in terms of Ψ and Δ. These measurements may be connected to the materials properties and thicknesses of the reflecting surface structure through Maxwell's equations, derived into a convenient algebraic form, called here, the reflecting surface model. The well-known equations are used as follows:

$$R_p = \frac{r_{1p} + r_{2p}e^{i\delta}}{1 + r_{1p}r_{2p}e^{i\delta}} \qquad (4.1)$$

$$R_s = \frac{r_{1s} + r_{2s}e^{i\delta}}{1 + r_{1s}r_{2s}e^{i\delta}} \qquad (4.2)$$

where $R_p$ and $R_s$ are the complex overall reflection coefficients for the parallel and perpendicular polarized light respectively (Figure 3.7(b)). Note that the term to the left is capital "R" in Ellipsometry and Polarized Light by Azzam and Bashara but appears as lower case "r" in the Handbook of Ellipsometry edited by Tompkins and Irene [73, 74]. Values of $r_{1p}$ and $r_{1s}$ are the reflection coefficients for light incident on the ambient-film interface (4.1) and $r_{2p}$ and $r_{2s}$ are those for light incident on the film-substrate interface (4.2). All four of these values may be computed using the well-known Fresnel reflection equations for a single layer on a bulk substrate [73]. The value of δ results from the transmission of the light through the film and the path length difference for each of the multiple reflections to the detector:

34

$$\delta = \frac{-4\pi d n_2 \cos(\theta_2)}{\lambda} \qquad (4.3)$$

where d is the film thickness, $n_1$ is the film complex index ($n_1 = n - ik$), $\alpha_1$ is the angle of refraction in the film, and $\lambda$ is the light wavelength in air. The value of $\alpha_1$ is obtained from the Snell's law.

The measurement ($\Psi$ and $\Delta$) is a ratio of the two fresnel's reflection coefficients ($R_p$ and $R_s$),

$$\text{Tan}(\Psi)\, e^{i\Delta} = R_p/R_s \qquad (4.4)$$

Measurements can be highly accurate and reproducible. They are obtained using light which impinges on the reflecting surface at an angle of incidence greater than 0° and less than 90°, typically in the range from 50° to 70°, with respect to the surface normal direction. There are at least two methods for extracting reflecting surface properties from the measurements. In both cases the process begins with the specification of an estimated reflecting surface model based on what is known, for example composition of the substrate, film composition, and film thickness.
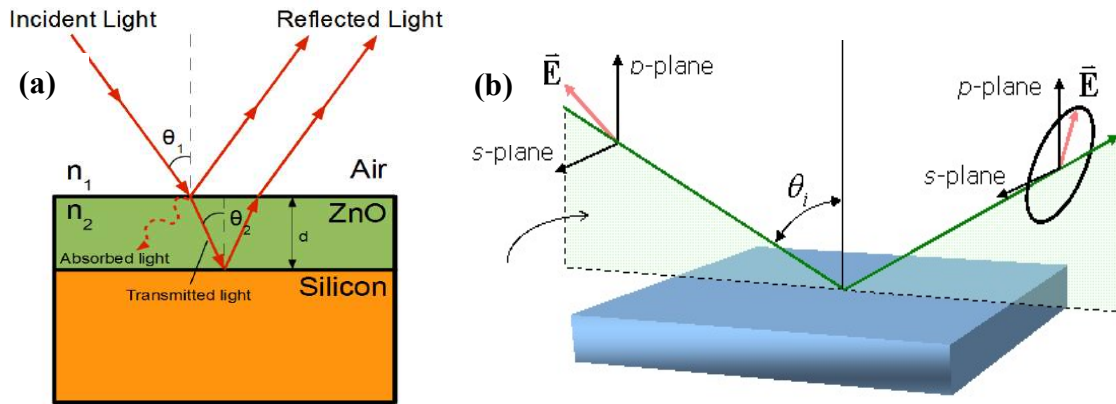


Figure 3.7: (a) Light reflecting through the upper and lower boundaries of the film will interfere with one another [63]; (b) The p-polarized light and s-polarized light reflects differently to the incident one [75].

The data-fitting method uses all of the measurements across angle and wavelength simultaneously. The estimated model, including estimated structure and properties, is used to compute theoretical measurements at all wavelengths and incidence angles employed in the

measurements. The theoretical measurements are then compared statistically to the actual measurements in a least squares sense in terms of an objective function of Mean Squared Error (MSE) or $\chi^2$. Subsequently a numerical method, commonly Levenberg-Marquardt, makes adjustments to the estimated model to bring the measured and computed data into agreement in an iterative process by reducing the objective function to a minimum [74]. Very commonly the objective function is initially not reduced sufficiently which makes it necessary to adjust specification of the estimated reflecting surface model by hand. In this way a variety of model specifications can be used with the measured data in pursuit of a sufficiently low objective function.

By contrast the method presented here solves the mathematical problem at each wavelength independently rather than statistically fitting across all measured wavelengths simultaneously. It does so by taking advantage of a number of theorems of Complex Analysis to algebraically transform the mathematical model into a more convenient form using no assumptions. Additional measurements at different film thicknesses, and/or if possible, at different incidence angles are required to mathematically solve for reflecting surface parameters at each wavelength independently. Further details of this methodology for ellipsometry problems can be found in publications by Urban and Barton [76-81]. When used with spectroscopic data the independent solution at each measured wavelength may be graphed against wavelength to provide visualization of the optical properties as a function of wavelength.

An advantage of solution curves, which come straight out of Maxwell's equations, is that they have been shown to provide useful information at each measurement wavelength including the condition of the equations and proximity of solutions to singularities [82]. These factors are dependent only on the underlying physical model and not at all on the solution method. A very small variation across the thickness of a film of interest poses no particular solution problem using the simple, single-layer reflecting surface model and the variation results in the solution

being a kind of average. On the other hand, a significant variation in properties in the growth direction cannot be made to agree well with the simple, single-layer model. In a previous work Urban and Barton presented a method for solving in the case in which the initial growth is inhomogeneous followed by subsequent homogeneous growth. This method works by use of a "numerical substrate" and does not require any knowledge of the physical substrate [83].

In this work, ellipsometry measurements were performed using a Woollam M2000 micro focusing ellipsometer. Data was taken at 64.63° incidence angle and across the wavelength range from 370 nm to 950 nm light wavelength. The instrument was calibrated periodically using a National Institute of Standards and Technology standard and was calibrated daily using the calibration standard provided by the instrument manufacturer. Multiple measurements were made in the area of interest to confirm that the data was not substrate location sensitive. Data was averaged for 50 to 100 revolutions.

### 3.2.2 AFM

AFM is a technique for measuring the topography and surface roughness. A cantilever (typically made up of silicon) with a tip protruding from the bottom at the edge is used to scan a surface. As the tip touches the surface and raster scans, the surface features cause the cantilever beam to deflect. The deflection and oscillation amplitude of the beam is registered (in a position sensitive detector) as a change in position of the laser beam reflecting off the cantilever's surface (Figure 3.8). When the changes in the deflection or oscillation are different than the specified setpoint voltage, a piezoelectric stack actuates and corrects the cantilever back to the setpoint. These voltages which are sent to the correction piezo are recorded and use to determine the height at a specific X-Y position. This data is stored as the tip raster scans the area of interest. A Nanonics Imaging ltd. AFM in tapping mode was used to determine the roughness of the as-deposited films, respectively.
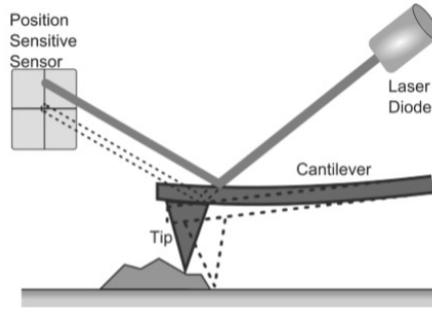
Figure 3.8: Illustration of an scanning AFM tip [84].

## 3.3 Diode design and fabrication

### 3.3.1 Design

Different design approaches were considered for creating the tunnel junction of the thin film diodes. Standard photolithography and liftoff process were used for patterning. Contact pads and top metal electrode, Chromium (Cr), were deposited by e-beam evaporation. Bottom metal electrode (Ni), nickel oxide ($NiO_x$), and zinc oxide (ZnO) were deposited by magnetron DC, reactive DC, and RF sputtering, respectively. MIIM devices with ALD deposited zinc oxide were also fabricated. Due to the simpler and faster process steps required for fabricating multilayer stack, a MIM stack can be used for determining the electrical characteristics of the diode. However, in such a configuration the top contact area length cannot be minimized below 1 mm to avoid misalignment of the probe on the contact pad. Within such a large area there is variation in thickness of the insulator which is responsible for the variation in electrical characteristics.
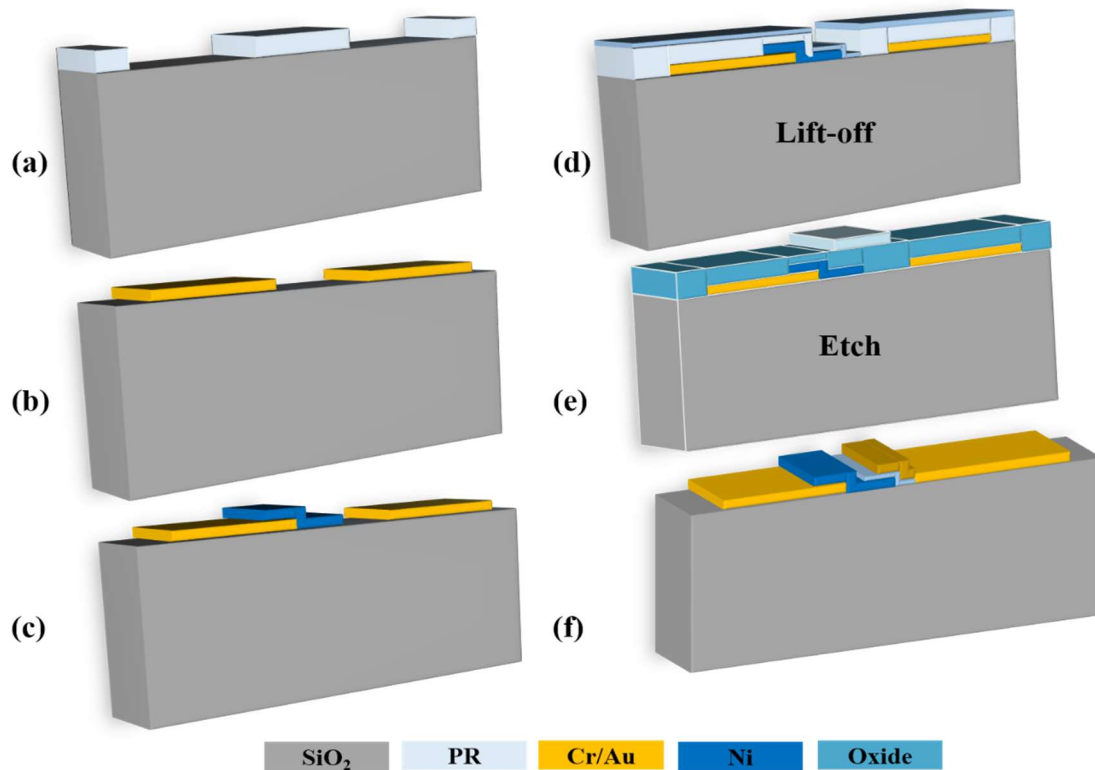
Figure 3.9: Fabrication steps for a MIM diode: (a) Photoresist (PR) patterning on SiO$_2$ Substrate (b) Deposition and lift-off for Cr/Au contact pads (c) Bottom Ni electrode PR patterning, deposition, and lift-off (d) PR patterning for sputter deposition of oxide layer followed by lift-off (e) PR patterning after ALD deposition of oxide layer followed by an etch step (f) PR Patterning, deposition of Cr/Au top electrode, and liftoff for final MIM or MIIM stack

To overcome the contact area limitation, design in Figure 3.9 was used where the contact area can be reduced. Steps (a), (b), (c), and (f) are followed for all the devices. Step (d) involves PR patterning, deposition of sputtered oxide followed by liftoff. Step (e) is done in case of ALD, where, oxide is deposited first followed by PR patterning and etch. The final stepped design of an MIM diode is shown in Figure 3.9(f). The added advantage is that the contact pad width can be more than 1mm while the diode junction can be reduced in area. This allows the probes to land elsewhere instead of exactly on top of the MIM junction where there are risks of puncturing the top metal contact with the probe. However, in this arrangement a junction is formed on the side-wall as well. One expects the side-wall to be a straight edge but the shape of side-wall can either be slanted, jagged, curved, or finned edge (Figure 3.10) [56]. For example, wet etching can lead

to a slanted edge or dry etching techniques such as reactive ion etching (RIE) or deep-RIE (DRIE) can lead to jagged edge due to scalloping. Physical vapor techniques such as sputtering or evaporation can lead to curved edges. Finned edges often result from lift-off process. As a result, in a stepped design it is hard to control the geometry of the side-wall junction which leads to invariability or non-repeatable device performance. Therefore, electrical measurements were taken for MIM devices with an extra $SiO_2$ spacer layer also. This spacer layer can be patterned and deposited before the second metal layer such that contact is formed only on the top of the insulator and not on the side-wall (Figure 3.11). It was found that the repeatability greatly improved for devices with an extra spacer layer. The thick spacer layer imposes challenges of parasitic capacitance in electrical measurements and it is an obstruction in case of optical measurements. Therefore, the spaced-design was not explored in case of optical measurements.
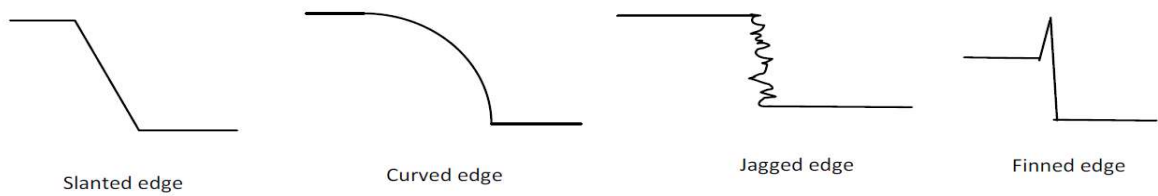


Figure 3.10: Possible sidewall profiles of a thin film due to different processing techniques [56]
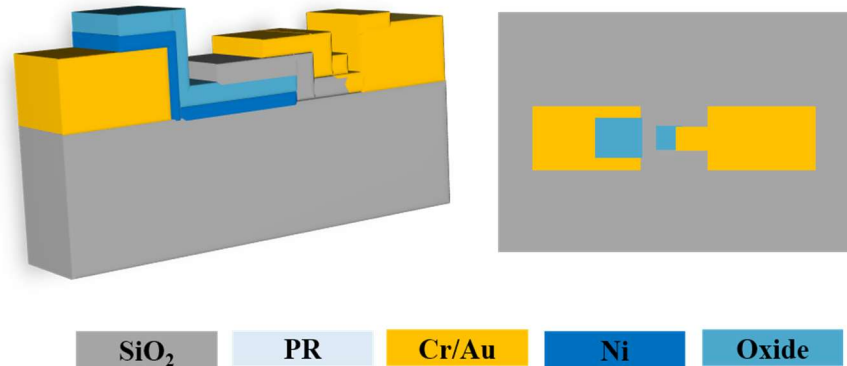


Figure 3.11: Design of an MIM diode with an extra spacer layer

### 3.3.2    Fabrication

#### 3.3.2.1  Substrate preparation

Thin film metal-insulator-metal (MIM) diodes are fabricated on high-quality borosilicate (BOROFLOAT 33) glass wafer. The wafer was cleaned by standard RCA clean process to remove organic contaminants [85]. By standard photolithography and liftoff process, metal and oxide layers were patterned. AZ-5214E image reversal photoresist was used as the negative photoresist for patterning and OAI mask aligner was the exposure tool. First, chromium (Cr) and gold (Au) were deposited using e-beam evaporation for contact pads. After liftoff, deposited film thickness was measured using Dektak Profilometer. A second step of photolithography was done using the same photoresist for patterning bottom electrode. Nickel (Ni) was deposited by DC magnetron sputtering as the bottom electrode. In the third step, nickel oxide (NiOx) was deposited and patterned as the insulator layer. The oxide was deposited via reactive DC sputtering. As the final layer, Cr and Au were deposited again on top of the oxide to form the Ni-NiOx-Cr junction.

For ellipsometry characterization, thin films were deposited on a bulk (1 0 0) p-type silicon wafer. The wafer was first cleaned by RCA standard cleaning process to remove native oxides and organic contaminants [85]. For removal of native oxide, the substrate was etched in 1:6 ratio buffered oxide etchant (BOE). Subsequently it was rinsed in DI water and dried with nitrogen.

#### 3.3.2.2  Thin film deposition

Ni and NiOx were deposited via sputtering and the base pressure was kept below 2μTorr to avoid contamination of the thin films. 100 nm of Ni was sputtered at 100W power and working pressure of 10 mTorr for nearly 10 minutes. The NiOx film was reactively sputter deposited in the presence of argon and oxygen with flow ratio of 2:1 (10 sccm, 5 sccm) or 33% oxygen. This ratio was selected following experiments at different ratios and flow rates with the objective of providing the lowest surface roughness. For ellipsometry analysis, NiOx films were deposited

onto single crystal (100) p-type silicon wafers with a resistivity of 100 Ω-cm. Prior to deposition, the Si wafer was etched in 1:6 ratio buffered oxide etchant (BOE) for removal of native oxide. Subsequently it was rinsed in DI water and dried with nitrogen. NiOx films were sputtered at 30W power and working pressure of 10 mTorr, resulting in a deposition rate of 1nm/min. In case of annealed oxide films, the sputter deposited NiOx films were annealed at 400 °C in Thermco's mini-brute tube-furnace.  A constant 20sccm flow rate of oxygen was maintained in the furnace to drive the oxygen further into the NiOx film.

The dielectric nickel oxide thin films were reactively sputter deposited. A DC magnetron source was used for sputtering of nickel target (2 inch diameter) in the presence of argon and oxygen for deposition of NiOx films. Various argon to oxygen ratios were experimented with and plasma with flow ratio of 2:1 (10 sccm, 5 sccm) or 33% oxygen concentration provided the lowest surface roughness. While sputtering, the substrate holder was maintained at room temperature and the substrate was kept at a distance of 30cm from the target. The substrate was not rotated and was placed directly above the 2 inch target. NiOx samples were sputtered at a rate of 1nm/min with 30 W power and a working pressure of 10 mTorr. NiOx was sputtered for 3 minutes targeting a thickness of 3nm.

Zinc oxide (ZnO) was sputtered as the second insulator layer for MIIM formation. A ZnO target was used to deposit films by RF sputtering and $O_2$ gas was introduced to eliminate oxygen vacancies. It was sputtered at a rate of 2.5nm/min when deposited at 100 W power and a working pressure of 30 mTorr. It was sputtered for 72 seconds also targeting a thickness of 3nm. The same oxygen to argon ratio was used to keep the process consistent.

ZnO films were also deposited via thermal ALD process for comparison.  A (1 0 0) p-type silicon substrate with a resistivity of 100 Ω-cm was used. The substrate was etched in 1:6 ratio buffered oxide etchant (BOE) to remove the native oxide. Subsequently it was rinsed in DI water and dried with $N_2$. It was then transferred to the home-built ALD setup.  The schematic of

the ALD setup is shown in Figure 3.4. The chamber consists of a load-lock area where the samples are loaded. Once the load-lock is under vacuum (<10 mTorr), the samples are transferred to the chamber. The chamber has a showerhead on top from where the reactance precursors enter. The outlet is at the bottom of the chamber which is connected to a Pascal Technologies dry scroll pump. The substrate holder is inside the chamber which is maintained at a distance of 4 inches from the showerhead.

ZnO films were deposited using diethylzinc (DEZ) as the metal precursor and water vapor ($H_2O$) as the oxidizer. Prior to deposition, the substrate was heated at 150 °C at least for one hour. This was done to stabilize the substrate temperature. Argon was used as the precursor carrier gas and a flow rate of 10 sccm was maintained. A process pressure of 500 mTorr was maintained inside the ALD chamber. Both DEZ and $H_2O$ were pulsed for 250ms in sequence followed by long purges. The purge times for DEZ and $H_2O$ were 2 minutes and 3 minutes. Very long purge times were required due to the large volume of the chamber and complicated inner design of the chamber. By varying the number of cycles, samples of different thicknesses were prepared. The chemical reaction in the ALD process with DEZ and de-ionized water precursors can be express as follows:

$$CH5 - Zn - C2H5 + H2O \rightarrow ZnO + 2\ C2H6 \tag{4.5}$$

This reaction occurs in two stage, when the half-part chemical reactions take place at the surface during DEZ (phase 1) and water (phase 2) pulses:

$$\text{DEZ phase: surface} - OH + C2H5 - Zn - C2H5 \rightarrow \text{surface} - O - Zn - C2H5 + C2H6 \tag{4.6}$$

$$\text{Water phase: surface} - O - Zn - C2H5 + H2O \rightarrow \text{surface} - O - Zn - OH + C2H6 \tag{4.7}$$
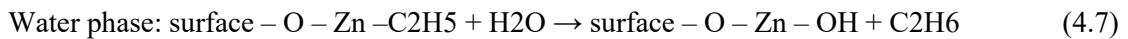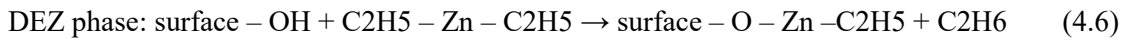
### 3.4 Device characterization

#### 3.4.1 DC characterization

Keithley 4200 SCS Parameter Analyzer was used for the DC I-V measurements of the MIM diodes connected in series with noise shielded probe station (Cascade micromanipulator). The data was recorded by the Keithley Interactive Test Environment (KITE) software on the analyzer. DC measurements of the devices were taken in two probe configuration and the devices were biased from -0.5 V to +0.5 V (Figure 3.12). The data was recorded by keeping Ni (bottom electrode) grounded while sweeping the top Cr electrode. Hence for a forward bias, Cr is at a higher potential and for a reverse bias, Cr is at a lower potential. The diodes were probed using tungsten probe tips with 12.5 μm diameter.
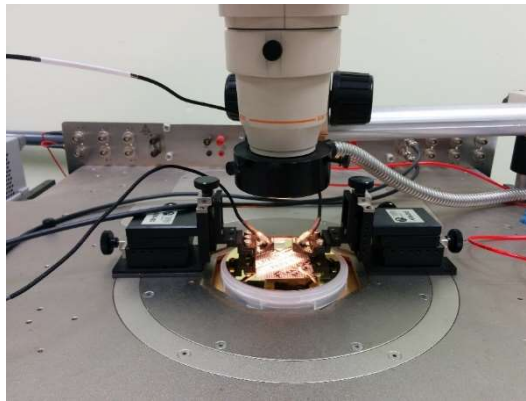


Figure 3.12: Measurement setup for I-V characteristics

#### 3.4.2 RF characterization

Schematic of the experimental arrangement for RF measurements is shown in Figure 3.13. A Keysight N5225A PNA microwave network analyzer was used as the signal source for high frequency measurements up to 50GHz. To minimize signal losses during high frequency measurements, co-planar waveguide (CPW) probes were used with probe pitch of 150 μm. The probes were connected to the waveguide of the PNA module. MIM diodes were fabricated with Cr/Au CPW contact pad with pitch same as that of the probe Figure 3.13. The input signal was fed to the diode through the gold transmission line and the output of the diode was connected to a

high precision Keithley Instruments Inc. (Model 4200). The PNA has the capability to change the input power that can be added to the source signal. The shielded Cascade probe-station was also used for RF measurements.
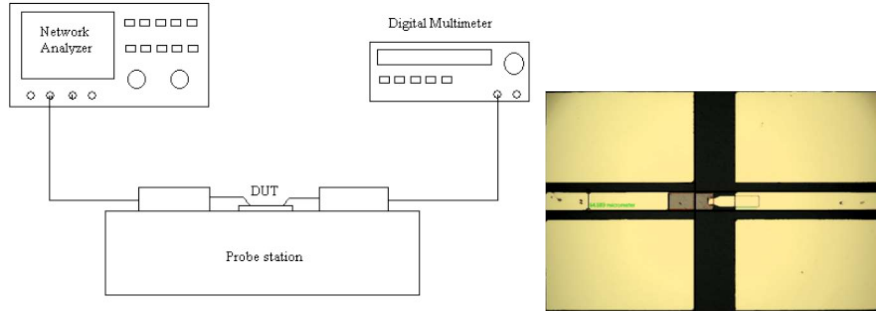


Figure 3.13: Test setup for high-frequency measurements (left) [15]; and MIM with CPW lines (right)

### 3.4.3   C-V characterization

Capactiance-voltage (C-V) measurements were performed using Keithley Model 4200-SCS parameter analyzer equipped with the Model 4200-CVU. The KTEI software was used to extract the parameters. C-V parameters are useful for extracting parameters such as oxide capacitance, oxide thickness, doping density, depletion depth, Debye length, flatband capacitance, flatband voltage, bulk potential, threshold voltage, metal-semiconductor work function difference, and effective oxide charge. The probe station used for this measurement was the same as the one used for I-V and RF measurements. However, to minimize signal losses, special types of probes were used.  The cascade microtech DCP 150R co-axial probes were used for shielded measurements. Schematic of the probe connection is shown in Figure 3.14.
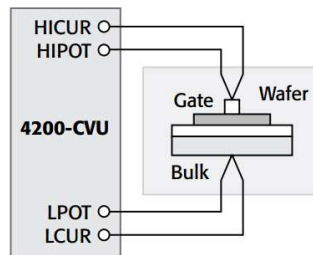


Figure 3.14: Basic configuration to do C-V measurements

## 4. RESULTS AND DISCUSSIONS

### 4.1 Comparison between MIM and MIIM diode

#### 4.1.1    Material characterization

In order to investigate the presence of energy levels and to determine the bandgap Reflectance mode UV-Vis measurements were done on the individual films and the bilayer. Calculated bandgap value of the NiOx was found to be 3.04eV which is consistent with the reported optical bang-gap range of 2.1-3.9eV [86]. While the reported band gap of ZnO at room temperature is 3.37eV [87], the calculated bandgap value of the film in this work was found to be 2.4eV. The lower band-gap can be attributed to the intrinsic defects in ZnO due to the high ratio of interstitial Zn compared to zinc vacancies, oxygen vacancies, and interstitial oxygen in the RF magnetron sputter deposited film [88].  Hall measurements were performed on individual films of thicknesses around 10nm. Results confirmed that the NiOx was p-type with a carrier concentration of $1.832 \times 10^{14}$ cm$^{-3}$ and a resistivity of 94$\Omega$-m. ZnO was n-type with a carrier concentration of $2.32 \times 10^{13}$ cm$^{-3}$, resistivity of 2k$\Omega$-m.

The Focused Ion Beam (FIB) tool "Quanta 3D" with the gallium ion gun was used for thin membrane (lamella) preparation for Transmission Electron Microscopy (TEM) of both devices. High Resolution TEM (HR TEM) was performed in HR TEM Tecnai TF20. For chemical analysis and elements distribution Electron Dispersive X rays Spectroscopy (EDS) and profile scan for each detected elemental was measured. The cross sectional TEM images of the Ni-NiOx-Cr MIM are shown in Figure 4.1 and for Ni-NiOx-ZnO-Cr MIIM diode are shown in Figure 4.2. Results in Figure 4.1(c) and Figure 4.2(c) show the HRTEM images of our MIM and MIIM device layers with the EDS based elements determined. Figure 4.1(a) and Figure 4.2(a) are Selected Electron Diffraction (SAD) of the corresponding areas showing polycrystalline structure of all Au, Cr, NiOx, ZnO, and Ni layers. Figure 4.1(b) and Figure 4.2(b) show the HRTEM cross section of the device at lower magnification to show the smooth and continuous insulator-bottom

electrode interface over an extended range. Further the d-spacing was extracted from the HR-TEM data for each layer to confirm the material and stoichiometry of the dielectrics. The d-spacing of 2.1Å, 2.13 Å, 2.66 Å, and 2.8 Å confirmed the presence of NiO [89], $NiO_2$ [90], and ZnO [91, 92].
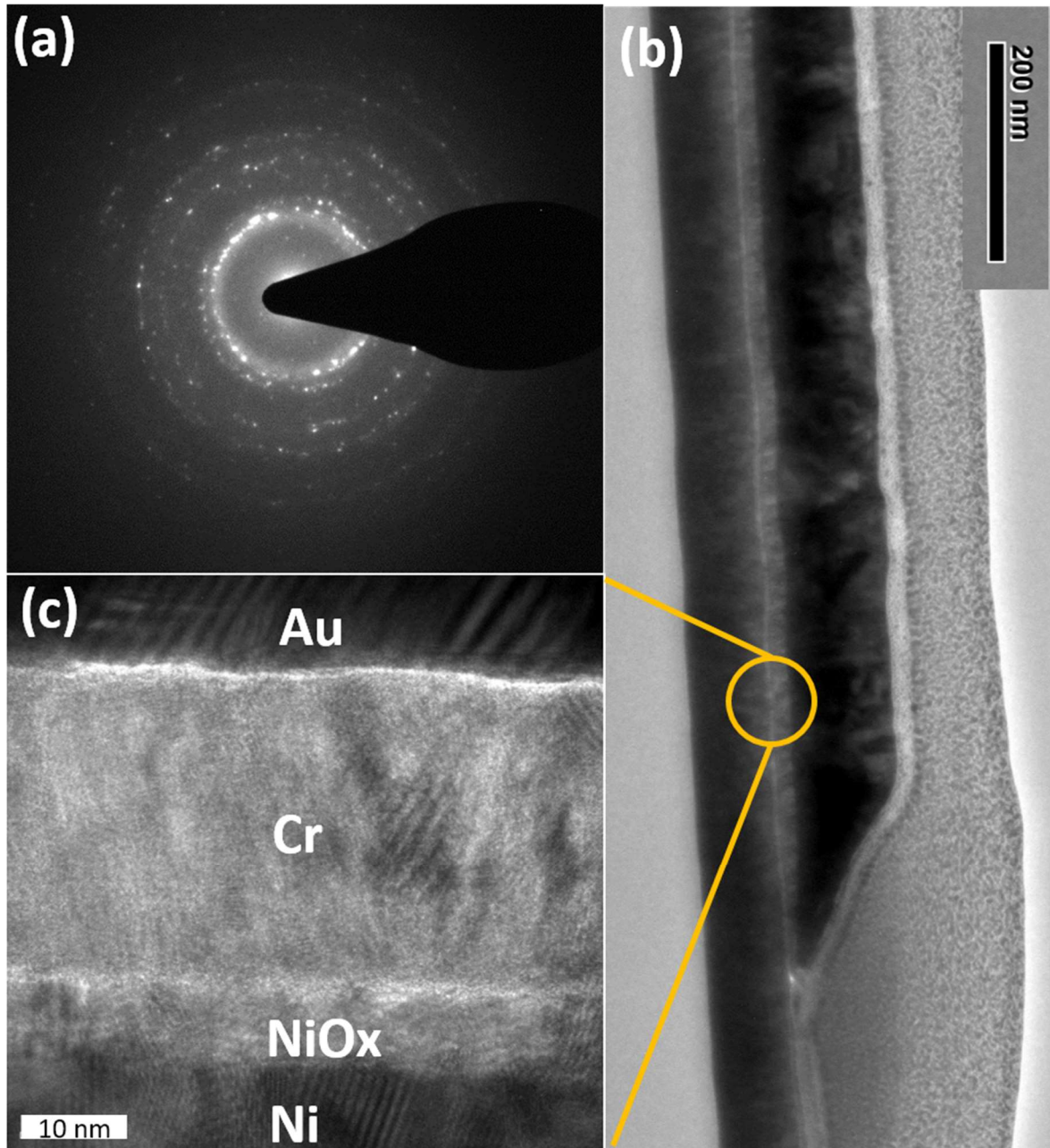


Figure 4.1: (a) SAD, (b) HR TEM of MIM cross section over extended range, and (c) HR TEM of the Ni-NiOx-Cr cross section
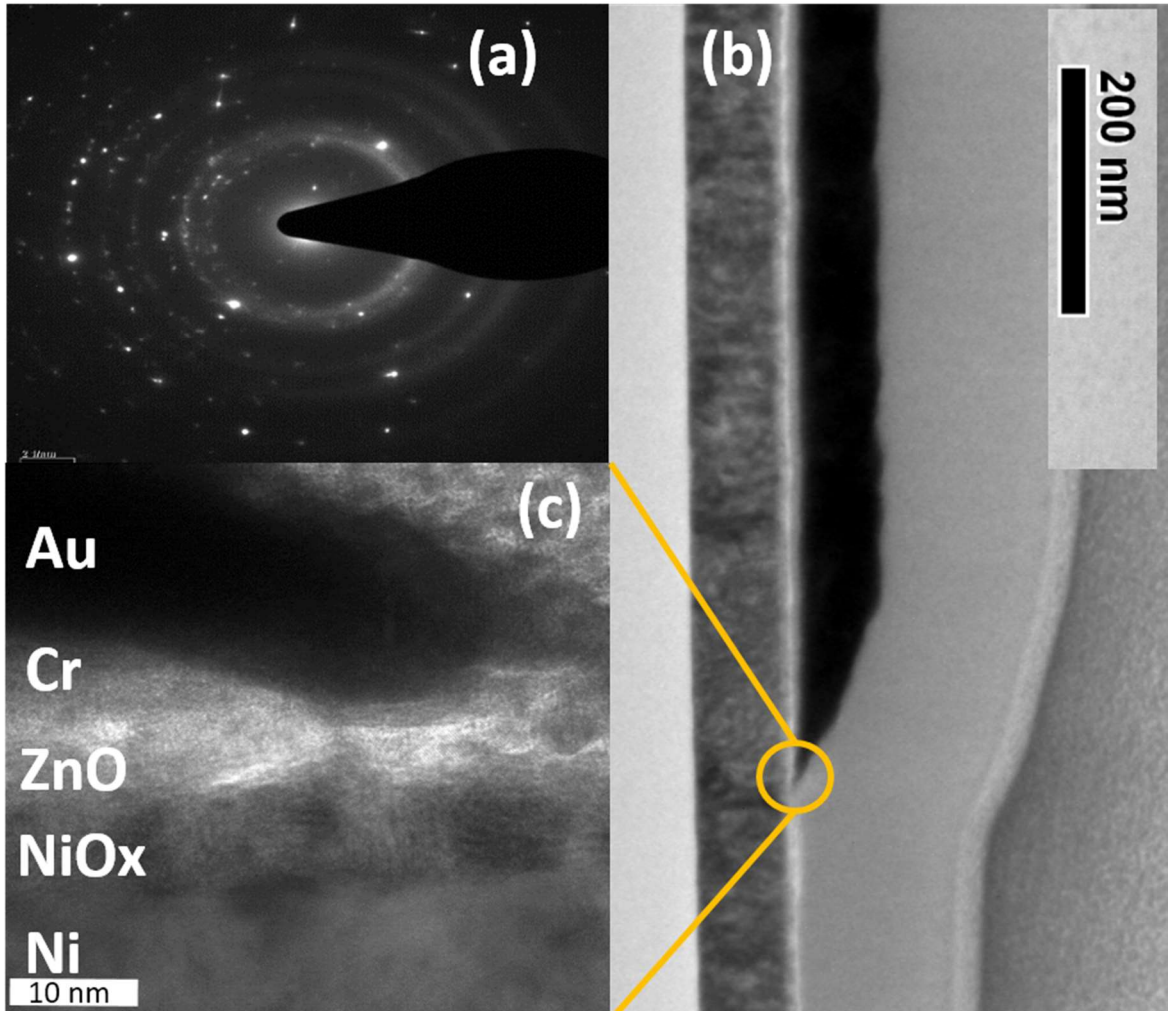
Figure 4.2: (a) SAD, (b) HR TEM of MIM cross section over extended range, and (c) HR TEM of the   Ni-NiOx-Cr cross section

Secondary-ion mass spectroscopy (SIMS) measurements were also carried out to analyze the depth profile of oxygen in the device stack. Figure 4.3 and Figure 4.4 show the depth profile of all the materials (ZnO, NiO, Ni, and Si) in the device stack. The nickel peaks is higher than the insulator peaks, NiO and ZnO.  This does not signify anything but that Ni has a higher secondary ion yield in this matrix.  We also observe a peak in all the elements at the interface, which is a sputter beam artefact.
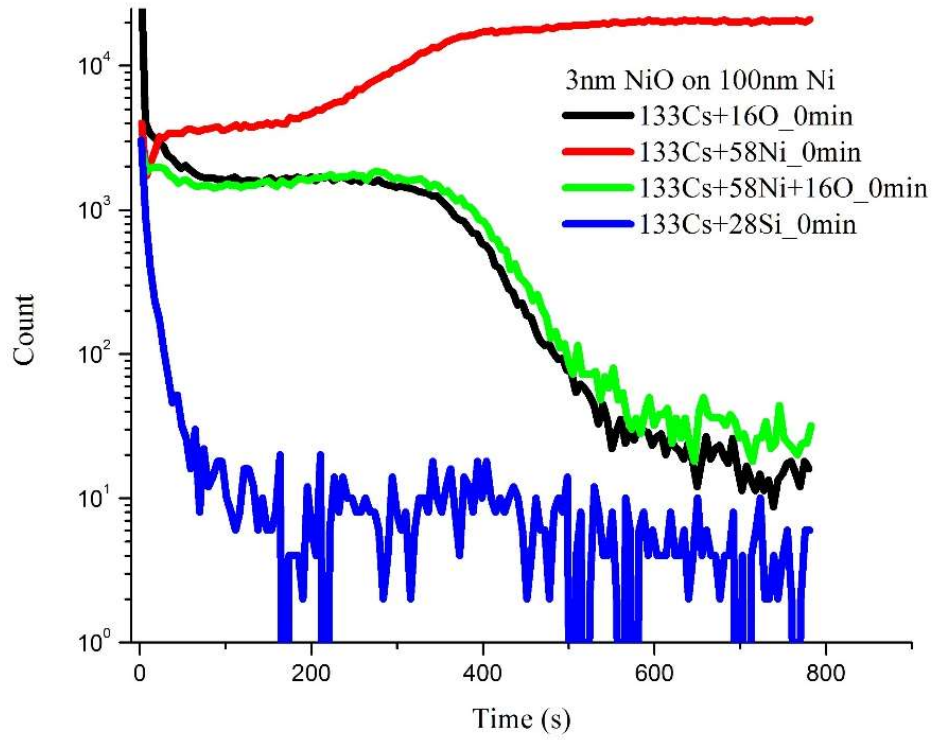
Figure 4.3: Secondary ion mass spectroscopy of MIM diode
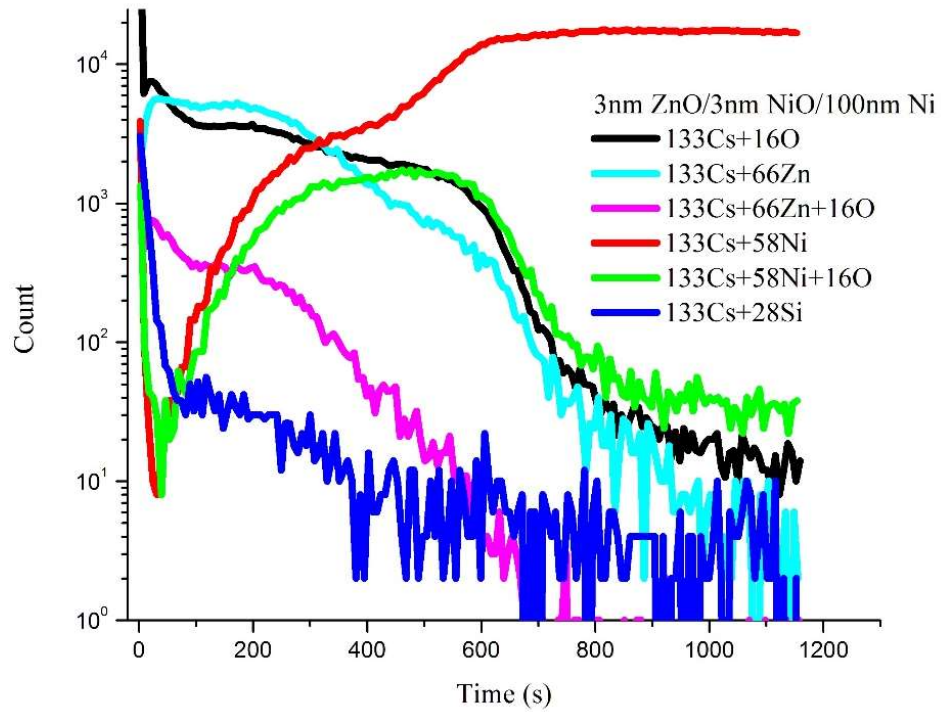


Figure 4.4: Secondary ion mass spectroscopy of MIIM diode

49

### 4.1.2 I-V characteristics

I-V characteristics of single layer NiOx diode and bilayer NiOx/ZnO diode are shown in Figure 4.5 and Figure 4.6 respectively. For each device, the I-V curve (Figure 4.5(a), Figure 4.6(a)) and its first derivative curve (Figure 4.5(b), Figure 4.6(b)) and second derivative curves (Figure 4.5(c), Figure 4.6(c)) are plotted. NiOx diode shows slightly higher reverse bias current than forward bias current. NiOx/ZnO diode exhibits a significant asymmetric and non-linear response under positive bias (Figure 4.6(a)), therefore, implying that resonant tunneling is the dominant tunneling mechanism in this configuration. The turn-on voltage for both diodes is nearly 250 mV. The first derivative, I' =dI/dV, shows the conductivity of the device. The zero-voltage resistance obtained from first derivative curves of single and bilayer dielectric diode is 157 MΩ and 234 MΩ. The bilayer diode has higher resistance since it has nearly twice the insulator layer thickness than the single layer diode. Nonlinearity of the diode is defined by the sensitivity of the diode. Sensitivity of the diode is the ratio of second derivative (I") to first derivative of I-V curve where second derivative implies the rate of change of conductivity. The maximum sensitivity obtained for the single and bilayer dielectric diode is 11 $V^{-1}$ (Figure 4.5(d)) and 16 $V^{-1}$ (Figure 4.6(d)) over an area of 20 μm X 20 μm. The maximum current density of the bilayer dielectric is four times that of the single layer device under forward bias (Figure 4.7(a)). The asymmetry or the normal rectification ratio is the absolute value of the ratio of forward bias current to the reverse bias current. Bilayer diode has an asymmetry of 16 at 0.5V which is significantly more than that of NiOx diode (Figure 4.7(b)). NiOx diode has an asymmetry of slightly more than 1 at -0.5V. This is due to the slightly larger reverse bias current than the forward bias current. These results can be interpreted by taking the energy-band diagram of the device into consideration.
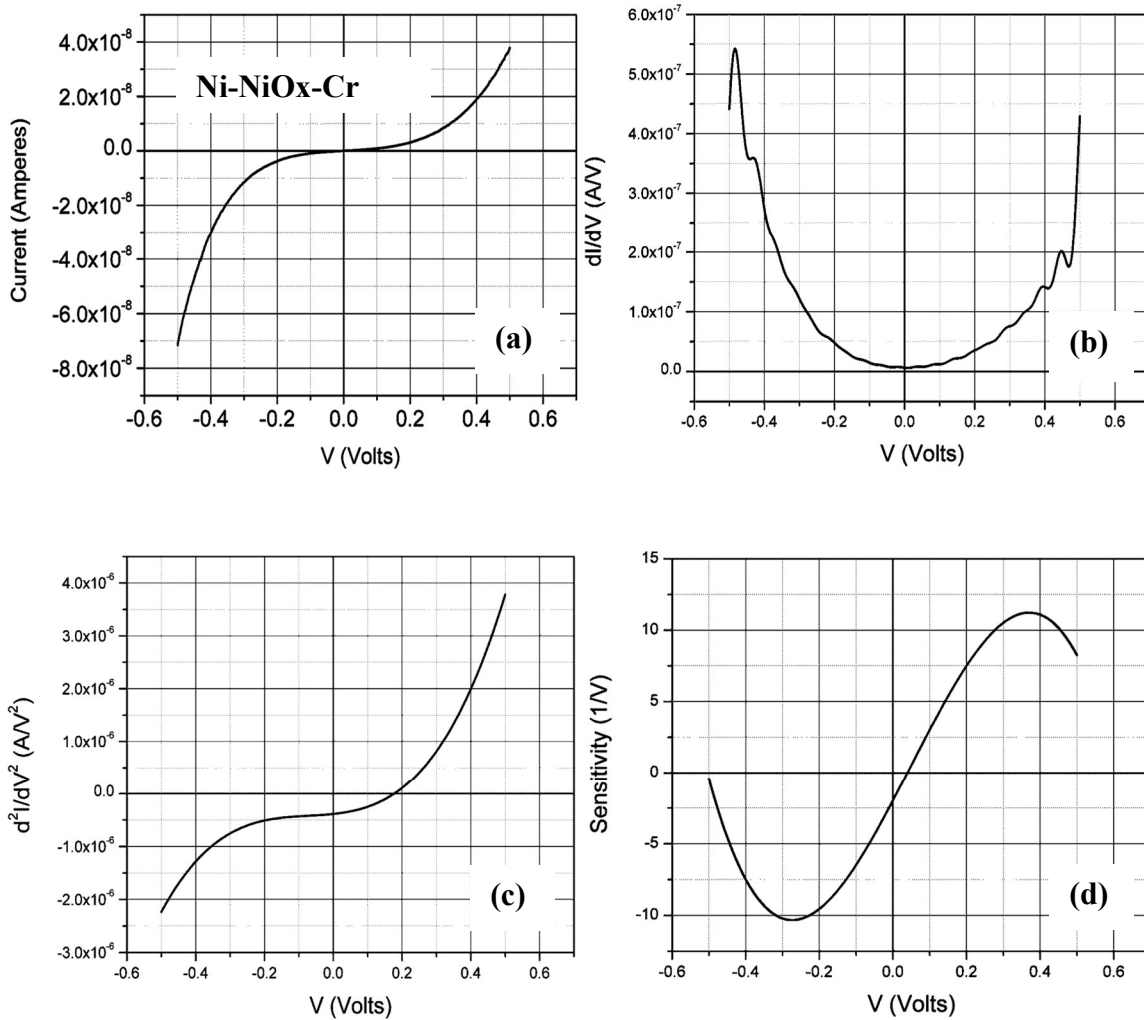
Figure 4.5: Ni-NiOx-Cr diode: (a) I-V (b) first derivative (c) second derivative (d) sensitivity
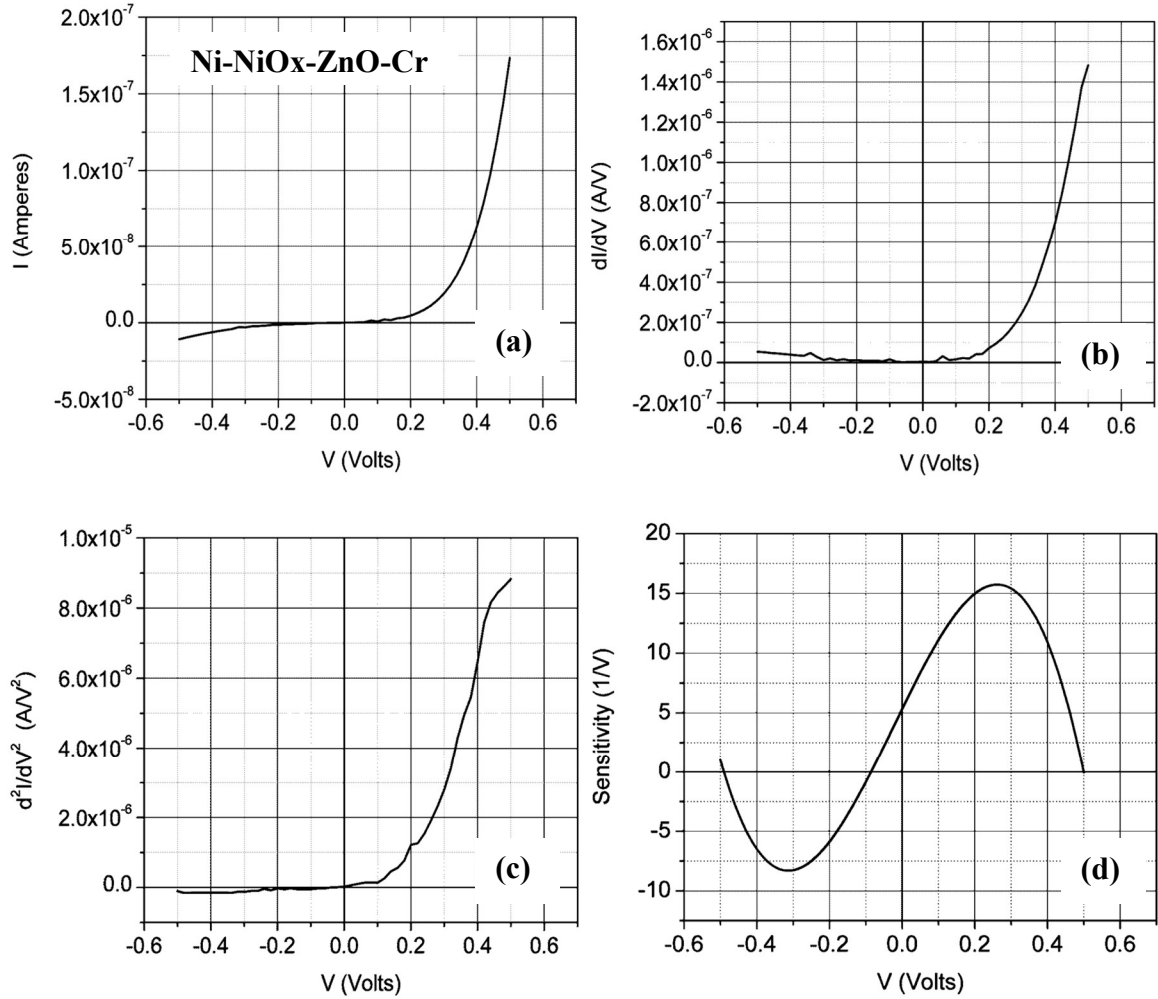
Figure 4.6: Ni-NiOx-ZnO-Cr diode: (a) I-V (b) first derivative (c) second derivative (d) sensitivity

Asymmetry in the tunnel diodes can be achieved by using dissimilar top and bottom metal electrodes. The difference in the work function of the metals $\Delta\Phi$ provides a barrier height at zero bias. Therefore, the MIM diode with dissimilar metal electrodes has significantly higher chances of tunneling at zero bias than diode with identical electrodes. Previously, Choi et al. fabricated NiO/ZnO MIIM diode with identical metal electrodes and it displayed symmetrical I-V characteristics [93]. Thus in this work, nickel was chosen as the bottom electrode only and chromium was chosen as the top electrode. Chromium also acted as the adhesion layer for the gold contact pad. The work function difference between the metals was much higher than the

required difference of 30 meV [94] to set the nonlinearity. A MIM diode is forward biased when the metal with lower work function (Cr) is at a higher voltage than the metal with higher work function (Ni).
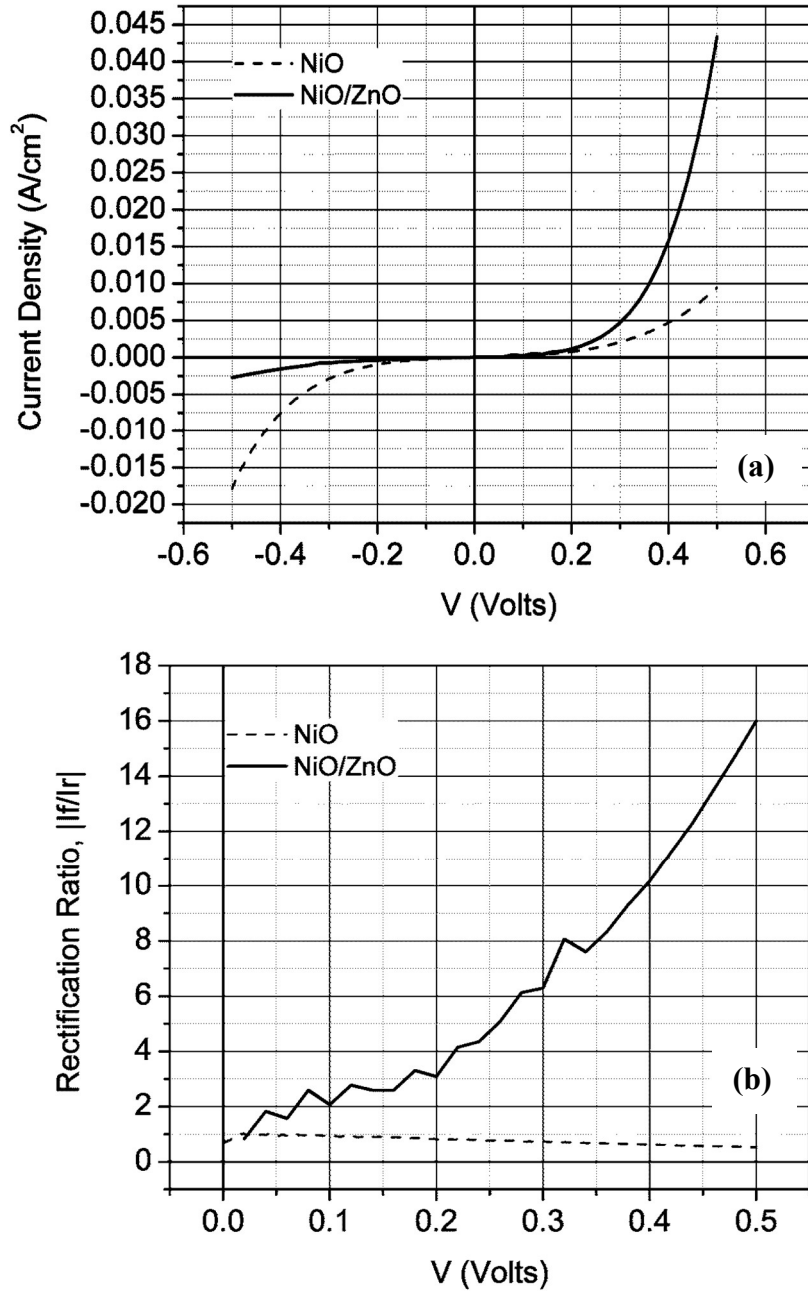


Figure 4.7: Comparison of (a) Current density and (b) Rectification ratio of single and bilayer dielectric tunnel diodes.

### 4.1.3    Theoretical I-V characteristics

The property of the insulator greatly influences the asymmetry of the device. Tunneling probability of the electrons increases with the decreasing insulator thickness but at the cost of asymmetry and non-linearity [17]. The small variations in thickness of the insulator can cause large fluctuations in the MIM tunnel diode behavior. The effective or approximate dielectric thickness (S) and mean barrier height ($\Phi$) in MIM diodes can be estimated by Simmons equation (equation 3) in [48]. The current density (J) according to Simmons equation is given by [48] as:

$$J = \left(\frac{6.2 \text{X} 10^{10}}{S^2}\right)\left[\left(\phi \cdot e^{-1.025 \cdot S \cdot \sqrt{\phi}}\right) - \left((\phi + V) \cdot e^{-1.025 \cdot S \cdot \sqrt{\phi + V}}\right)\right] \tag{4.1}$$

The mean barrier height $\Phi$ is $(\Phi_1 + \Phi_2 - V)/2$ in equation 4.1 where $\Phi_1$ is the barrier height between bottom electrode and insulator and $\Phi_2$ is the barrier height between top electrode and insulator. Expected values of $\Phi_1$ and $\Phi_2$ are 4.55 eV and 3.9 eV due to the relation $\Phi = \psi - \chi$, where the work functions, $\psi$, of Ni and Cr are 5.15eV and 4.5 eV and the electron affinity $\chi$ of NiOx ~0.6eV [95, 96]. Therefore the expected barrier height difference is ~0.65eV. The Simmons current density equation was fitted to the measured data starting with the expected thickness and barrier height values. However, the fitted values for $\Phi_1$, $\Phi_2$, and S were extracted to be 0.4eV, 1.03eV, and ~3nm. The fitted barrier height difference of 0.63eV corresponds to the difference of the expected barrier heights. The zero bias resistance of 157 M$\Omega$ at a barrier height of 0.63eV for our single insulator diode with an effective barrier thickness of 3nm is consistent with the theoretical data depicted in Figure 4(b) of [19]. The reduced barrier lowering of $\Phi_1$ and $\Phi_2$ can be explained by image charge forces which are not considered in the theoretical equation. The image charge forces are built up in the metal electrode due to the charge carriers approaching the metal-insulator interface. The potential associated with these charges cause the rounding of the barrier edge hence barrier lowering. The effective barrier thickness of 3nm across the 20μmX20μm contact area is lower than the targeted thickness of 7nm. This kind of variation is expected in such

comparatively large contact junctions. The theoretical fit to the measured J-V curve of the MIM diode is shown in Figure 4.8.
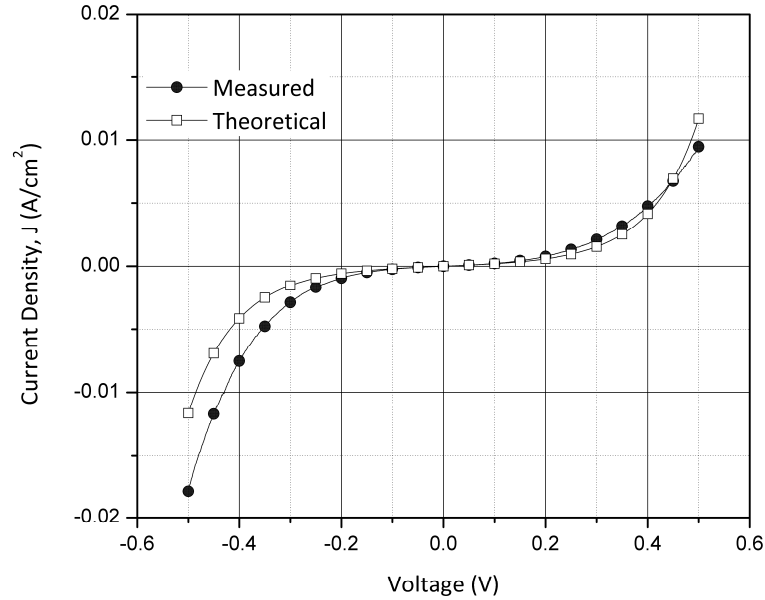


Figure 4.8: Simmons Curve Fit to J-V characteristics of Ni-NiOx-Cr diode

The MIM properties for rectification can be enhanced by choosing a bilayer dielectric configuration, MIIM [19, 97]. Depending on the height and width of the barrier the electron can either resonate within the barrier, tunnel or hop the barrier. A MIIM diode's enhanced performance can be explained by resonant tunneling [98] and step tunneling [97]. Both can occur in the same device at opposite bias arrangement. From the approximated bandgap values of NiOx and ZnO obtained from UV–Vis measurements, the energy band diagram of the bilayer tunnel junction of the Ni/NiOx/ZnO/Cr stack in this work can be assumed to be as shown in Figure 4.9. Under forward bias, formation of a quantum well between the two insulators allows resonant tunneling to occur. When the energy of the electrons resonates with the quantum well's lowest energy level it results in large current flow. Under negative bias, when Cr is at a lower potential than Ni the barrier height increases. Due to the bias, the NiOx and ZnO p-n junction is also reverse biased, hence supporting the increment in barrier height. There is no quantum well

formation under negative bias but the tunnel distance reduces abruptly for the electrons due to the increased barrier height and reduced barrier width.
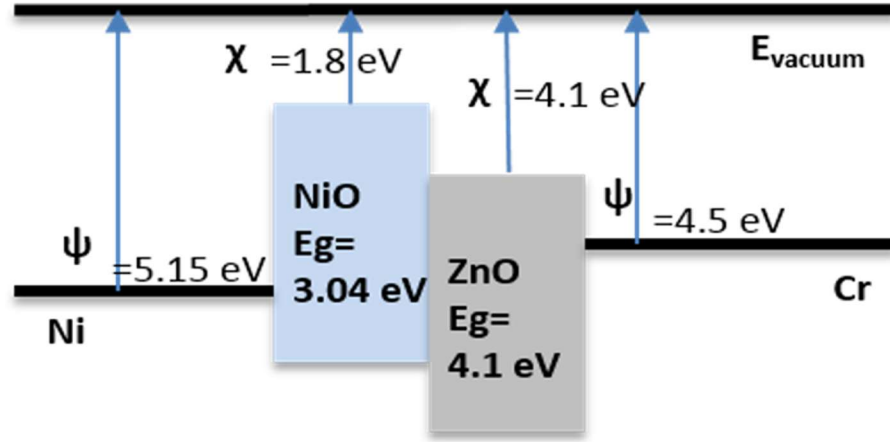


Figure 4.9: Energy band diagram of Ni-NiOx-ZnO-Cr tunnel diode.

As evident from Figure 4.6(a), the dominant tunneling mechanism is due to resonant tunneling in the forward bias. The tunneling can be either direct or trap assisted. We fitted our measured I-V data to Fowler-Nordheim (FN) model [99] and Trap Assisted Tunneling (TAT) model [100] to identify which tunneling mechanism was occurring in our MIIM diode. The electrical properties of the oxides are highly affected by the presence of the defects which can induce electronic states in the band gap. These electronic states can either trap electrons or assist in tunneling of the electrons. The current density relation due to trap-assisted tunneling at high fields is governed by equation (8) in [100]:

$$J_{tat} \propto e^{[\frac{-8\pi\sqrt{2qm*}\Phi^{3/2}}{3hV}]} \tag{4.2}$$

Here m* is the effective mass of the electron and h is the plank's constant. Figure 4.10(a) shows the TAT fit for MIIM diode at higher voltages in the ln(J) as a function of 1/V plot. The current J is in A/cm$^2$ and V is the applied bias. The fitted $\Phi$ for MIIM diode was 0.655eV which is in agreement with the expected barrier height value. Figure 4.10(b) shows the FN fit of the

MIIM diode on a $\ln(J/V^2)$ as a function of $1/V$ plot at higher voltages since FN tunneling is dominant at higher electric fields. It is governed by equation 22 in [101] and simplified in [99] as:

$$J_{FN} = CV^2 e^{-\frac{B}{V}} A/cm^2 \tag{4.3}$$

where $C=\frac{mq^3}{8\pi h m^*\Phi}$ and $B=\frac{8\pi\sqrt{2m^*}\Phi^{3/2}}{3h}$. The fitted curve gives an unreasonably low barrier height which confirms that FN tunneling is not possible under forward bias at low fields for our proposed MIIM diode. Therefore, trap assisted tunneling is the dominant tunneling mechanism under forward bias in our Ni-NiOx-ZnO-Cr diode.



Figure 4.10:(a)

57
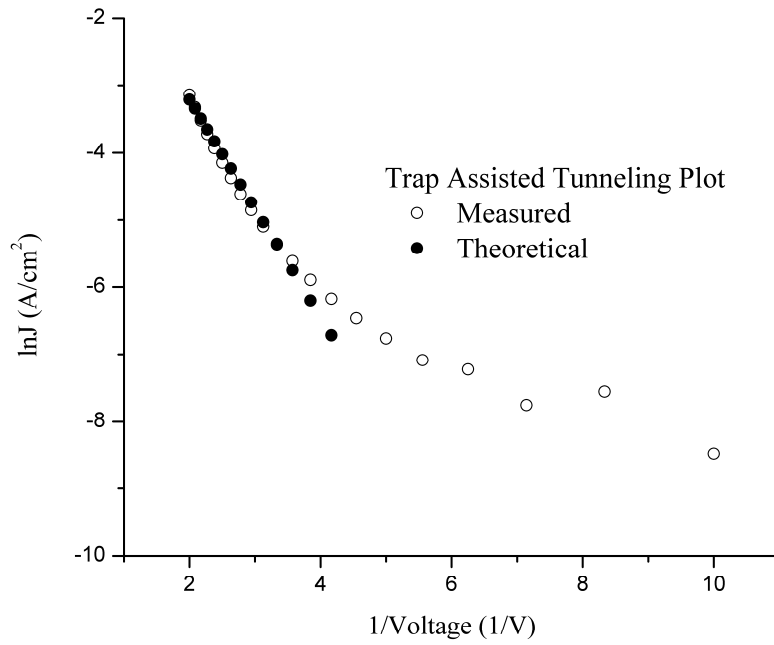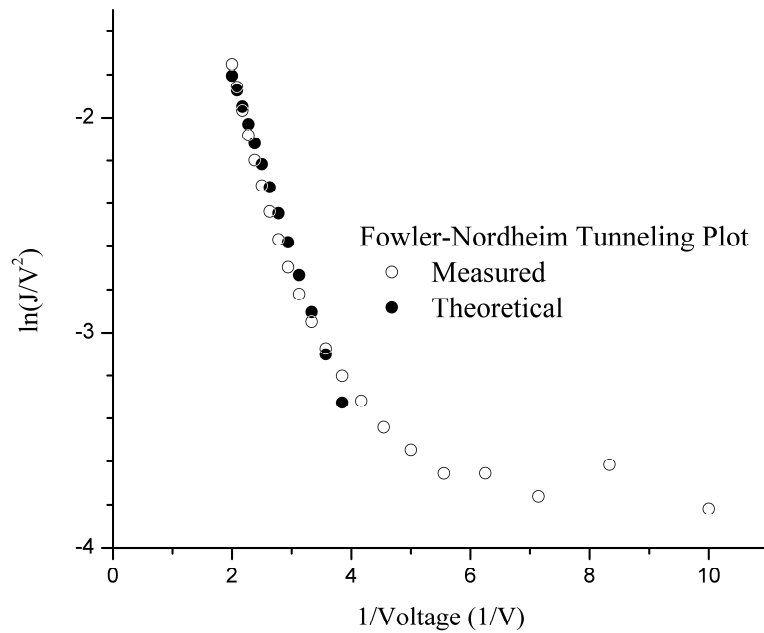
Figure 4.10:(b)

Figure 4.10: (a) TAT fit (b) FN fit to Ni-NiOx-ZnO-Cr diode characteristics

### 4.1.4    Zero bias resistance and C-V characteristics

Following the I-V measurement of MIM and MIIM diode, a MIIM diode with a reduced junction thickness of 6nm (3nm NiO and 3nm ZnO) was also fabricated. It was essential to further explore a MIIM diode with thinner $NiO_x$/ZnO junction, since it exhibited I-V characteristics with a high asymmetric ratio of 16 as compared to the MIM device. A reduced junction thickness was hoped to reduce the overall resistance of the diode while still maintaining the high asymmetry. The zero bias resistance of the various diode structures was determined.

Figure 4.11 shows the distribution of zero bias resistances. Diode resistances are in the range of few hundred MΩ and tens of MΩ for 14nm MIIM and 3nm MIM diodes.  Upon decreasing the thickness of the MIIM junction thickness to 6nm, the resistance drops significantly to a few hundred ohms, which is even less than that of 3nm MIM diode. Similar

MIIM diode structures were fabricated with ALD deposited ZnO instead of sputter deposited for a more uniform bilayer insulating stack. The resistance was found to be in the range of tens of kΩ. The change in resistance can be due to the change in physical properties of the ZnO layer due to the different deposition techniques.

Figure 4.12-Figure 4.14 show the asymmetry and sensitivity of the four diode structures with targeted area of $16\mu m^2$. The 14nm MIIM diode exhibits the maximum asymmetry and sensitivity. Sensitivity increases from 3nm MIM to 6nm MIIM diodes. Asymmetry is comparable for the 3nm MIM and 6nm MIIM diodes. However, slope of the asymmetry curve of 6nm ALD MIIM diode is negative. This implies that the reverse bias current is larger than the forward bias current. RF characterization is performed using these devices and results are presented in the next section.
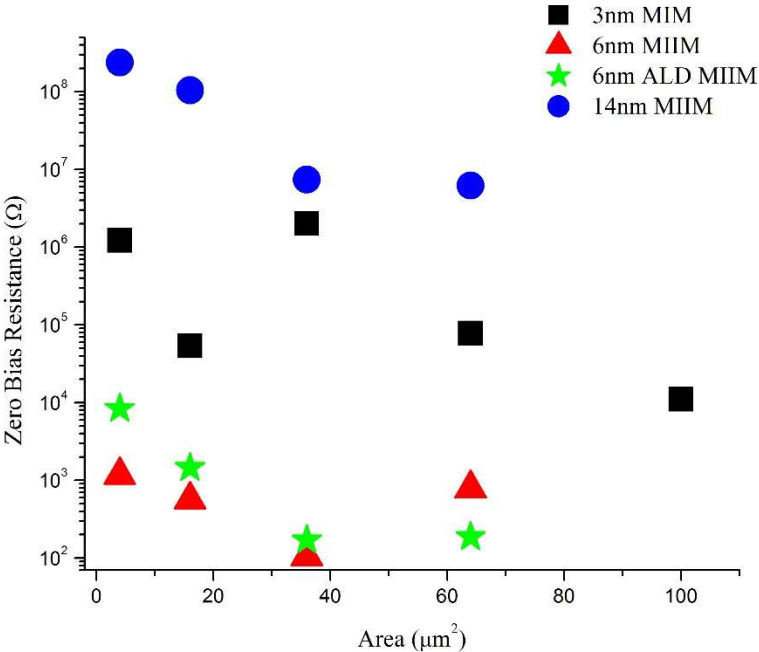


Figure 4.11: Distribution of zero-bias resistance of various diode structures

Capacitance-voltage measurements were performed to determine the capacitance of the devices with respect to area, as shown in Figure 4.15. The capacitance values for the 3nm MIM

and 6nm MIIM are comparable for devices with area less than 100 $\mu m^2$. Capacitance of 6nm MIIM diode is slightly less than that of 3nm MIM due to difference in effective oxide thickness. The same can be said in the case of 14nm MIIM diodes which exhibit the minimum capacitance value. For larger devices (>100 $\mu m^2$), 6nm ALD MIIM structures show the maximum capacitance. Again, this can be explained by the variation in physical properties of the two ZnO films. I-V and C-V measurements of the MIM and MIIM devices were also carried out in the temperature range of 3K-268K. As the temperature decreased, the current values also decreased. The ln(I) vs 1000/T curve for a 6nm MIIM diode can be seen in Figure 4.16. The capacitance dependency on temperature is depicted in Figure 4.17. Capacitance increases, almost linearly, with temperature.
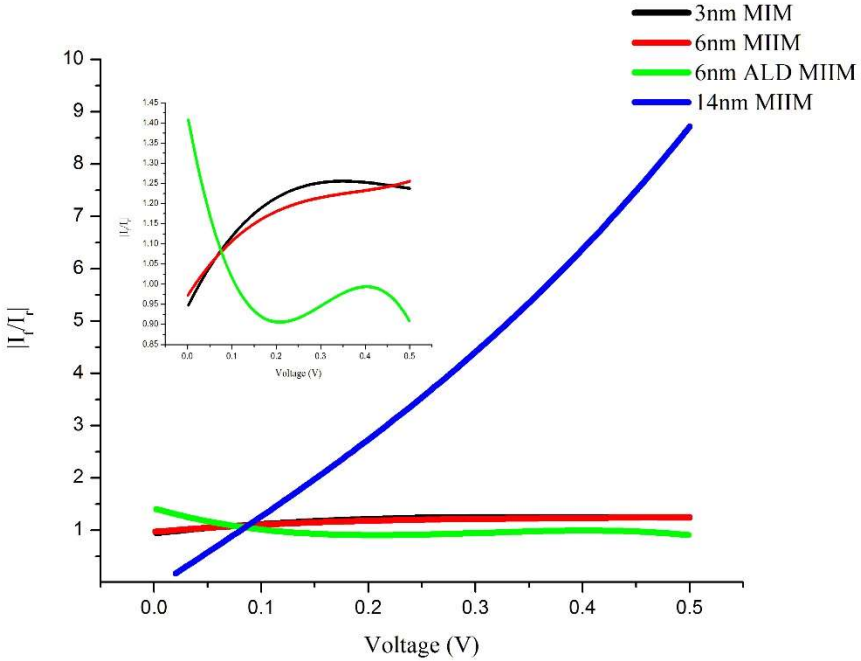


Figure 4.12: Current asymmetry of various diode structures
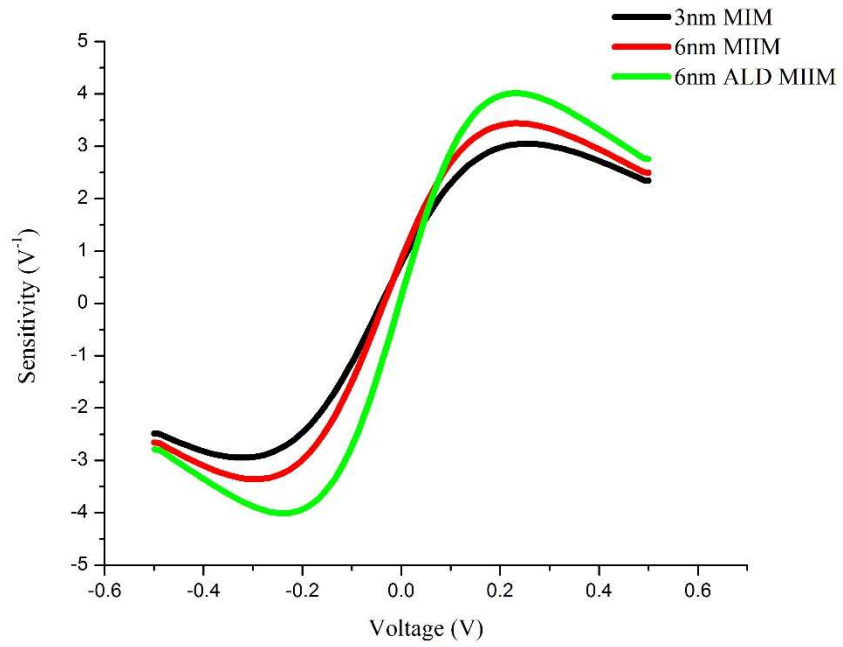
Figure 4.13: Sensitivity of various diode structures
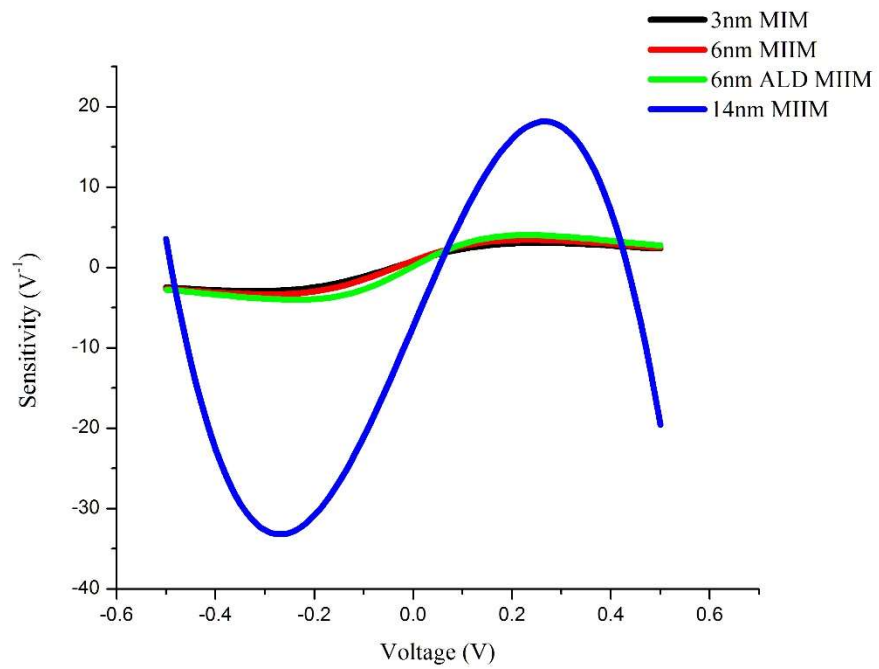


Figure 4.14: Sensitivity of various diode structures in comparison to 14nm MIIM diode

61
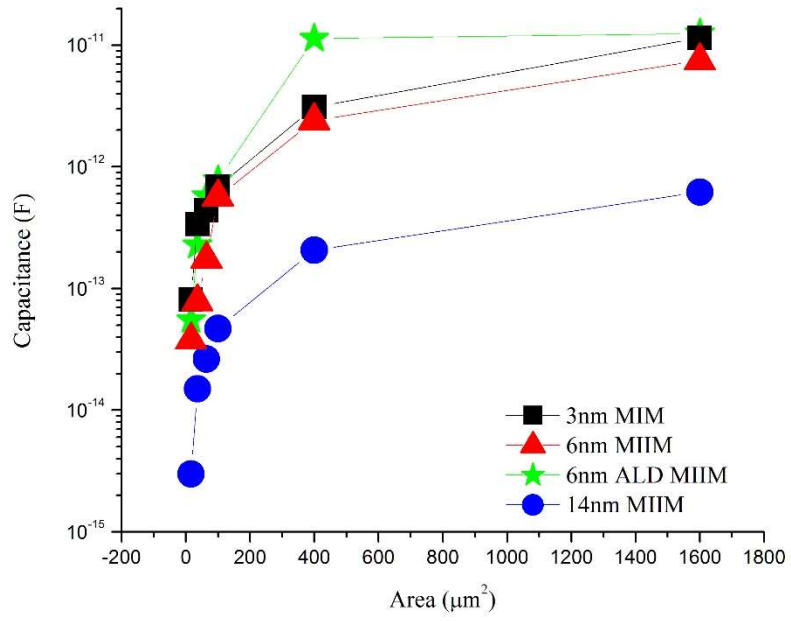
Figure 4.15: Capacitance-voltage of various diode structures
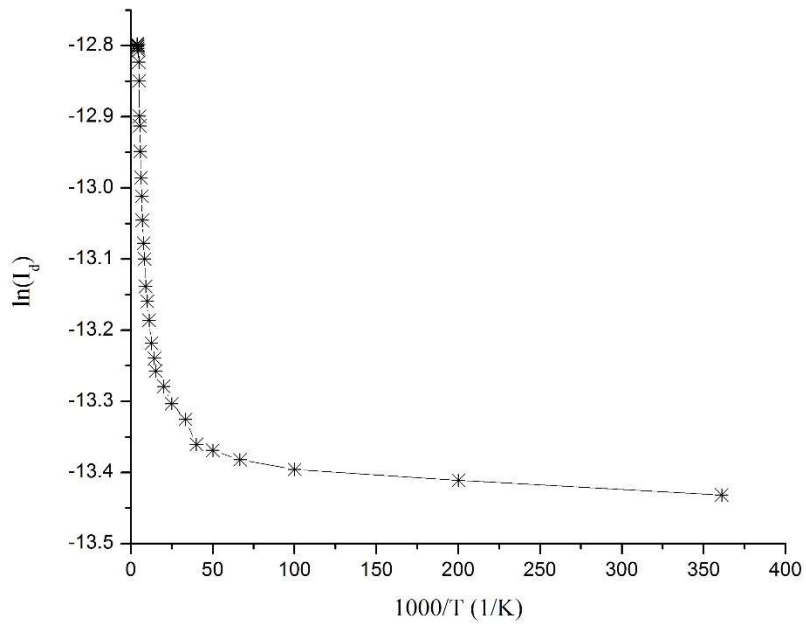


Figure 4.16: ln(I) vs. 1000/T response of a MIIM diode in the 3K-268K temperature range
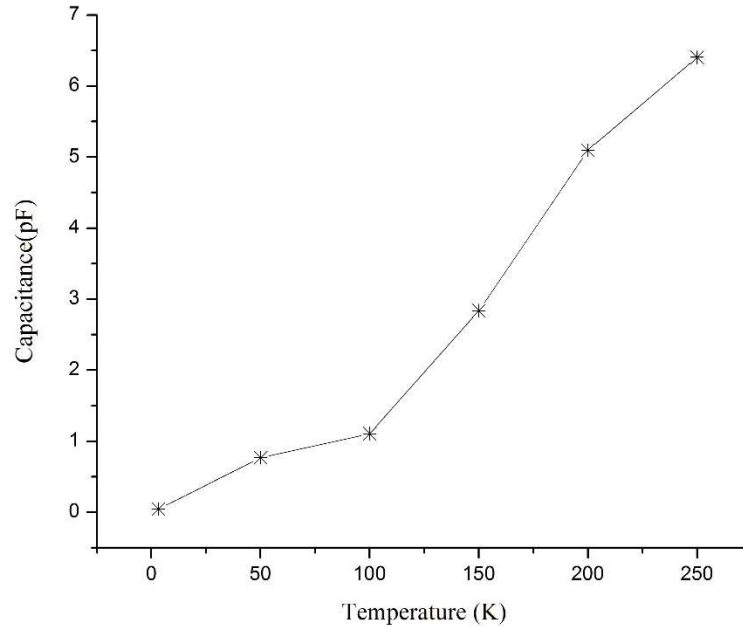
Figure 4.17: Capacitance-temperature (3K -268K) characteristics of a MIIM diode

### 4.1.5 RF characterization

The MIM diodes fabricated on silicon substrates were used for 50 GHz measurements. Keysight N5225A PNA microwave network was used for the diode testing. After the on-wafer calibration was performed, the probes were moved to the edge of the diode contact pads and gently placed to make a good contact. A 50 GHz signal with a 0 dBm power (1 mW) was given as an input to the MIM diode using the PNA as a continuous signal generator. The diode was connected to a multimeter to record the output current. When the input signal was provided, the diodes responded positively and output current was measured in the multimeter. The current recorded was predominantly in the order of low μA. The amplitude and Vp-p was not noted since, the PNA was not hooked up to an oscilloscope, which is the only way of knowing the input voltage. Due to the unavailability of a high frequency oscilloscope, the amplitude of the input signal could not be observed.

The RF power was varied from -10 dBm to 10 dBm and the corresponding current was measured for a MIM diode. Figure 4.18 shows the variation in current with input RF power. As can be seen from Figure 4.18, all the diodes exhibited the same trend of increase in current with increase in RF power. To measure the reflection coefficient or the return loss of the MIM diodes, the S11 and S21 pattern of the diodes were measured. The on-chip calibration standards were initially calibrated, and then using the two-port configuration the return losses and transmission were measured. Figure 4.19-Figure 4.21 show the return loss in the 25MHz to 50GHz frequency range for different diode structures: 3nm MIM, 6nm MIIM, and 14nm MIIM. It is observed that 6nm MIIM diodes exhibit higher return losses and low transmission than 3nm MIM. Typically, a perfectly matched device will have very low return loss approaching - ∞. This suggests that the diodes are rejecting a large part of the incident signal that is transmitted through the lead lines. This can be resolved by providing a matching network between the transmission line and the diode or by developing the diode with much less resistance. But, in order to achieve maximum efficiency, a matching network would be preferred.
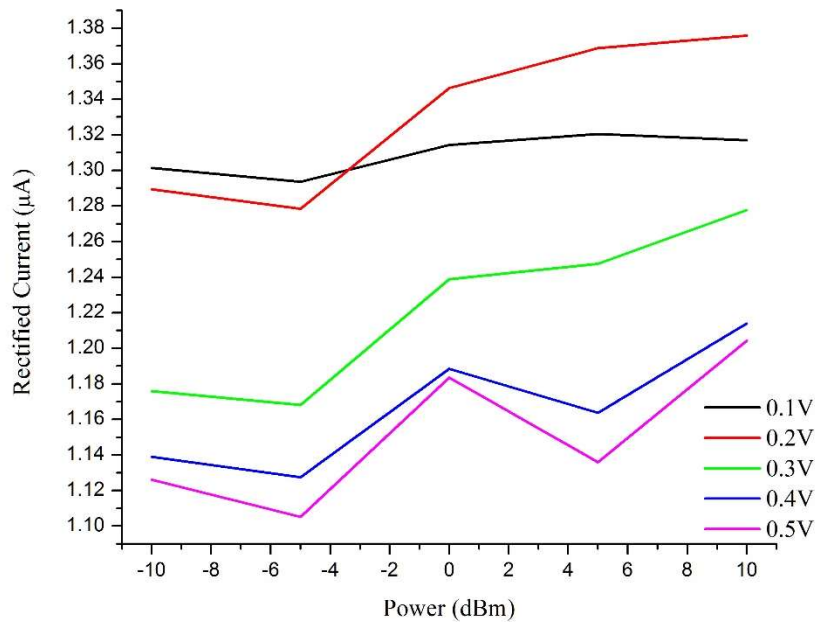


Figure 4.18: Variation in DC current with change in input power

Figure 4.22 shows the distribution of current recorded for 3nm MIM and 6nm MIIM diodes at different positive bias upon feeding a 50 GHz signal for 3nm MIM, 6nm MIIM, 6nm ALD MIIM and 10 GHz signal for 14nm MIIM diode. From the distribution it can be seen that the diodes exhibit maximum current near 0.2V which is where the diode's sensitivity was found to be maximum. From the AC measurements it can be noted that the current was in the same range as the DC I-V measurement for 3nm MIM and 14nm MIIM diode, however the rectified current values for 6nm MIIM is significantly less. This could be due to the low transmission ratios. The accurate comparison of the devices is only possible with a matching network between the transmission line and the diode for impedance matching. Although the diodes displayed acceptable level of output current, when considering the efficiency, the diode performance is on the lower side. At 0 dBm or 1mW input power, and no external bias the diodes yielded a maximum of 100 nA with kohms resistance. The efficiency ($\eta$) of a device can be defined as the ratio of output power to the input power. Hence the efficiency was determined to be <1% for MIIM diodes. As mentioned earlier, a matching network would be preferred in order to achieve maximum efficiency.
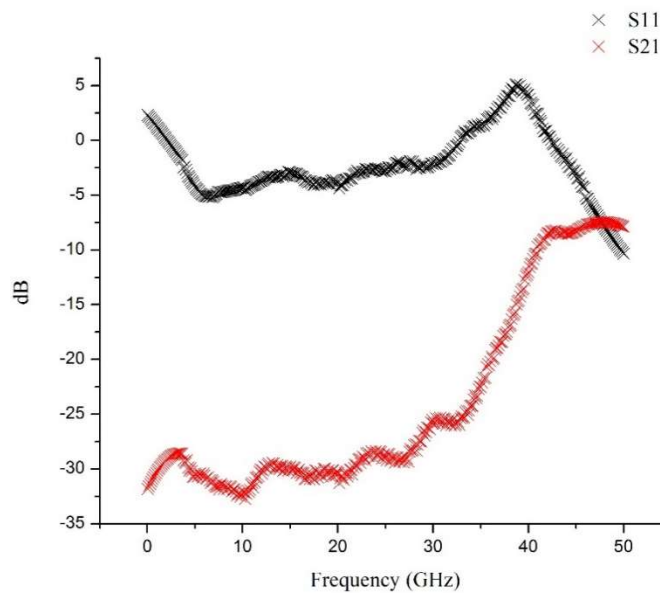


Figure 4.19: S11 and S21 response of 3nm MIM diode in 25MHz – 50GHz frequency range
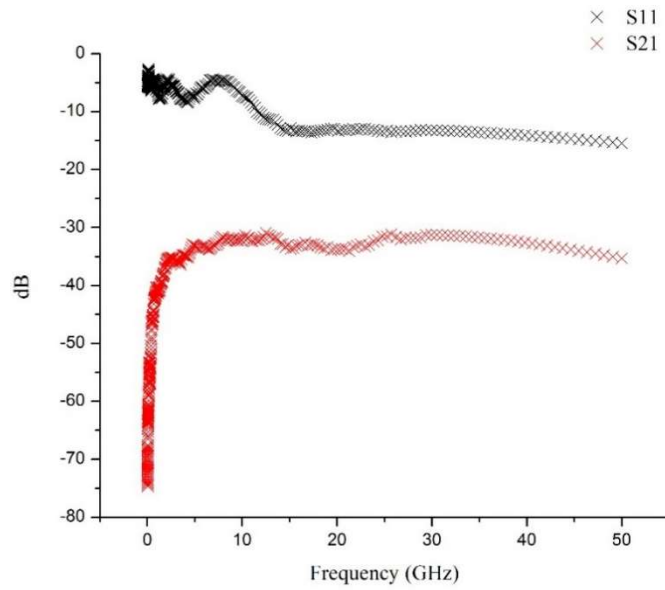
Figure 4.20: S11 and S21 response of 6nm MIIM diode in 25MHz – 50GHz frequency range
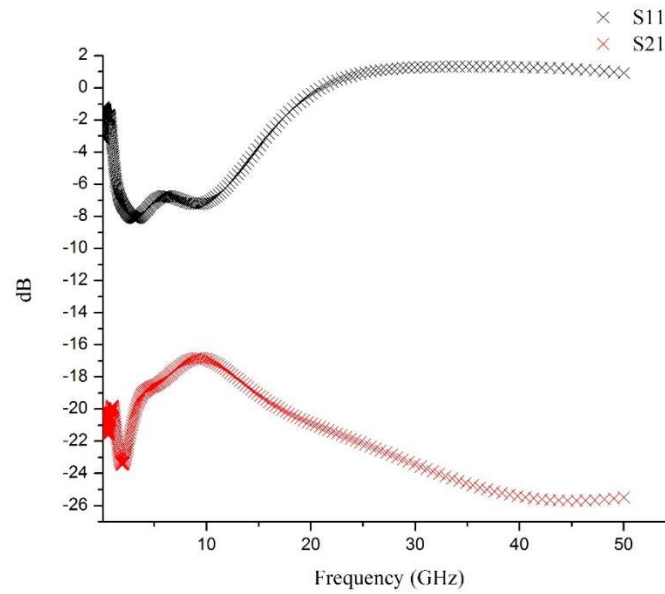


Figure 4.21: S11 and S21 response of 14nm MIIM diode in 25MHz – 50GHz frequency range
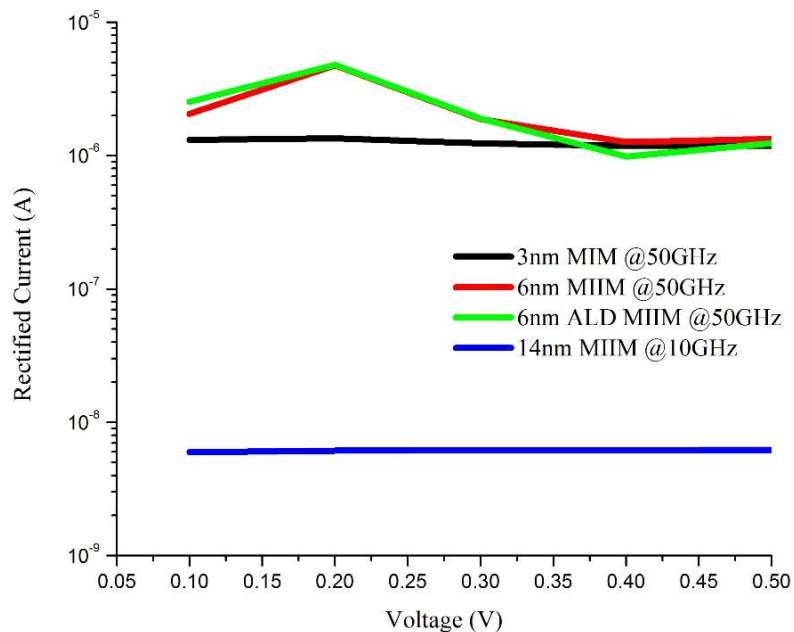
Figure 4.22: Output current response of MIM and MIIM diodes when subject to RF signal

Thus the experiment provides evidence of AC to DC conversion in spite of the issues. In summary, the diodes when subjected to 50 GHz signal yielded about μA current output as exhibited from the rectified current response. However, when the diode was operated at a lower frequency, did not display any rectification like behavior. This might be because the diodes were designed for high frequency operation and hence the frequency mismatch causes the diode not to demonstrate rectification characteristics.

### 4.1.6 Conclusions

In summary we report fabrication of bilayer Ni-NiOx-ZnO-Cr MIIM diode and its I-V characterization. MIIM diode with sputter deposited NiOx/ZnO bilayer insulators exhibited significant asymmetry and nonlinearity when compared to the MIM diode. The sputter deposited MIIM diode had an asymmetry of 16 at 0.5V which is comparatively larger than most atomic layer deposited diodes reported in literature. The maximum sensitivity of the NiOx/ZnO diode was 16 $V^{-1}$. It was also shown that resonant tunneling dominates via trap-assisted tunneling mechanism in the bilayer dielectric diode. For further reduction of the diode resistance, diodes

with 6nm NiOx/ZnO junction thickness were fabricated. ZnO was deposited by two different techniques: Sputtering and ALD for diode performance comparison. Both 6nm sputtered and ALD MIIM diode exhibited similar characteristics. The asymmetry was compromised on reduction of the oxide thickness but the diode resistance was dramatically reduced. This suggests exploration of NiOx/ZnO structures with n:1 NiOx:ZnO thickness ratios where p-type NiOx has higher thickness than n-type ZnO. To conclude, p-n junction MIIM diodes have demonstrated potential for high-frequency rectification.

## 4.2  Analysis of inhomogeneous NiOx thin films

For measurements made on films of different thicknesses, the twisted curves in three-dimensional ($n$-$k$-$d$) space do not intersect; however, their projections onto the $n$-$k$ plane do. If the film optical properties remain constant in the growth direction, all measurements result in curves which intersect at or near a vertex in the $n$-$k$ plane. The films reported here do not result in a vertex. Instead, pairs of measurements intersect at different $n$-$k$ values which exhibit a monotonic shift across the n-k plane with increasing film thickness. This supports our conclusion that the films are not homogeneous in the growth direction. The mathematics for multiple layers in the n-k plane analysis method is fully described in the work of Urban and Barton [81].

Figure 4.23 shows four solution curves corresponding to measurements made on four different thicknesses of $NiO_x$ films deposited on silicon substrates by reactive magnetron sputtering. Measurements were made at 370 nm light wavelength. The figure displays plots of the n-k plane projections of the overall film three-dimensional n, k, and d solutions which satisfy the measurements and models of unknown films on a silicon substrate. The value of film thickness, d, is parametric in these curves, being the smallest on the left end of each curve and increasing to the right and upward. The blue curve (a) corresponds to the thinnest film and the green (b), red (c), and black (d) curves, correspond to films of increasing thickness. Note that the four curves

give rise to three distinct n-k plane intersections marked with black dots. Each intersection

indicates a single value of film n and k and two values of thickness which is different on each of

the curves at the intersection. No amount of adjustments of the film overlayer or underlayer could

bring all three black dots into a sharp vertex.  This is in contrast with the case of a vertically

homogeneous film for which a very sharp vertex could be formed [82]. Thus the plots in the

figure indicate vertical inhomogeneity in which the film index, n, and extinction coefficient, k,

both decrease with increasing film thickness from (a) to (d). The locations of the intersections of

adjacent curves are used primarily as a way to determine the film thicknesses.



Figure 4.23: This figure shows four solution curves for NiOx films deposited for (a) 10 min., (b) 15 min., (c) 20 min., and (d) 30 min. Measurements were made at 370 nm light wavelength.

Figure 4.23 also shows that adjacent solution curves intersect at relatively small angles.

The consequence of this is that the location of the intersections is quite sensitive to measurement

accuracy. A small shift in the location of either of the solution curves due to measurement

accuracy will move the intersection significantly. It would be better to employ measurements that

wavelengths for which the intersections are more perpendicular, that is closer to 90° than to 0°.  It

is also instructive to note that an intersection corresponding to a greater difference in thickness, (a) intersection with (d) for example occurs at a larger than those closer in thickness. Thus there is a tradeoff between the thickness resolution of the measurements and the accuracy of the solutions.
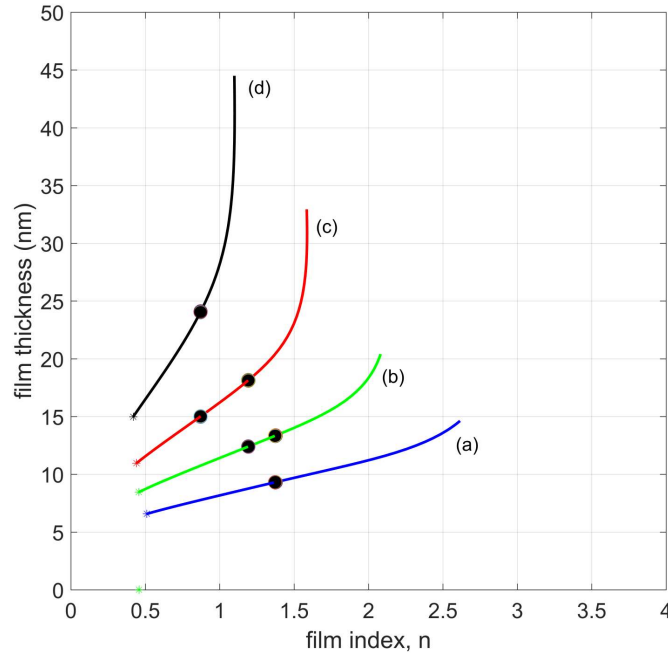


Figure 4.24: This figure shows projection of four solution curves onto the n-d plane for NiOx films deposited for (a) 10 min., (b) 15 min., (c) 20 min., and (d) 30 min. Measurements were made at 370 nm light wavelength.

Figure 4.24 shows plots of the same four solution curves but projected on the n-d plane rather than n-k plane. Recall that solution curves consists of a set of points in three-dimensional n-k-d space which are being represented in two dimensions, the most the can be shown here. There are three pairs of black dots, one vertically aligned pair for each intersection in the n-k plane. Due to the geometry, curve (b) intersects both curve (a) and curve (c). The same is true for curve (c) with (b) and (d). It can be seen that for curve (d) the intersection lies on a segment for which the thickness is changing very quickly with respect to the film index, n. This situation results in a thickness solution which is more sensitive to measurement accuracy that is the case for the other curves, especially (a) and (b). Recall that the geometry of the n-k-d space is purely a

function of the underlying mathematics and cannot be avoided. All solution methods are dealing with the same model equations. One of the advantages of the method presented here is that this behavior is visualized and can lead to selecting wavelengths for which the curves are relatively flat in the region of the intersections as is the case for curves (a) and (b) here. Experimental design becomes a factor here as well.
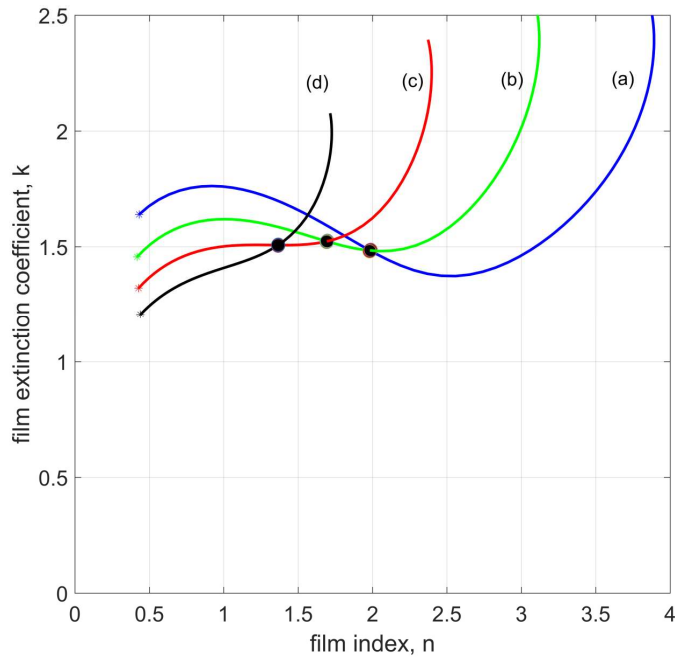


Figure 4.25: This figure shows four solution curves for NiOx films deposited for (a) 10 min., (b) 15 min., (c) 20 min., and (d) 30 min. Measurements were made at 400 nm light wavelength.

Figure 4.25 shows the solution curves for measurements made at 400 nm light wavelength. Note the intersection angles between adjacent solution curves. While these angles are not ideal, they are better than those found for the 370 nm measurements. This improved condition at the intersection persists for the wavelength range up to measurements made at 500 nm light wavelengths shown in Figure 4.26 which shows a more acute angle between adjacent curves, similar to those shown in Figure 4.23 at 370 nm light wavelength. Figure 4.27 shows curves at 600 nm light wavelength and these are clearly less useful for determining thickness. The situation deteriorates further beyond this wavelength to the end at 950 nm light wavelength.

Therefore the best wavelength range for determination of film thicknesses was chosen to be the range from 400 nm to 500 nm light wavelength.
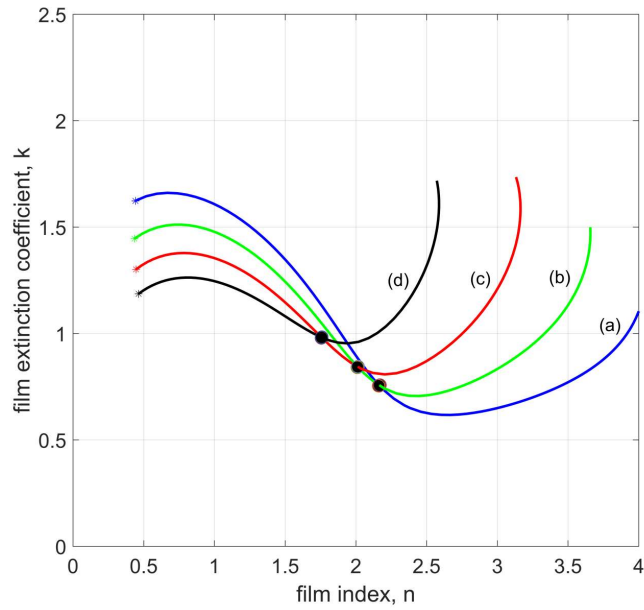


Figure 4.26: This figure shows four solution curves for NiOx films deposited for (a) 10 min., (b) 15 min., (c) 20 min., and (d) 30 min. Measurements were made at 500 nm light wavelength.
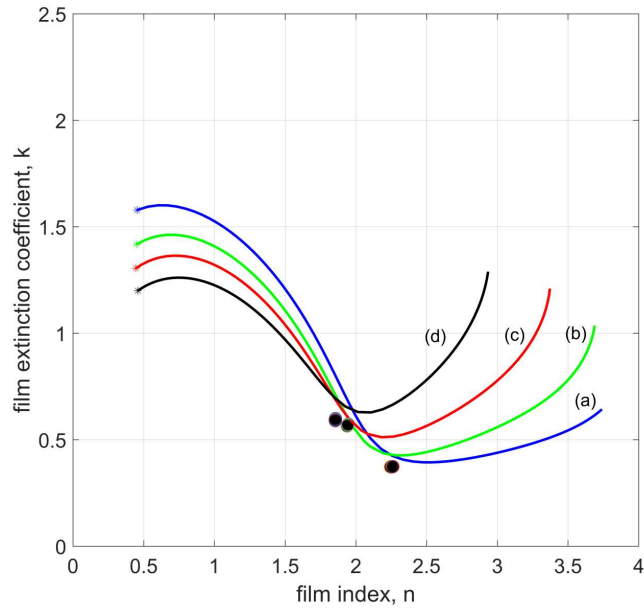

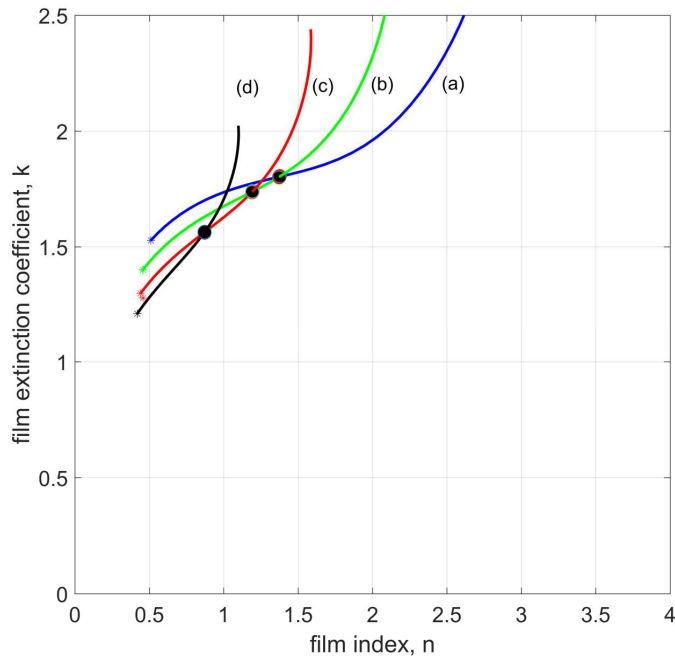
Figure 4.27: This figure shows four solution curves for NiOx films deposited for (a) 10 min., (b) 15 min., (c) 20 min., and (d) 30 min. Measurements were made at 600 nm light wavelength.

Thicknesses of all for films were taken from intersections bearing in mind that the intersections occur in the following pairs: (a)-(b), (b)-(c), and (c)-(d). Thus the thicknesses of layers (a) and (d) are taken to be those found by the single intersection they have with their adjacent layer. And the thicknesses of (b) and (c) are taken to be the average of the two intersections in which they take part. The four thicknesses are 10.3 nm, 13.7 nm, 17.5 nm and 24.5 nm respectively as exhibited in Figure 4.28 as the average of the thickness is determined for all 65 wavelengths measured from 400 to 500 nm.
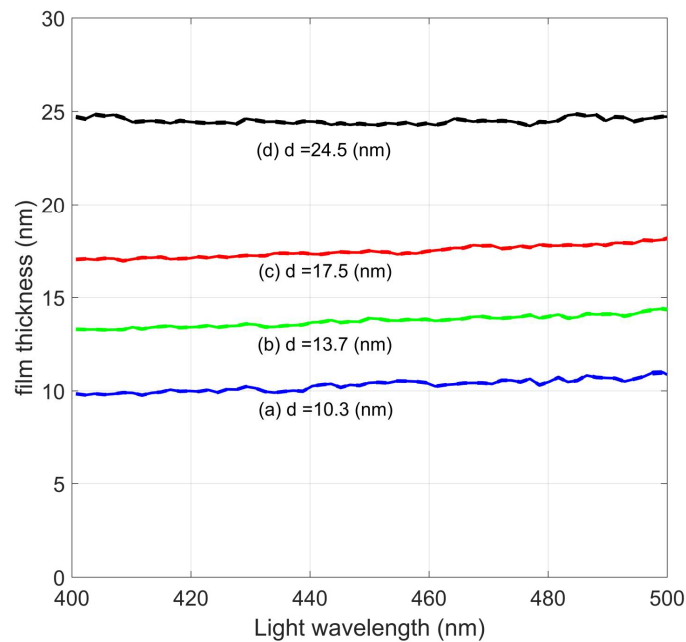


Figure 4.28: This figure exhibits 65 different solved thicknesses for NiOx films deposited for (a) 10 min., (b) 15 min., (c) 20 min., and (d) 30 min. The thicknesses in the figure are averages of 65 measurements between 400 and 500 nm.

A bit of variation can be seen in each of the plots which presumably is due to measurement accuracy considering that in the physical world each film only has one thickness and that the mathematical solution was performed to 13 figures of accuracy. Nevertheless the thicknesses remain in a very tight range considering that the step in thickness between layers (a) and (b) is merely 3.4 nm while (b) and (c) are separated by 3.8 nm and (c) and (d) by 7.0 nm. Once the thickness of each layer is determined it becomes possible to find the unique value of n

and k for each of the 368 measurements across wavelength for each of the four films (a) through (d). In this work, optical properties were determined by scanning the points on each solution curve defined the values just above and just below the thickness determined in the preceding step. Next an interpolation is performed on these numbers.

Figure 4.29 exhibits a plot of each of the 368 solutions for a total of 1,472 independently calculated values. They can be seen that at the shortest wavelength the extinction coefficient, k, is highest for the 10.3 nm film, and it decreases in thickness order to the 24.5 nm film. The films reversers sequence at about 400 nm up to around 500 nm. Beyond 500 nm the thickest film crosses below and descends to the limit of measurements. So the first observation is that the films are inhomogeneous in the growth direction. The more interesting observation is that the extinction coefficient only descends to about 0.5 rather than to a number approaching zero which is indicative of a transparent oxide film. This suggests that the film may be a mixture of metal and metal oxide, a hypothesis to be further examined following.

Figure 4.30 shows the index of refraction, n, as a function of wavelength for all for films. In this case the index for the thinnest film, 10.3 nm, is the highest of the four. The value of the index decreases monotonically with increasing film thickness across the entire wavelength range.
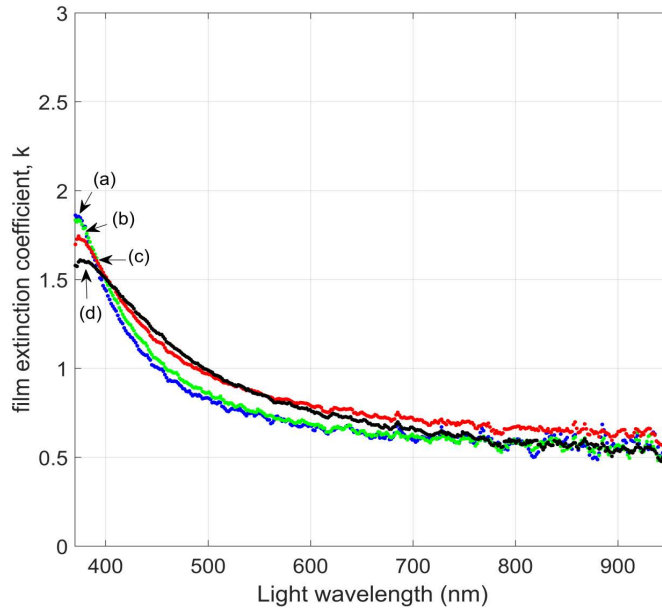
Figure 4.29: This figure shows the film extinction coefficient, k, for NiOx films deposited for (a) 10 min., (b) 15 min., (c) 20 min., and (d) 30 min. from 370 nm to 950 nm light wavelength.
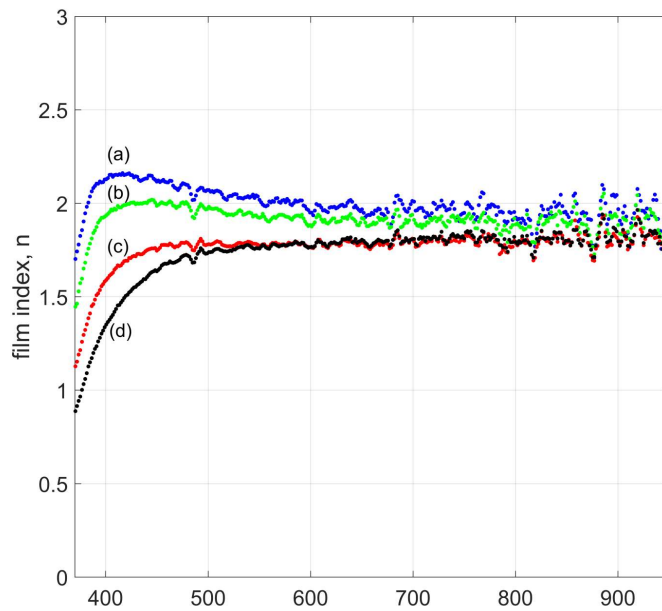


Figure 4.30: This figure shows the film index of refraction, n, for NiOx films deposited for (a) 10 min., (b) 15 min., (c) 20 min., and (d) 30 min. from 370 nm to 950 nm light wavelength.

### 4.2.1 Effect of annealing

The possibility that the films are not fully oxidized was examined by heating separate coupons of each film to 400°C in oxygen for 3 min. and 6 min. Temperature of 400°C was chosen for post annealing since oxidation kinetics is at its peak in nickel films at this temperature [102]. The plot in Figure 4.31 shows the results for the thinnest film, 10.3 nm in thickness. It exhibits a significant decrease in film extinction coefficient with annealing time. The figures show that the film is changing in the annealing step resulting in the lowering of the extinction coefficient. This suggests that longer annealing times would result in further decrease in extinction coefficient. Figure 4.32 shows the same annealing process applied to the next thicker film, 13.7 nm. This figure shows the same trend as for the thinnest film in Figure 4.31. The values of the real part of the index of refraction, n, also shifted with annealing but much less (

Figure 4.33-Figure 4.34).
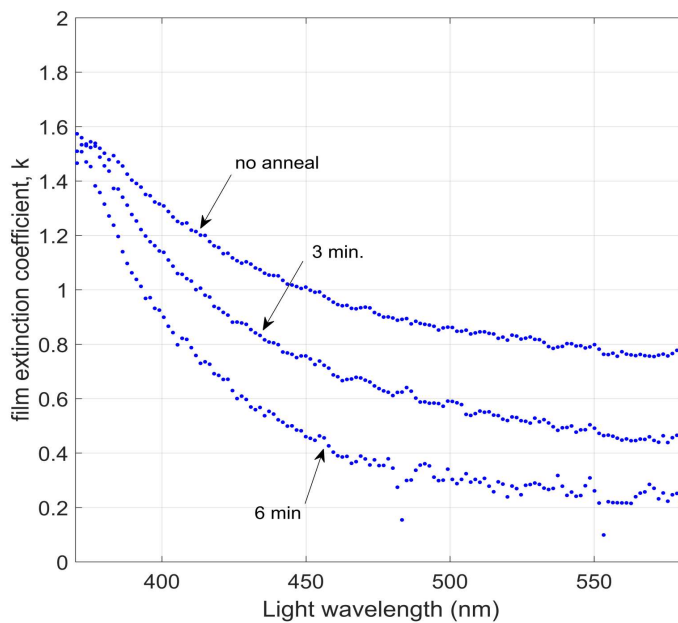


Figure 4.31: This figure shows the film extinction coefficient, k, for NiOx films deposited for 10 min, as deposited, following 3 min. annealing at 400° C under oxygen and following 6 min. annealing at 400° C under oxygen.
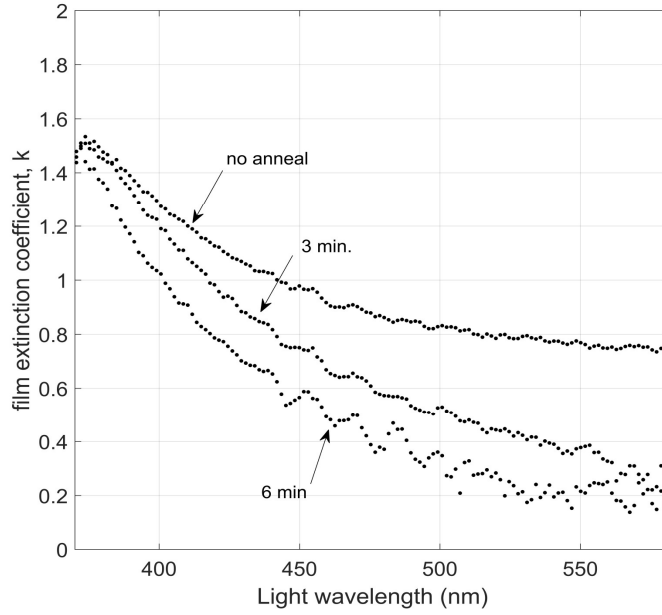
Figure 4.32: This figure shows the film extinction coefficient, k, for NiOx films deposited for 15min, as deposited, following 3 min. annealing at 400° C under oxygen and following 6 min. annealing at 400° C under oxygen.
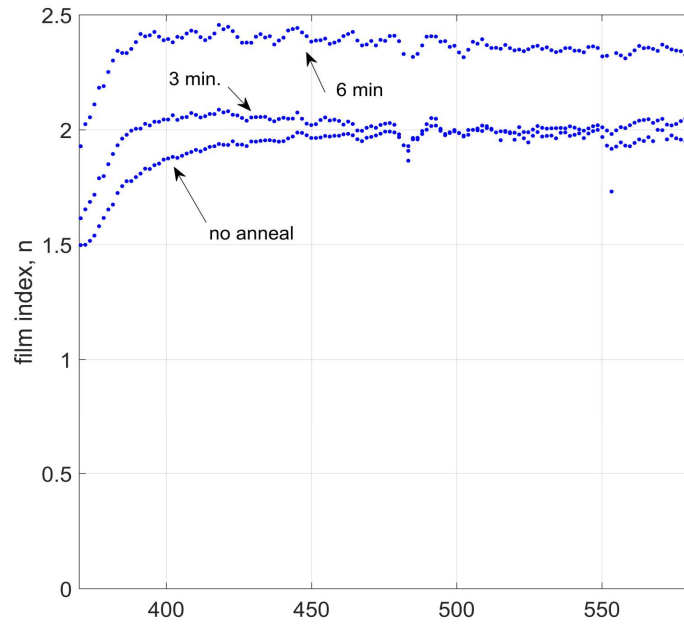


Figure 4.33: This figure shows the index of refraction, n, for NiOx films deposited for 10 min, as deposited, following 3 min. annealing at 400° C under oxygen and following 6 min. annealing at 400° C under oxygen.
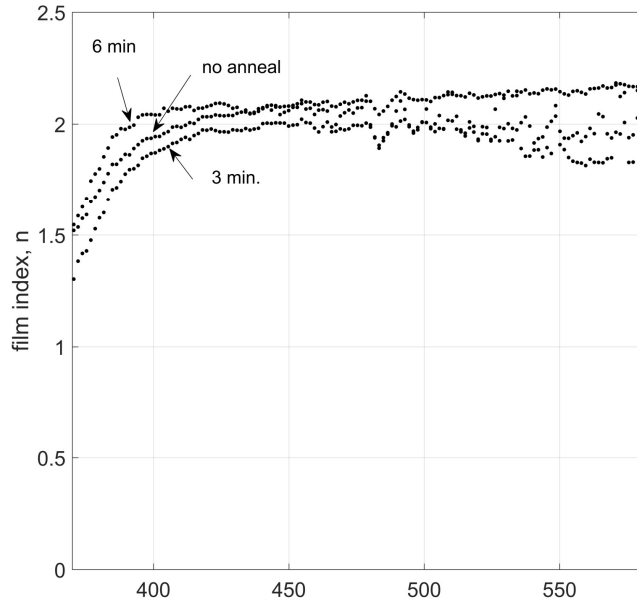
Figure 4.34: This figure shows the index of refraction, n, for NiOx films deposited for 15 min, as deposited, following 3 min. annealing at 400° C under oxygen and following 6 min. annealing at 400° C under oxygen.

### 4.2.2    Conclusions

Ellipsometry measurements for different thicknesses of reactive magnetron sputter deposited NiOx revealed inhomogeneity in the growth direction for the films. It also revealed a rather high, k = 0.5, extinction coefficient suggesting the material may be a mixture of nickel and nickel oxide. As a first step to explore this possibility the films were annealed type 400° C for 3 min. and 6 min. which resulted in a significant reduction in extinction coefficient. This suggests that the films were more fully oxidized in the annealing step but this has yet to be confirmed by compositional analysis.  This suggests further investigation of these films to examine the oxygen depth profile and NiO composition.

## 4.3 Annealed-film device characteristics

### 4.3.1    Material characterization

An important factor that dramatically influences the tunneling current in MIM diodes is the roughness of the film. The surface roughness of a 6nm thick un-annealed and annealed NiOx films on Si substrate, over an area of 10μmX10μm, is shown in Figure 4.35. The average roughness of un-annealed film, 3 min. annealed, and 6 min. annealed film is 0.127nm, 0.155nm, and 0.204nm. The average roughness is less than 1nm which is in agreement with the characterized roughness of NiOx films at low power (<100W) high temperature (>350 °C) [103].



(a)                                    (b)



(c)
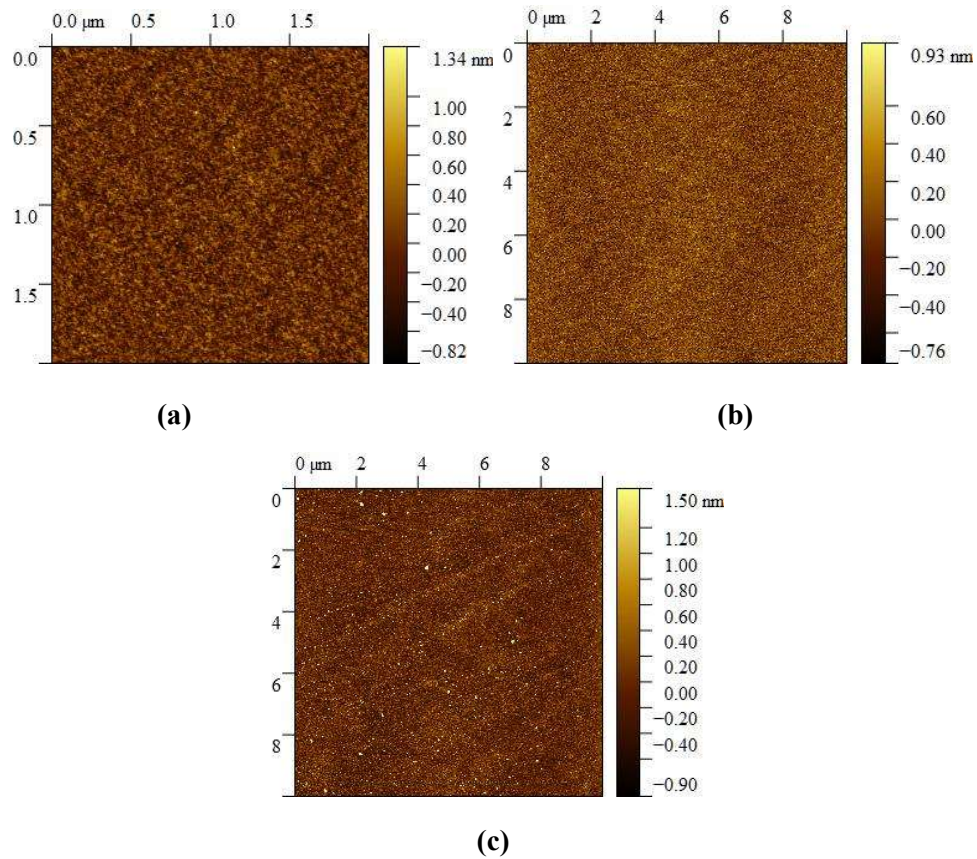
Figure 4.35: Surface roughness of (a) un-annealed, (b) 3 min. annealed and (c) 6 min. annealed NiOx films on silicon substrate.

From Raman spectroscopy, NiO peaks near 1000 cm$^{-1}$ are evident as shown in Figure 4.36. The peak intensity increases with annealing time.  This can be due to microstructural

changes in the NiO$_x$ layer, suggesting a more crystalline structure. The effect of film composition on the decrease in extinction coefficient with annealing was examined using Secondary Ion Mass Spectroscopy (SIMS) for NiOx films with nominal 10nm and 15nm thicknesses. From, Figure 4.37 and Figure 4.38 it can be concluded that the Ni:O ratio in the films didn't change with annealing since the NiO and O$_2$ peaks overlap for 0min, 3min, 6min, and 12min anneal time. However, the nickel peaks are higher than the NiO and O$_2$ peaks. This does not signify anything other than Ni has a higher secondary ion yield in this matrix. We also observe a peak in all the elements at the interface, which is a sputter beam artefact. Since a final thickness of 3nm NiO was desired for the MIM diode, SIMS measurements were also used to analyze 3nm thick NiO films on Si substrate (Figure 4.39) and 100nm Nickel substrate (Figure 4.40) with 0min and 3min anneal time. On Si substrate, NiO and O$_2$ peaks do not overlap and O$_2$ peaks are much higher (Figure 4.39). Since the film is very thin, it is hard to conclude anything about the Ni:O ratio from this other than that there may be loose O$_2$ bonds on the surface of the film. An overlap between NiO and O$_2$ peak is evident in case of the NiO film on Ni substrate (Figure 4.40). The NiO erosion time is noticeably longer in case of the 3min annealed film as compared to the 0min film especially on Ni substrate. This suggests a strong NiO bond, possibly a more crystalline NiO film. To conclude the SIMS depth profiles did not show a measurable change in relative abundance of oxygen for pre and post annealing at all anneal times. Thus it can be stated that changes in the optical properties of the films most likely came about due to the thermal treatment and not by significant incorporation of additional oxygen. At this time, the leading hypothesis for this effect is that the thermal annealing provided sufficient energy to minutely move and affect the bond states of the Ni and O atoms which had been frozen in place in a somewhat random structure during the room temperature deposit. Thus the ratio of film atoms was approximately correct but they were in the "wrong" place, much as is seen in post ion implant annealing.
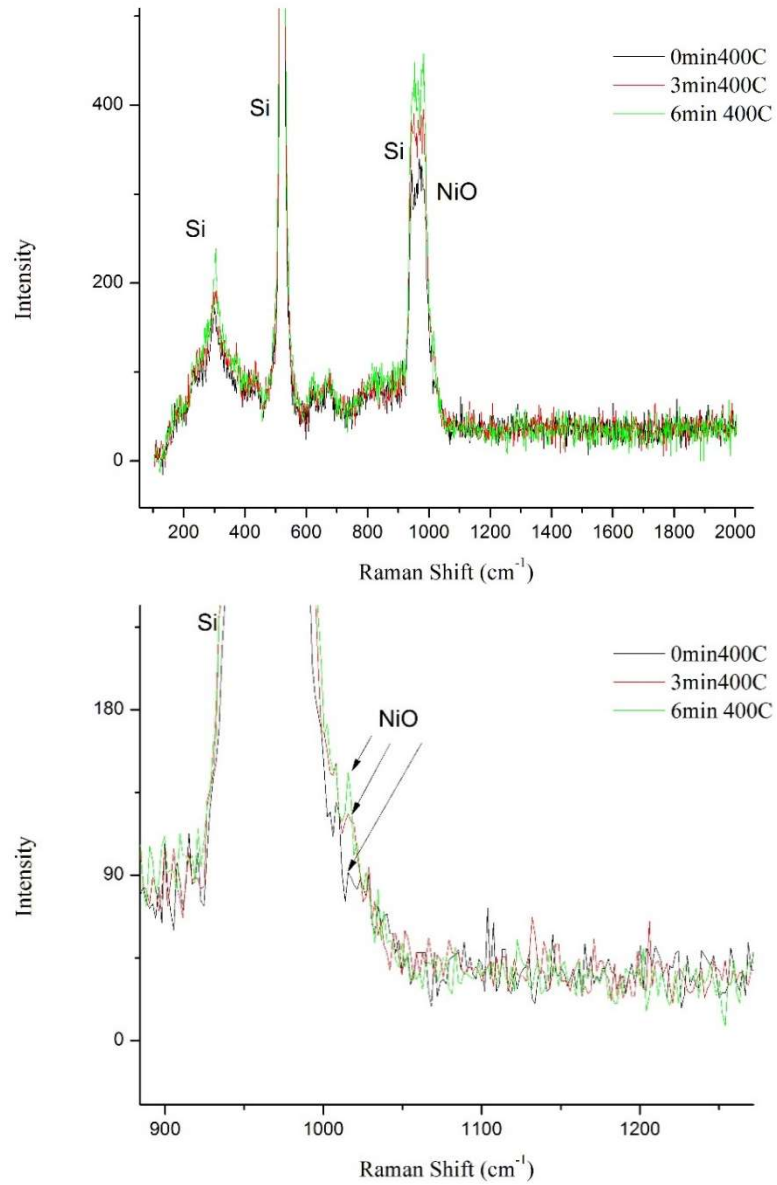
Figure 4.36: Raman spectroscopy of un-annealed and annealed NiO$_x$ films on bare silicon substrate.
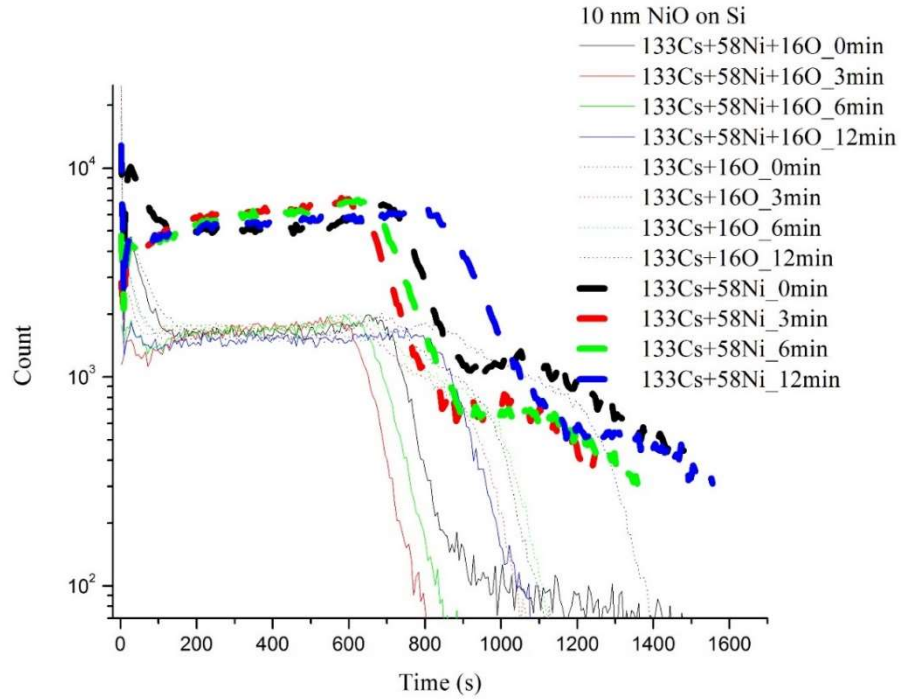
Figure 4.37: SIMS oxygen depth profile for un-annealed and annealed10nm NiO$_x$ film on silicon.
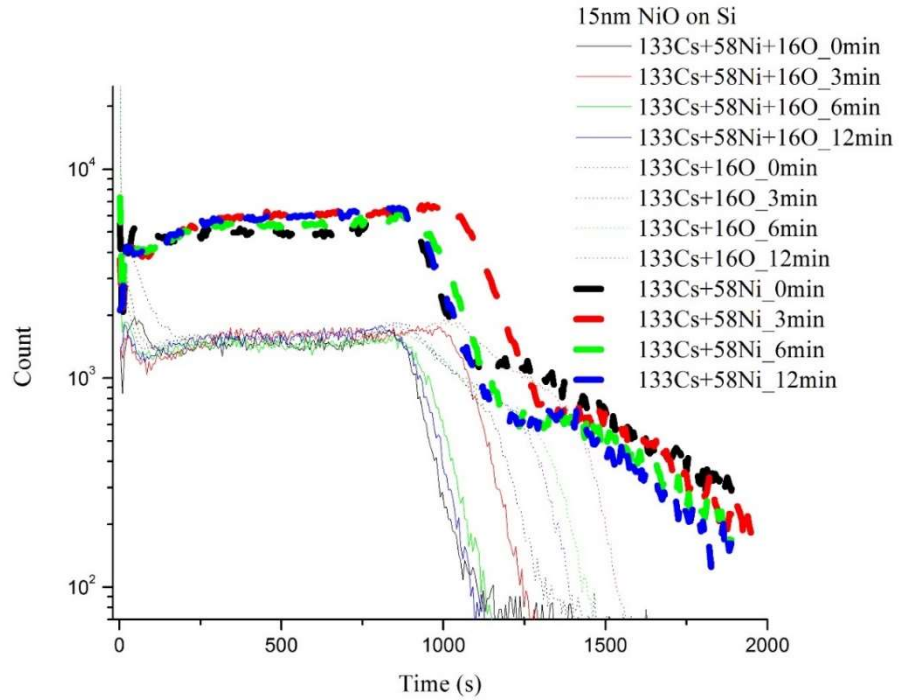


Figure 4.38: SIMS oxygen depth profile un-annealed and annealed 15nm NiO$_x$ film on silicon.
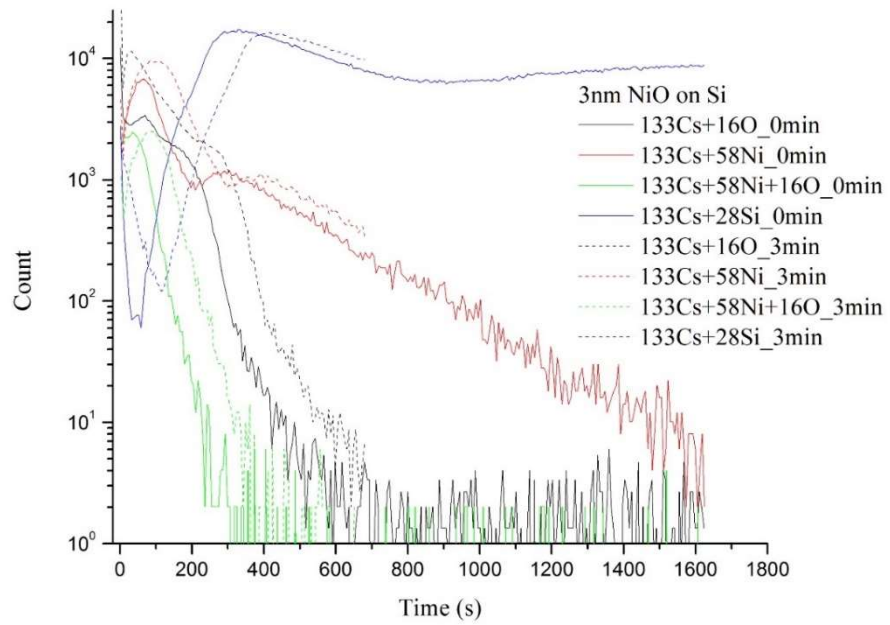
Figure 4.39: SIMS oxygen depth profile for un-annealed and annealed 3nm NiO$_x$ film on silicon
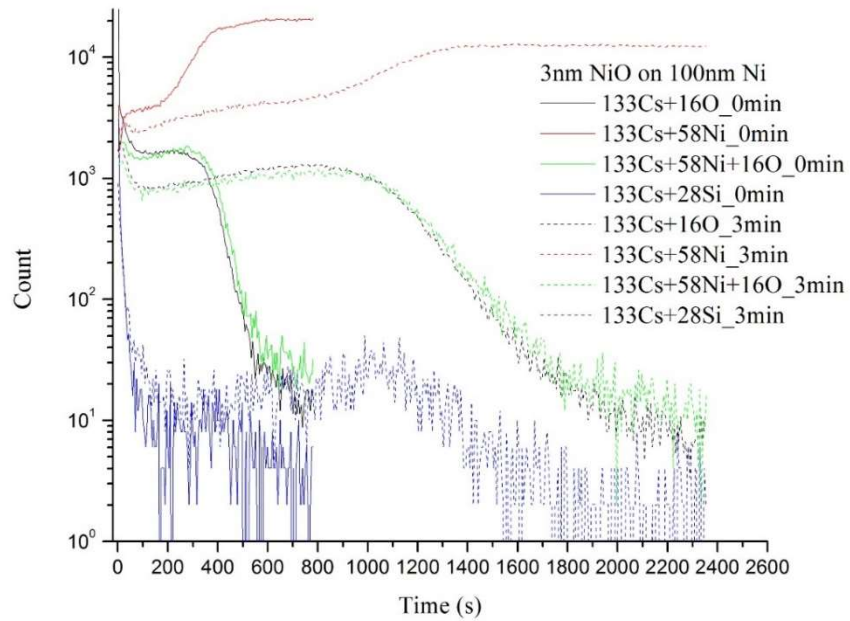


Figure 4.40: SIMS oxygen depth profile for un-annealed and annealed 3nm NiO$_x$ film on 100 Ni film

### 4.3.2 I-V and C-V characteristics

I-V characteristics of the Ni-NiOx-Cr junction with un-annealed and post deposition annealed NiOx film is shown in Figure 4.41. The magnitude of the current is the greatest for the un-annealed film and decreases with increasing annealing time. This decrease in current corresponds to a lower current capability of the diode which is undesirable. A beneficial trend is observed by capacitance-voltage measurements also where the capacitance decreases with annealing time. The maximum capacitance ($C_{max}$) drops from 3.2pF to 2.55pF and 1.85 pF after a 3 min and 6 min. anneal (Figure 4.42). The capacitance, $C=(\epsilon_r\epsilon_0 A)/d$ where $\epsilon$ is the dielectric constant, A is the area of the junction, and d is the initial thickness. Since A is controlled, the decrease in C with annealing can be accounted for either by decrease in the dielectric constant or an increase in thickness or a combination. An increase in thickness can be neglected since ellipsometry confirms little to no change in thickness. Therefore, it is primarily due to a decrease in dielectric constant at the measurement frequency which is consistent with the optical findings above. Another important factor that dramatically influences the tunneling current is the roughness of the film. Increasing roughness not only contributes to an uneven thickness in the junction but also decreases the effective junction area, which leads to a drop in the magnitude of the current.

From the I-V curve the sensitivity of the MIM junction was also extracted. Sensitivity defines the nonlinearity of the MIM diode. Sensitivity is the ratio of second derivative (I") to first derivative (I') of I-V curve. The second derivative ($I"=d^2I/dV^2$) implies the rate of change of conductivity. The sensitivities of the devices with un-annealed film and annealed films is shown in Figure 4.43. The maximum sensitivity of the device with un-annealed film is 31 $V^{-1}$ at 0.23V over an area of 20 μm X 20 μm. The values obtained for devices with 3 minute and 6 minute annealed films are 49$V^{-1}$ at 0.19V and 36 $V^{-1}$ at 0.24V respectively. Thus, a short anneal time of 3 minutes enhances the sensitivity of the device while there is little difference with 6 minute

annealed films In a similar work where the films were annealed in presence of oxygen, MIM junctions exhibited increase in current with increase in annealing temperature [104]. This increase in current was explained by the increase in grain growth of oxide film. Krishnan et. al. took a different approach of annealing the complete device junction instead of just the oxide on bottom electrode [105]. They also reported an initial increase in current with annealing, however on further annealing the device current values drop as the temperature is increased. The initial increase in current was explained by polycrystalline nature of NiO and the drop in current was due to a fully crystallized film.
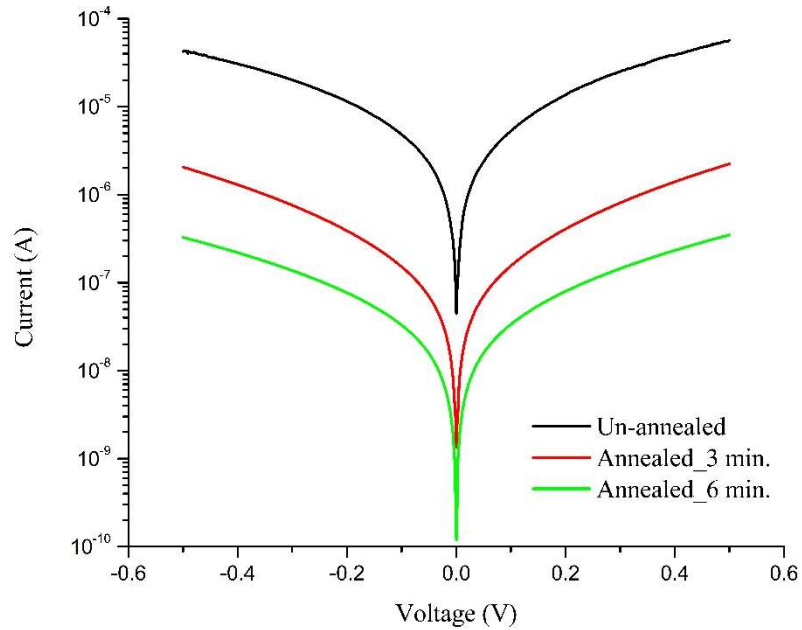


Figure 4.41: I-V characteristics of the MIM junction with un-annealed and annealed oxide at 400°C
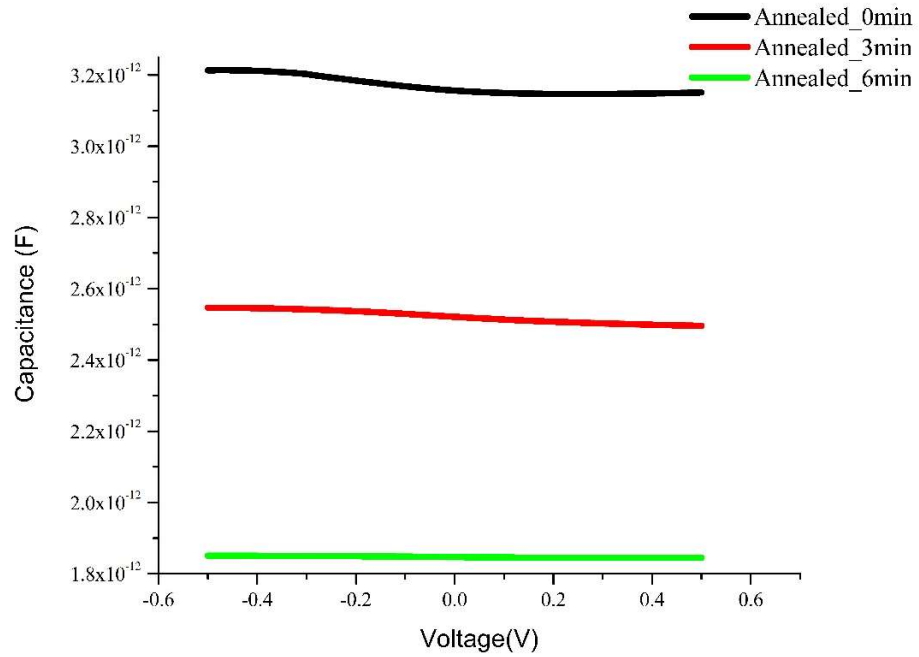
Figure 4.42: C-V characteristics of the MIM junction with un-annealed and annealed oxide at 400°C
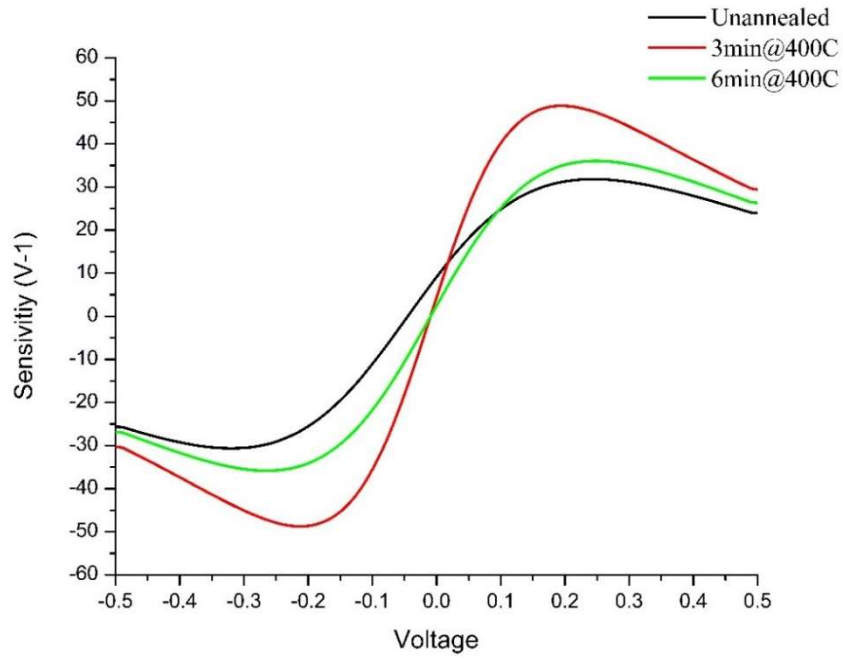


Figure 4.43: Sensitivity of Ni-NiOx-Cr junction with un-annealed and annealed oxide at 400 °C

### 4.3.3    Conclusions

In summary ellipsometry measurements on four different thicknesses of reactive magnetron sputter deposited NiOx revealed inhomogeneity in the growth direction for the films. Measurements also revealed a rather high, $k = 0.8$, extinction coefficient suggesting the material may be a mixture of nickel and nickel oxide. The films were annealed at $400° C$ for 3 min. and 6 min. which resulted in a significant reduction in the extinction coefficient. This occurred with no significant change of the Ni to O ratio.  This suggests that the films reorganized by annealing to achieve an improved stoichiometric configuration on an atomic scale.  The I-V characteristics of the devices with annealed films did not show a significant increase in the non-linearity or sensitivity but did exhibit a significant decrease in current capability. The C-V characteristics showed a decrease in capacitance with short annealing time which is consistent with the change in optical properties. The ellipsometry results demonstrate that direct measurements on inhomogeneous films may be carried out using ellipsometry for layer thicknesses in the 10 to 30 nm range with a layer resolution of less than 4 nm.  These results also suggest than additional measurements at intermediate thicknesses could result in optical property resolution on the single nanometer scale, which is near or at a single monolayer.

### 4.4  Optical response

In spite of the ongoing research in THz field, frequency selective THz devices are still a challenge due to the poor spectral response in THz range and electromagnetic field enhancement [106].  Rectenna, rectifying-antenna, is one such device which has been explored for THz applications. In an effort to demonstrate that MIM diode based rectennas can be employed for THz detections geometric MIM diodes [107] and rectennas [59] have been explored. The graphene based geometric diode proved to have a very low RC time constant of 7 femtosecond, however it's responsivity was $<1V^{-1}$ [107].  Since rectenna based model demonstrates higher responsivities [59], efforts to optimize the rectenna parameters are still ongoing. The final aim of

this research was development of an antenna design that incorporates the diode component into its design allowing it to exploit MIM rectenna benefits effectively. Specifically, this project aims discovering the correct geometry at optimizing the design of a bowtie antenna to operate at optical frequencies. Lumerical software was utilized for the three-dimentional (3D) finite-difference time-domain (FDTD) method based numerical modelling for the THz frequency range. Numerical modelling based simulation is presented for a complete rectenna structure i.e. antenna and diode rather than just the antenna. Simulations have been carried out to optimize the bowtie antenna parameters where the bowtie arms overlap sandwiching a thin oxide to form the complete rectenna structure. The antenna was made asymmetric by using two different metals for the antenna arms. The metals used for this work are nickel (Ni) and gold (Au) as the bottom and top metal layers of the MIM rectenna. Aluminum oxide has been used as the oxide layer in the structure. Substrate medium was defined by semi-infinite layer of silicon dioxide. This forms the four layer stack structure as shown in Figure 4.44, where the first layer is the substrate, nickel is the second, oxide is the third, and gold is the fourth. The thickness of each metal layer is 400nm. The simulation was done for 10nm and 20nm oxide thickness. Each structure is referred to as 10nm dimer and 20nm dimer.

The Lumerical package version 8.15 was utilized for the 3D FDTD method based numerical modelling. The 3D grid sizes for the MIM device layers were set to 1 nm in all directions. The material properties experimentally derived by E. D. Palik [108] were used for modelling. Boundaries were defined by perfectly matched layers. A linear electrical plane wave was used as the light source with pulse length and offset time length of 2.65 fs and 7.5 fs.
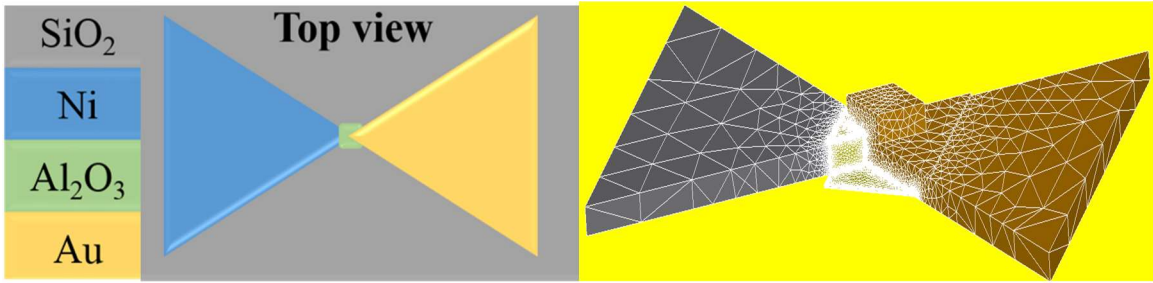
Figure 4.44: Top-view and the cross-sectional view of the bow-tie structure used for numerical modelling

The simulated structure is excited through a normally incident plane wave (z-axis) with an electric field intensity of 1 V/m and a linear polarization parallel to the rectenna axis (x-axis). Drude model has been intentionally avoided because it overlooks inter-band transition or absorption, which is very significant in metals at THz frequencies. The electric field (e-field) intensity is computed along the overlap of the metals with the oxide layer in-between forming the MIM rectenna. The antenna bow's length and angle were optimized as 150 μm and 60° with maximum absorption peak at 0.45 THz within a frequency sweep of 0.1-3 THz. To study the effect of the oxide thickness on the value of the relative intensity enhancement, two oxide thicknesses 20nm and 10nm were investigated within the frequency sweep of 0.1-3 THz, as shown in Figure 4.45 and Figure 4.46. The overlap was maintained at 20μm from tip-to-tip of the antenna arms. The 20nm and 10nm dimer result with maximum absorption at 0.32 THz and 0.4 THz (Figure 4.45 and Figure 4.46). The absorption peak shifts downward in frequency by 0.5 THz with 10nm oxide and by 0.58 THz with 20nm thick oxide. The asymmetry due to the two different metals (Ni and Au) antenna arms in the e-field intensity is more prominent in the case of 20nm dimer (Figure 4.45 and Figure 4.46). Simulations results shows that doubling the oxide thickness results in a significant decrease in the resonance frequency but a very slight variation in the e-field intensity. Since the overlap area remains the same, the e-field variation is only due to the oxide thickness. In a bowtie antenna the maximum value of the field is localized at the tip of

the bowtie. In the overlap design of a MIM rectenna, field gets highly localized at the tip of the bowties and the only path for the signal is through the MIM rectifier. The next step was to test the simulated results. A Ni-NiO$_x$-Cr rectenna with 10nm NiO$_x$ layer was fabricated using the steps described in chapter 3 Figure 4.47. The metal thickness and dimer sizes were maintained same as in simulation. The simulated and measured response of Ni-NiO$_x$-Cr BowTie rectenna at optical frequencies matched (Figure 4.48).
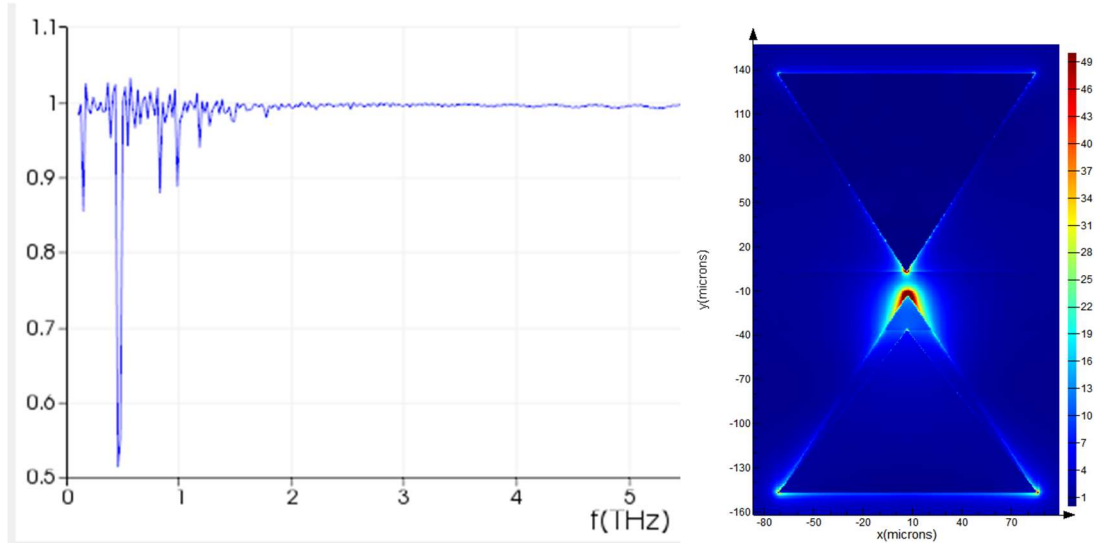


Figure 4.45: Transmission and top-view e-field of 20nm dimer structure
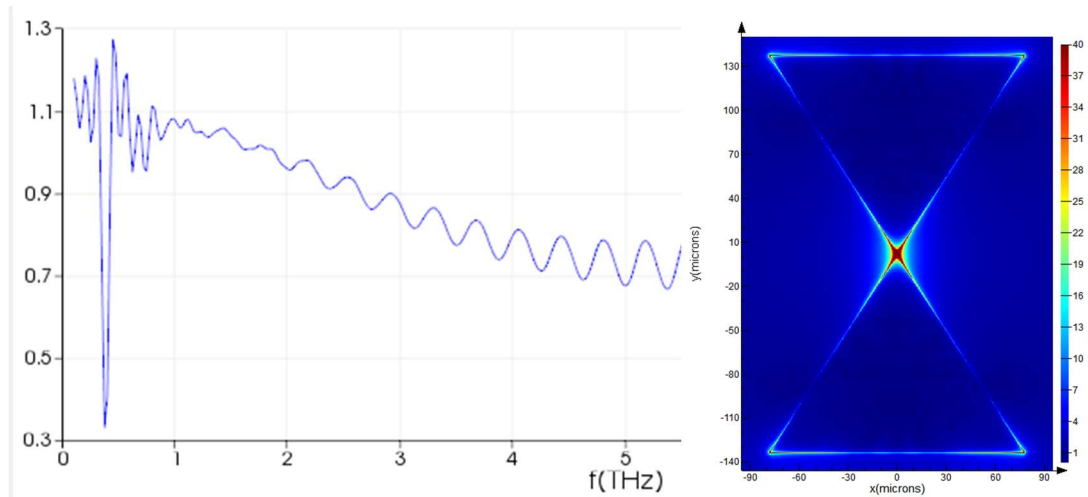


Figure 4.46: Transmission and top-view e-field of 10nm dimer structure

90
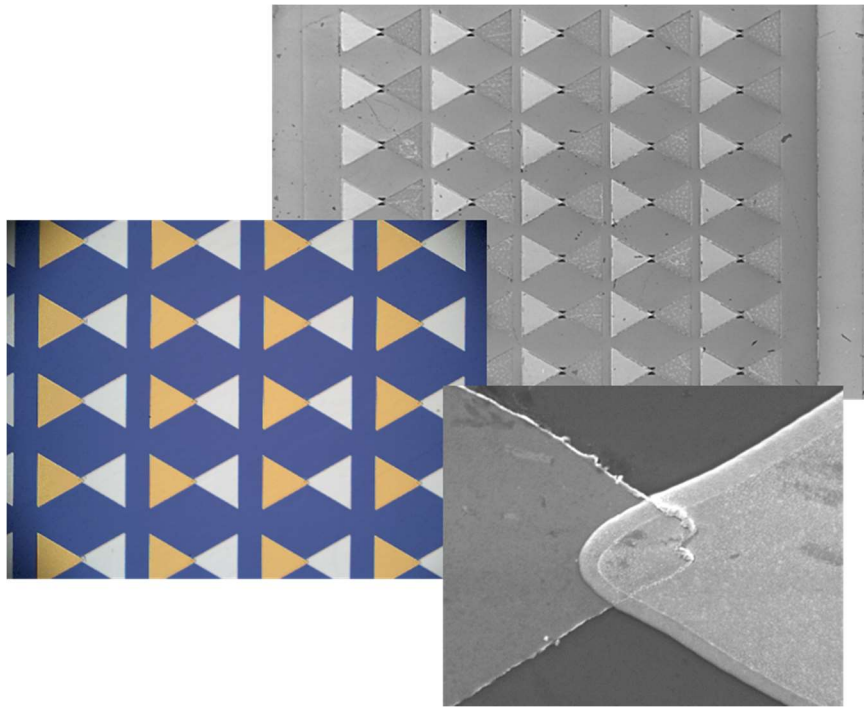
Figure 4.47: SEM and optical images of the Ni-NiO$_x$-Cr BowTie rectenna
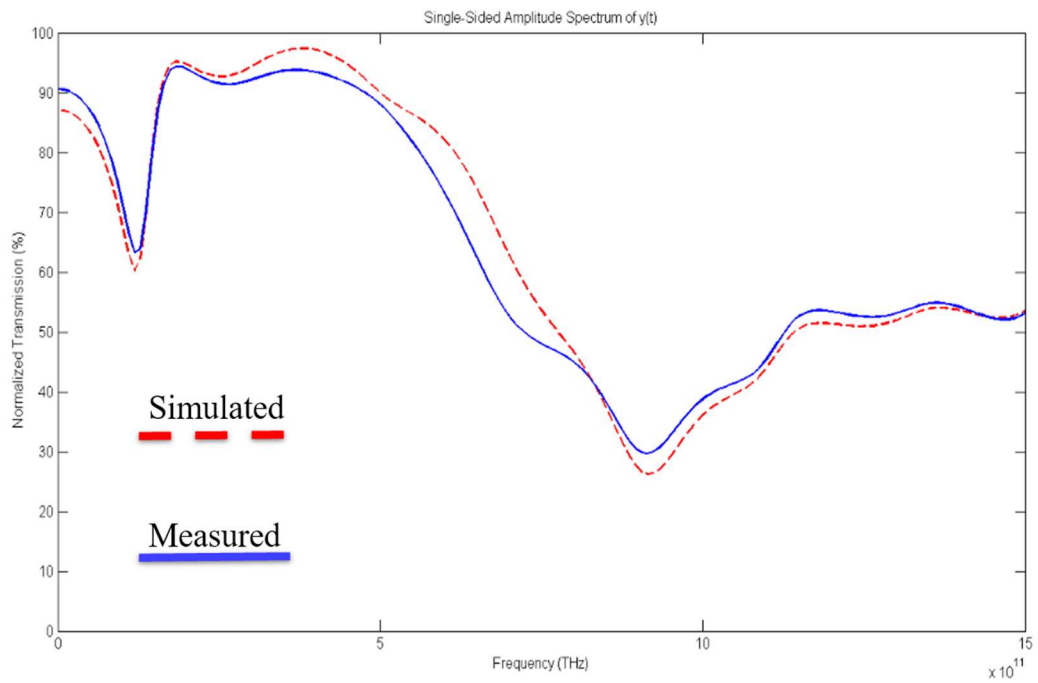


Figure 4.48: Response of Ni-NiO$_x$-Cr BowTie rectenna at optical frequencies

# 5. SUMMARY AND FUTURE WORK

In summary we report design and fabrication of bilayer Ni-NiOx-ZnO-Cr MIIM diode and compared its performance to the single layer Ni-NiOx-Cr MIM diode. I-V characterization of the devices demonstrated its capability as a rectifier in-terms of non-linearity and asymmetry which modulated the sensitivity of the devices. Theoretical modelling of the device's I-V characteristics were done to extract the device parameters. Combination of p-type ($NiO_x$) and n-type (ZnO) thin films in a MIIM configuration enhances current-asymmetry. Diodes with varying thickness were also tested. A reduced p-n junction reduces the overall diode resistance. Ellipsometry measurements on different thicknesses of sputter deposited NiOx films revealed inhomogeneity in the growth direction for the films. It also revealed a rather high, k = 0.8, extinction coefficient suggesting the material may be a mixture of nickel and nickel oxide. In order to fully oxidize the films, an annealing step was performed post-deposition and prior to final lithography step. A decrease in the k value with oxidation time suggested that the film is getting fully oxidized. I-V characteristics and C-V characteristics were performed to understand the impact of annealing on the device behavior.

A comparative study of the MIIM devices with sputtered ZnO and ALD ZnO was also done. ALD was built from first principles and characterized. Initial ALD film devices were comparable to sputtered film devices. Device fabrication steps were different and posed different challenges. The MIIM devices also responded well when high frequency signals up to 10-50GHz were fed to it proving that it can operate in a wide spectrum of frequencies giving reasonable output. The rectified current measured from the 6nm MIIM devices, at high frequencies, was less than its DC current with the highest efficiency of <1%. This performance can be improved by fine tuning the thickness and stoichiometry of the thin insulators. Addition of a matching network would greatly enhance the efficiency of the devices.

In case of the sputtered devices, it was determined that the diode design with the spacer layer exhibited more reliability. However, a spacer layer is not preferred for optical measurements since it will greatly decrease the transmittance. Therefore, devices without spacer layers were used for electrical and optical measurements. The experimental optical response of the asymmetric MIM rectenna matched the simulated results at optical frequencies. To quantify the rectification capabilities of the MIM and MIIM devices, measurements with varying input power and lower DC biases are required.

### FUTURE WORK

This research on p-n junction based MIM diodes for high frequency applications in the millimeter wave and THz range is preliminary but promising. With regard to the current structure, the following comments or suggestions can be made:

i. The asymmetry was compromised on reduction of the NiOx/ZnO junction thickness and the diode resistance was dramatically reduced. This suggests exploration of NiOx/ZnO structures with n:1 $NiO_x$:ZnO thickness ratios where p-type $NiO_x$ has higher thickness than n-type ZnO.

ii. There is limited contribution in literature on asymmetric MIM rectennas for THz detection. Asymmetric Ni-NiO-Cr MIM rectenna has shown high transmission at 0.3-0.4 THz which is promising for use of asymmetric MIM rectennas for THz detection.

iii. Further analysis of the device performance is required with varying optical and electrical properties of thin insulating films.

iv. The diodes were fabricated as a step-by-step process, wherein a photolithography process was involved after each layer. This caused the thin films to be exposed to several chemicals, causing unreliable device performance. Hence a multi-step deposition process

followed by etch can be adopted to preserve the metal-insulator and insulator-insulator interfaces.

v.   The diode development can be done by considering composite materials with alternate structural, electrical, and optical properties. The conventional transparent oxide semiconductors have large grain boundaries which effect the device performance, in terms of stability and repeatability, over large areas. In that view, it would be interesting to work with ternary metal oxides such as InZnO (IZO) [109] or quaternary metal oxide, IGZO [109, 110], apart from binary oxides such as NiO and ZnO.

REFERENCES

1.   Singh, B.R., Application of Metal-Insulator-Metal (MIM) capacitors as a d.c. block in microwave integrated circuits. Thin Solid Films, 1977. **42**(3): p. L5-L8.

2.   Mondal, J.P., An Experimental Verification of a Simple Distributed Model of MIM Capacitors for MMIC Applications. IEEE Transactions on Microwave Theory and Techniques, 1987. **35**(4): p. 403-408.

3.   Slayman, C.W. and T.K. Gustafson. Metal-Barrier-Metal Junctions for Room Temperature Millimeter-Wave Mixing and Detection. in Microwave Symposium Digest, 1981 IEEE MTT-S International. 1981.

4.   Dees, J.W., Detection and harmonic generation in the submillimeter wavelength region Microwave Journal 1966. **9**: p. 48-55.

5.   Jennings, D.A., F.R. Petersen, and K.M. Evenson, Extension of absolute frequency measurements to 148 THz: Frequencies of the 2.0- and 3.5-μm Xe laser. Applied Physics Letters, 1975. **26**(9): p. 510-511.

6.   Moichiro, N., Response Time of Metal-Insulator-Metal Tunnel Junctions. Japanese Journal of Applied Physics, 1972. **11**(11): p. 1611.

7.   Rogalski, A., Infrared detectors: status and trends. Progress in Quantum Electronics, 2003. **27**(2–3): p. 59-210.

8.   Jayaweera, P.V.V., et al., Uncooled infrared detectors for 3–5μm and beyond. Applied Physics Letters, 2008. **93**(2): p. 021105.

9.   Hübers, H.W., G.W. Schwaab, and H.P. Röser, Video detection and mixing performance of GaAs Schottky-barrier diodes at 30 THz and comparison with metal-insulator-metal diodes. Journal of Applied Physics, 1994. **75**(8): p. 4243-4248.

10.  Kazemi, H., et al. First THz and IR characterization of nanometer-scaled antenna-coupled InGaAs/InP Schottky-diode detectors for room temperature infrared imaging. 2007.

11.  Masalmeh, S.K., H.K.E. Stadermann, and J. Korving, Proceedings of the Second International Conference on Point-contact SpectroscopyMixing and rectification properties of MIM diodes. Physica B: Condensed Matter, 1996. **218**(1): p. 56-59.

12.  Frayne, P.G., N. Chandler, and M.W. Booton, Point-contact diode submillimetre detectors. Journal of Physics D: Applied Physics, 1978. **11**(17): p. 2391.

13.  Wiesendanger, E. and F. Kneubühl, Thin-film MOM-diodes for infrared detection. Applied physics, 1977. **13**(4): p. 343-349.

14.  Matyi, G., Nanoantennas for uncooled, double-band, CMOS compatible, high-speed infrared sensors. International Journal of Circuit Theory and Applications, 2004. **32**(5): p. 425-430.

15. Krishnan, S., Thin film metal-insulator-metal tunnel junctions for millimeter wave detection, in Electrical Engineering. 2008, University of South Florida.

16. Grover, S. and G. Moddel, Metal Single-Insulator and Multi-Insulator Diodes for Rectenna Solar Cells, in Rectenna Solar Cells, G. Moddel and S. Grover, Editors. 2013, Springer New York: New York, NY. p. 89-109.

17. Eliasson, B.J., Metal-Insulator-Metal Diodes for Solar Energy Conversion, in Electrical and Computer Engineering Department. 2001, University of Colorado: Boulder.

18. Grover, S. and G. Moddel, Applicability of Metal/Insulator/Metal (MIM) Diodes to Solar Rectennas. IEEE Journal of Photovoltaics, 2011. **1**(1): p. 78-83.

19. Grover, S. and G. Moddel, Engineering the current–voltage characteristics of metal–insulator–metal diodes using double-insulator tunnel barriers. Solid-State Electronics, 2012. **67**(1): p. 94-99.

20. Hoofring, A.B., V.J. Kapoor, and W. Krawczonek, Submicron nickel-oxide-gold tunnel diode detectors for rectennas. Journal of Applied Physics, 1989. **66**(1): p. 430-437.

21. Heiblum, M., et al., Characteristics of integrated MOM junctions at DC and at optical frequencies. IEEE Journal of Quantum Electronics, 1978. **14**(3): p. 159-169.

22. Wilke, I., et al., Nanometer thin-film Ni-NiO-Ni diodes for 30 THz radiation. Applied Physics A, 1994. **58**(4): p. 329-341.

23. Abdel-Rahman, M.R. and González, Antenna-coupled metal-oxide-metal diodes for dual-band detection at 92.5 GHz and 28 THz. Electronics letters, 2004. **40**(2): p. 1.

24. Esfandiari, P., et al. Tunable antenna-coupled metal-oxide-metal (MOM) uncooled IR detector (Invited Paper). 2005.

25. Krishnan, S., et al., Design and development of batch fabricatable metal–insulator–metal diode and microstrip slot antenna as rectenna elements. Sensors and Actuators A: Physical, 2008. **142**(1): p. 40-47.

26. Choi, K., et al., A Focused Asymmetric Metal-Insulator-Metal Tunneling Diode: Fabrication, DC Characteristics and RF Rectification Analysis. IEEE Transactions on Electron Devices, 2011. **58**(10): p. 3519-3528.

27. Alimardani, N., et al., Investigation of the impact of insulator material on the performance of dissimilar electrode metal-insulator-metal diodes. Journal of Applied Physics, 2014. **116**(2): p. 024508.

28. Ajayi, O.A., DC and RF Characterization of High Frequency ALD Enhanced Nanostructured Metal-Insulator-Metal Diodes. 2014.

29. Donchev, E., Thin-Film Diode Structures for Advanced Energy Applications. 2015, Imperial College London.

30. Maraghechi, P., et al., Enhanced rectifying response from metal-insulator-insulator-metal junctions. Applied Physics Letters, 2011. **99**(25): p. 253503.

31. Aydinoglu, F., et al., Higher Performance Metal-Insulator-Metal Diodes using Multiple Insulator Layers. Austin J Nanomed Nanotechnol, 2013. **1**.

32. Alhazmi, M., et al., Comparison of the effects of varying of metal electrode in metal-insulator-metal diodes with multi layer dielectric layers. Austin J Nanomed Nanotechnol, 2014. **2**.

33. Rockwell, S., et al. Characterization and Modeling of Metal/Double-Insulator/Metal Diodes for Millimeter Wave Wireless Receiver Applications. in 2007 IEEE Radio Frequency Integrated Circuits (RFIC) Symposium. 2007.

34. A new technology for terahertz electronics, Phiar Corporation, 2003.

35. Hegyi, B., Á. Csurgay, and W. Porod, Investigation of the nonlinearity properties of the DC I-V characteristics of metal-insulator-metal (MIM) tunnel diodes with double-layer insulators. Journal of Computational Electronics, 2007. **6**(1): p. 159-162.

36. Esaki, L., Long journey into tunneling. Reviews of Modern Physics, 1974. **46**(2): p. 237-244.

37. Alimardani, N., Investigation of metal-insulator-metal (MIM) and nanolaminatebarrier MIIM tunnel devices fabricated via atomic layer deposition, in Electrical and Computer Engineering. 2013, Oregon State University. p. 182.

38. Choi, K.N., et al., Fabrication and Electrical Properties of Metal/Double-Insulator/Metal Diode. MRS Online Proceedings Library Archive, 2008. **1108**: p. 1108-A09-11 (5 pages).

39. Singh, A., et al., Fabrication and current–voltage characteristics of NiOx/ZnO based MIIM tunnel diode. Applied Surface Science, 2015. **334**: p. 197-204.

40. Schottky, W., Über kalte und warme Elektronenentladungen. Zeitschrift für Physik, 1923. **14**(1): p. 63-106.

41. Millikan, R.A. and C.F. Eyring, Laws Governing the Pulling of Electrons out of Metals by Intense Electrical Fields. Physical Review, 1926. **27**(1): p. 51-67.

42. Millikan, R.A. and C.C. Lauritsen, Relations of Field-Currents to Thermionic-Currents. Proceedings of the National Academy of Sciences of the United States of America, 1928. **14**(1): p. 45-49.

43. Nordheim, L., Zur Theorie der thermischen Emission und der Reflexion von Elektronen an Metallen. Zeitschrift für Physik, 1928. **46**(11): p. 833-855.

44. Fowler, R.H. and L. Nordheim, Electron Emission in Intense Electric Fields. Proceedings of the Royal Society of London A: Mathematical, Physical and Engineering Sciences, 1928. **119**(781): p. 173-181.

45.     Griffiths, D.J., Introduction to Quantum Mechanics. 1995: Prentice Hall. 394.

46.     Merzbacher, E., Quantum Mechanics. 3rd ed. 1998: John Wiley & Songs, Inc.

47.     Simmons, J.G., Generalized Formula for the Electric Tunnel Effect between Similar Electrodes Separated by a Thin Insulating Film. Journal of Applied Physics, 1963. **34**(6): p. 1793-1803.

48.     Simmons, J.G., Electric Tunnel Effect between Dissimilar Electrodes Separated by a Thin Insulating Film. Journal of Applied Physics, 1963. **34**(9): p. 2581-2590.

49.     Hall, E.H., Sommerfeld's Electron-Theory of Metals. Proceedings of the National Academy of Sciences of the United States of America, 1928. **14**(5): p. 370-377.

50.     Brinkman, W.F., R.C. Dynes, and J.M. Rowell, Tunneling Conductance of Asymmetrical Barriers. Journal of Applied Physics, 1970. **41**(5): p. 1915-1921.

51.     Simmons, J.G., Effect of Deep Traps on the Barrier Heights of Metal-Insulator-Metal Tunnel Junctions. Physical Review Letters, 1969. **23**(6): p. 297-300.

52.     Chang, L.L., L. Esaki, and R. Tsu, Resonant tunneling in semiconductor double barriers. Applied Physics Letters, 1974. **24**(12): p. 593-595.

53.     Schulz, P.A. and C.E.T. Gonçalves da Silva, Two-step barrier diodes. Applied Physics Letters, 1988. **52**(12): p. 960-962.

54.     Di Ventra, M., et al., Indented barrier resonant tunneling rectifiers. Journal of Applied Physics, 1996. **80**(7): p. 4174-4176.

55.     Balanis, C.A., Antenna Theory: Analysis and Design. 2005: Wiley-Interscience.

56.     Ratnadurai, R., Development of a Reliable Metal-Insulator-Metal Bilayer Tunnel Junction for Wideband Detectors, in Electrical Engineering. 2012, University of South Florida.

57.     Sharma, A., et al., A carbon nanotube optical rectenna. Nat Nano, 2015. **10**(12): p. 1027-1032.

58.     Krishnan, S., et al., Thin Film Metal-Insulator-Metal Junction for Millimeter Wave Detection. Procedia Chemistry, 2009. **1**(1): p. 409-412.

59.     Gadalla, M.N., M. Abdel-Rahman, and A. Shamim, Design, Optimization and Fabrication of a 28.3 THz Nano-Rectenna for Infrared Detection and Rectification. Scientific Reports, 2014. **4**: p. 4270.

60.     Bean, J.A., A. Weeks, and G.D. Boreman, Performance Optimization of Antenna-Coupled Tunnel Diode Infrared Detectors. IEEE Journal of Quantum Electronics, 2011. **47**(1): p. 126-135.

61.    Alfonso, E., J. Olaya, and G. Cubillos, Thin Film Growth Through Sputtering Technique and Its Applications, Crystallization - Science and Technology, ed. M. Andreeta. 2012: InTech. 578.

62.    Chapman, B., Glow Discharge Processes: Sputtering and Plasma Etching. 1980: Wiley.

63.    Olzick, A., Deposition, Characterization, and Fabrication of a Zinc Oxide Piezoelectric Thin Film Microspeaker Using DC Reactive Sputtering, in Materials Engineering. 2012, California Polytechnic State University.

64.    Knisley, T.J., L.C. Kalutarage, and C.H. Winter, Precursors and chemistry for the atomic layer deposition of metallic first row transition metal films. Coordination Chemistry Reviews, 2013. **257**(23–24): p. 3222-3231.

65.    Leskelä, M. and M. Ritala, Atomic layer deposition (ALD): from precursors to thin film structures. Thin Solid Films, 2002. **409**(1): p. 138-146.

66.    Pinna, N. and M. Knez, eds. Atomic Layer Deposition of Nanostructured Materials. 2011, Wiley-VCH Verlag GmbH & Co. KGaA. 472.

67.    Blanquart, T., et al., Atomic Layer Deposition of Groups 4 and 5 Transition Metal Oxide Thin Films: Focus on Heteroleptic Precursors. Chemical Vapor Deposition, 2014. **20**(7-8-9): p. 189-208.

68.    Miikkulainen, V., et al., Crystallinity of inorganic films grown by atomic layer deposition: Overview and general trends. Journal of Applied Physics, 2013. **113**(2): p. 021301.

69.    George, S.M., Atomic Layer Deposition: An Overview. Chemical Reviews, 2010. **110**(1): p. 111-131.

70.    Argile, C. and G.E. Rhead, Adsorbed layer and thin film growth modes monitored by Auger electron spectroscopy. Surface Science Reports, 1989. **10**(6): p. 277-356.

71.    Wind, R.W., et al., Nucleation period, surface roughness, and oscillations in mass gain per cycle during W atomic layer deposition on Al2O3. Journal of Applied Physics, 2009. **105**(7): p. 074309.

72.    JEOL Ltd. (copyright), http://www.jeol.co.jp.

73.    Azzam, R.M.A. and N.M. Bashara, Ellipsometry and Polarized Light. 1977, New York: North Holland.

74.    Tompkins, H.G. and E.A. Irene, eds. Handbook of Ellipsometry. 2005, William Andrew Publishing: Norwich, NY.

75.    www.uta.edu.

76.    Urban III, F.K., D. Barton, and T. Tiwald, Numerical ellipsometry: Analysis of thin metal layers using n-k-d twisted curve methods with multiple incidence angles. Journal of Vacuum Science & Technology A, 2010. **28**(4): p. 947-952.

77.    Urban III, F.K., D. Barton, and T. Tiwald, Numerical ellipsometry: Analysis of thin metal layers using n–k plane methods with multiple incidence angles. Thin Solid Films, 2009. **518**(5): p. 1411-1414.

78.    Urban III, F.K. and D. Barton, Numerical Ellipsometry: Ellipsometer analysis in the n–k plane for growing films on unknown homogeneous, isotropic substrates and unknown, layered substrates. Thin Solid Films, 2008. **517**(3): p. 1081-1085.

79.    Urban III, F.K. and D. Barton, Numerical ellipsometry: Ellipsometer analysis in the n–k plane for select combinations of metals, semiconductors, and insulators. Thin Solid Films, 2008. **517**(3): p. 1063-1071.

80.    Barton, D. and F.K. Urban III, Ellipsometer analysis in the n-k plane. Thin Solid Films, 2007. **516**: p. 119-127.

81.    Urban III, F.K. and D. Barton, Numerical ellipsometry: Advanced analysis of thin absorbing films in the n–k plane. Thin Solid Films, 2011. **519**(19): p. 6284-6289.

82.    Urban III, F.K. and D. Barton, Numerical ellipsometry: High accuracy modeling of thin absorbing films in the n–k plane. Thin Solid Films, 2014. **562**: p. 49-55.

83.    Urban III, F.K. and D. Barton, Numerical ellipsometry: Examination of growing nickel and rhenium thin films using n–k plane analysis and effective numerical substrates. Thin Solid Films, 2015. **583**: p. 239-244.

84.    Perros, A.C.P. 2015, Aalto University.

85.    Kern, W., The Evolution of Silicon Wafer Cleaning Technology. Journal of The Electrochemical Society, 1990. **137**(6): p. 1887-1892.

86.    Ezema, F.I., A.B.C. Ekwealor, and R.U. Osuji, Optical properties of chemical bath deposited nickel oxide (NiOx) thin films. Superficies y vacío, 2008. **21**: p. 6-10.

87.    Mang, A., K. Reimann, and S. Rübenacke, Band gaps, crystal-field splitting, spin-orbit coupling, and exciton binding energies in ZnO under hydrostatic pressure. Solid State Communications, 1995. **94**(4): p. 251-254.

88.    Li, C., et al., Stoichiometry Control of ZnO Thin Film by Adjusting Working Gas Ratio during Radio Frequency Magnetron Sputtering. Journal of Materials, 2013. **2013**: p. 1-6.

89.    Arbuzov, M.P. and V.G. Chuprina, Metallographic study of the oxidation of Ni3Al-Ni3Nb alloys. Soviet Physics Journal, 1968. **11**(1): p. 11-15.

90.    Arai, H., et al., Structural and Thermal Characteristics of Nickel Dioxide Derived from LiNiO2. Journal of Solid State Chemistry, 2002. **163**(1): p. 340-349.

91. Rykl, D. and J. Bauer, Hydrothermalsynthese von Zinkit. Kristall und Technik, 1968. **3**(3): p. 375-384.

92. Karzel, H., Potzel, U., Potzel, W., Moser, J., Schafer, C., Steiner, M., Peter, M., Kratzer, A., Kalvius, G. M., X-Ray Diffractomer for high pressure and low temperatures Materials Science Forum, 1991. **79-82**.

93. Choi, K.N., et al., Fabrication and Electrical Properties of Metal/Double-Insulator/Metal Diode. MRS Online Proceedings Library, 2008. **1108**: p. null-null.

94. Periasamy, P., et al., Metal-Insulator-Metal Diodes: Role of the Insulator Layer on the Rectification Performance. Advanced Materials, 2013. **25**(9): p. 1301-1308.

95. Rao, K.V. and A. Smakula, Dielectric Properties of Cobalt Oxide, Nickel Oxide, and Their Mixed Crystals. Journal of Applied Physics, 1965. **36**(6): p. 2031-2038.

96. Aiken, J.G. and A.G. Jordan, Electrical transport properties of single crystal nickel oxide. Journal of Physics and Chemistry of Solids, 1968. **29**(12): p. 2153-2167.

97. Alimardani, N., Investigation of Metal-Insulator-Metal (MIM) and Nanolaminate Barrier MIIM Tunnel Devices Fabricated via Atomic Layer Deposition in Electrical and Computer Engineering 2013, Oregon State University p. 182.

98. Maraghechi, P., et al., Observation of resonant tunneling phenomenon in metal-insulator-insulator-insulator-metal electron tunnel devices. Applied Physics Letters, 2012. **100**(11): p. -.

99. Gomer, R., Field emission and field ionization. 1961: Harvard University Press, Cambridge.

100. Houng, M.P., Y.H. Wang, and W.J. Chang, Current transport mechanism in trapped oxides: A generalized trap-assisted tunneling model. Journal of Applied Physics, 1999. **86**(3): p. 1488-1491.

101. Fowler, R.H. and L. Nordheim, Electron Emission in Intense Electric Fields. Proceedings of the Royal Society of London. Series A, 1928. **119**(781): p. 173-181.

102. López-Beltrán, A.M. and A. Mendoza-Galván, The oxidation kinetics of nickel thin films studied by spectroscopic ellipsometry. Thin Solid Films, 2006. **503**(1–2): p. 40-44.

103. Chen, H.-L., Y.-M. Lu, and W.-S. Hwang, Characterization of sputtered NiO thin films. Surface and Coatings Technology, 2005. **198**(1–3): p. 138-142.

104. Jeong, S.W., et al., Effects of annealing temperature on the characteristics of ALD-deposited HfO2 in MIM capacitors. Thin Solid Films, 2006. **515**(2): p. 526-530.

105. Krishnan, S., et al., Thermal stability analysis of thin film Ni–NiOx–Cr tunnel junctions. Thin Solid Films, 2010. **518**(12): p. 3367-3372.

106.    Armstrong, C.M., The truth about terahertz. IEEE Spectrum, 2012. **49**(9): p. 36-41.

107.    Zhu, Z., et al. Optical rectenna solar cells using graphene geometric diodes. in Photovoltaic Specialists Conference (PVSC), 2011 37th IEEE. 2011.

108.    Copyright A2 - PALIK, EDWARD D, in Handbook of Optical Constants of Solids. 1985, Academic Press: Boston. p. iv.

109.    Yu, X., T.J. Marks, and A. Facchetti, Metal oxides for optoelectronic applications. Nat Mater, 2016. **15**(4): p. 383-396.

110.    Hsu, C.-M., et al., Investigation of the High Mobility IGZO Thin Films by Using Co-Sputtering Method. Materials, 2015. **8**(5): p. 2769.

**Appendix A: Process flow**

**I.     Sputtered Devices**

**Step 1:** Substrate Cleaning

RCA 1 Clean: Remove organic

contaminants

Immerse the substrate in 1:1:5 solution of

NH4OH + H2O2+H2O at 75°C for 15

minutes

Oxide removal: Short Immersion of 1:10

HF+H20 to remove the native silicon

dioxide formed on the surface of the

substrate

RCA 2 Clean: Remove Ionic contaminants

Immerse the substrates in 1:1:5 solution of

HCl+H202+H20 at 75°C for 15 minutes.

Rinse it with water and N2 dry.

**Step2**: Thermal Oxidation

Load sample in oxidation tube furnace. Heat

up to 1100°C. Oxygen flow rate corresponds

to 1μm thick oxide growth.

**Step 3:** Photolithography

Layer 1- Contacts and Ground

Spin coat – AZ 5214E Image reversal resist

5 sec at 500 RPM

30 sec at 5000 RPM

Soft bake – Hotplate; T=110°C for 60

seconds

UV Expose – OAI Mask aligner; 4.7 sec at

14.4mW

Reversal bake – Hotplate; T=120°C for 60

seconds

Develop – MIF 300 developer; Immersion

developing at room temperature for 50 sec

Rinse in DI water and N2 dry

Pattern check: Optical Microscope

Thickness check: Dektek Profilometer

**Step 4:** Metal Deposition

Electron Beam Evaporation - Cr and Au

Pressure – <2 μTorr,

Apple Academic Presssec for Cr and 5Å/sec

for Au.

**Step 5:** Lift-Off and Ultrasonic clean

Immerse the substrate in Acetone until all

the unwanted metals peel off from the

substrate. Lift-off aided with ultrasonic bath

Check thickness using Profilometer

**Step 6:** Photolithography

Layer 2- Bottom Electrode and Insulator

Spin coat – AZ 5214E Image reversal resist

5 sec at 500 RPM

30 sec at 5000 RPM

Soft bake – Hotplate; T=110°C for 60 seconds

UV Expose – OAI Mask aligner; 4.7 sec at 14.4mW

Reversal bake – Hotplate; T=120°C for 60 seconds

Develop – MIF 300 developer; Immersion developing at room temperature for 50 sec

Rinse in DI water and N2 dry

Pattern check: Optical Microscope

Thickness check: Dektak Profilometer

**Step 7:** Metal and Insulator Deposition

DC Sputtering - Ni

Base pressure- <2 µTorr Power- 100 W;

Working pressure – 10 mTorr; Sputter time ~10mins

Reactive DC sputtering – NiO

Power- 30W; Working Pressure- 10mTorr;

Sputter Time- 3mins

RF Reactive Compound sputtering- ZnO

Power- 100W; Working Pressure- 10mTorr;

Sputter Time- 72 seconds

**Step 8:** Lift-Off and Ultrasonic clean

Immerse the substrate in Acetone until all the unwanted layers peel off from the substrate. Lift-off aided with ultrasonic bath

Check thickness using Profilometer

**Step 9:** Photolithography

Layer 3- Top Electrode

Spin coat – AZ 5214E Image reversal resist

5 sec at 500 RPM

30 sec at 5000 RPM

Soft bake – Hotplate; T=110°C for 60 seconds

UV Expose – OAI Mask aligner; 4.7 sec at 14.4mW

Reversal bake – Hotplate; T=120°C for 60 seconds

Develop – MIF 300 developer; Immersion developing at room temperature for 50 sec

Rinse in DI water and N2 dry

Pattern check: Optical Microscope

Thickness check: Dektak Profilometer

**Step 10:** Metal Deposition

Thermal Evaporation - Cr and Au

Pressure – <2 µTorr,

Deposition rate –2Å/sec for Cr and 5Å/sec for Au.

**Step 11:** Lift-Off and Ultrasonic clean

Immerse the substrate in Acetone until all the unwanted layers peel off from the substrate. Lift-off aided with ultrasonic bath; Check thickness using Profilometer

## II.    ALD Devices

**Step 1:** Substrate Cleaning

RCA 1 Clean: Remove organic contaminants

Immerse the substrate in 1:1:5 solution of $NH4OH + H2O2+H2O$ at 75°C for 15 minutes

Oxide removal: Short Immersion of 1:10 $HF+H20$ to remove the native silicon dioxide formed on the surface of the substrate

RCA 2 Clean: Remove Ionic contaminants

Immerse the substrates in 1:1:5 solution of $HCl+H202+H20$ at 75°C for 15 minutes. Rinse it with water and N2 dry.

**Step 2:** Thermal Oxidation

Load sample in oxidation tube furnace. Heat up to 1100°C. Oxygen flow rate corresponds to 1µm thick oxide growth.

**Step 3:** Photolithography

Layer 1- Contacts and Ground

Spin coat – AZ 5214E Image reversal resist

5 sec at 500 RPM

30 sec at 5000 RPM

Soft bake – Hotplate; T=110°C for 60 seconds

UV Expose – OAI Mask aligner; 4.7 sec at 14.4mW

Reversal bake – Hotplate; T=120°C for 60 seconds

Develop – MIF 300 developer; Immersion developing at room temperature for 50 sec

Rinse in DI water and N2 dry

Pattern check: Optical Microscope

Thickness check: Dektak Profilometer

**Step 4:** Metal Deposition

Electron Beam Evaporation - Cr and Au

Pressure – <2 µTorr,

Deposition rate –2Å/sec for Cr and 5Å/sec for Au.

**Step 5:** Lift-Off and Ultrasonic clean

Immerse the substrate in Acetone until all the unwanted metals peel off from the substrate. Lift-off aided with ultrasonic bath

Check thickness using Profilometer

**Step 6:** Photolithography

Layer 2- Bottom Electrode and Insulator

Spin coat – AZ 5214E Image reversal resist

5 sec at 500 RPM

30 sec at 5000 RPM

Soft bake – Hotplate; T=110°C for 60 seconds

UV Expose – OAI Mask aligner; 4.7 sec at 14.4mW

Reversal bake – Hotplate; T=120°C for 60 seconds

Develop – MIF 300 developer; Immersion developing at room temperature for 50 sec

Rinse in DI water and N2 dry

Pattern check: Optical Microscope

Thickness check: Dektak Profilometer

**Step 7:** Metal and Insulator Deposition

DC Sputtering - Ni

Base pressure- <2 μTorr Power- 100 W

Working pressure – 10 mTorr

Sputter time ~10mins

Reactive DC sputtering – NiO

Power- 30W; Working Pressure- 10mTorr; Sputter Time- 3mins

ALD Deposition- ZnO

Deposition temperature- 150 °C

DEZ Precursor temperature- 30 °C

Carrier Gas (Flow) - Ar (10sccm)

Working Pressure- 0.5Torr

ALD Cycle:

DEZ Pulse: 250ms; DEZ Purge: 120 s

$H_2O$ Pulse: 150ms; $H_2O$ Purge: 180 s

**Step 8:** Photolithography

Layer 3- To pattern ALD ZnO as layer 3

Spin coat – AZ 5214E Image reversal resist

5 sec at 500 RPM

30 sec at 5000 RPM

Soft bake – Hotplate; T=110°C for 60 seconds

UV Expose – OAI Mask aligner; 4.7 sec at 14.4mW

Reversal bake – Hotplate; T=120°C for 60 seconds

Develop – MIF 300 developer; Immersion developing at room temperature for 50 sec

Rinse in DI water and N2 dry

Pattern check: Optical Microscope

**Step 9:** Etching

Immersing the substrate in acetic acid: phosphoric acid: H2O (1:1:30) The etch rate is approximately 5000 Å/min.

Rinse in DI water and N2 dry

Pattern check: Optical Microscope

**Step 10:** Photolithography

Layer 4- Top Electrode

Spin coat – AZ 5214E Image reversal resist

5 sec at 500 RPM

30 sec at 5000 RPM

Soft bake – Hotplate; T=110°C for 60 seconds

UV Expose – OAI Mask aligner; 4.7 sec at 14.4mW

Reversal bake – Hotplate; T=120°C for 60 seconds

Develop – MIF 300 developer; Immersion developing at room temperature for 50 sec

Rinse in DI water and N2 dry

Pattern check: Optical Microscope

**Step 11:** Metal Deposition

Thermal Evaporation - Cr and Au

Pressure – <2 µTorr,

Deposition rate –2Å/sec for Cr and 5Å/sec for Au.

**Step 12:** Lift-Off and Ultrasonic clean

**Appendix B: LabView program for Atomic Layer Deposition Control System**

I.    **Main Control**
        a.  **Front Panel**

**b. Back Panel**
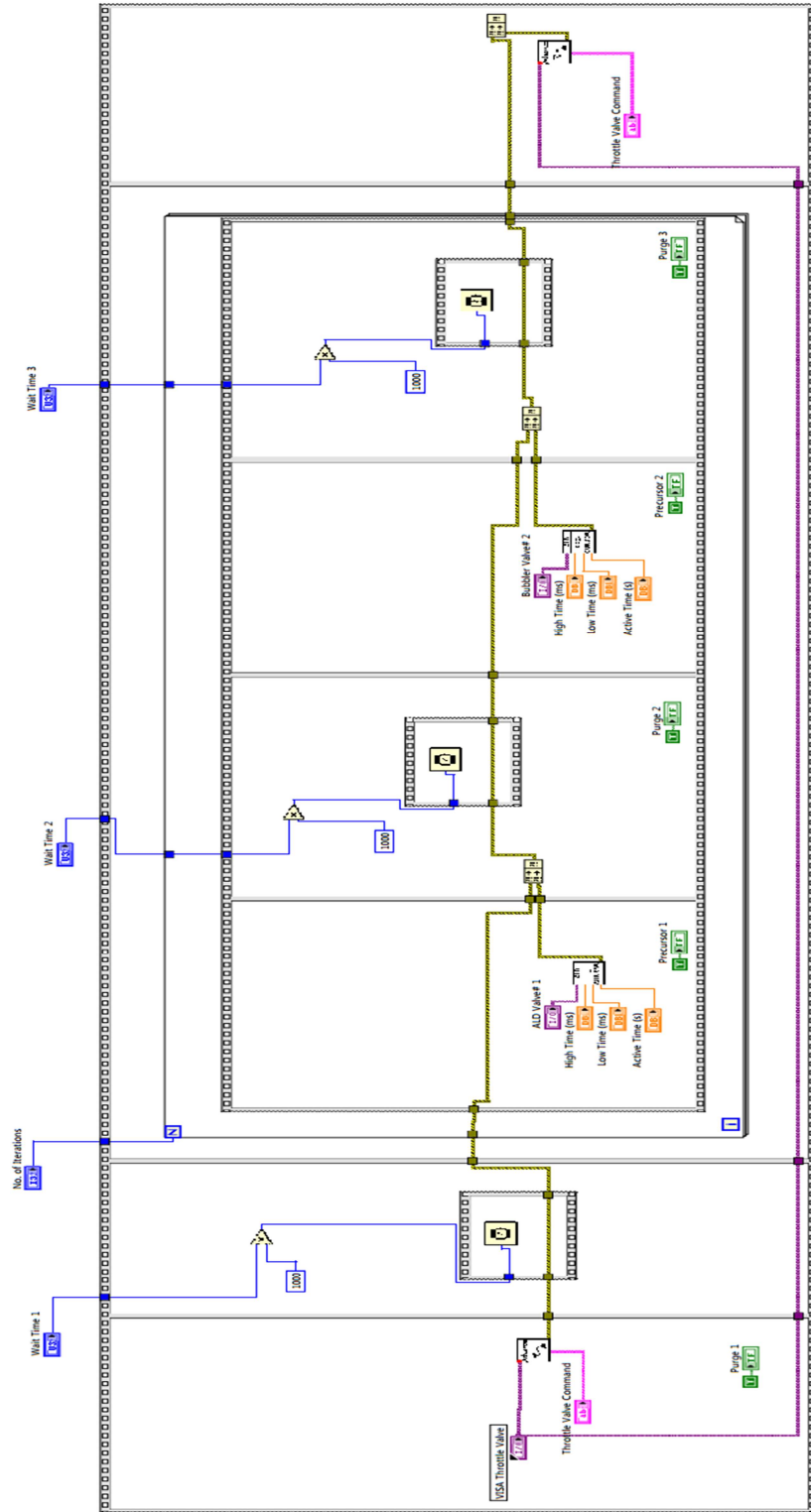
## II. MFC Control
### a. Front Panel

VITA

APARAJITA SINGH
Born, Allahabad, India

2006-2010            Integrated Master of Sciences in Physics (M.Sc. Honors)
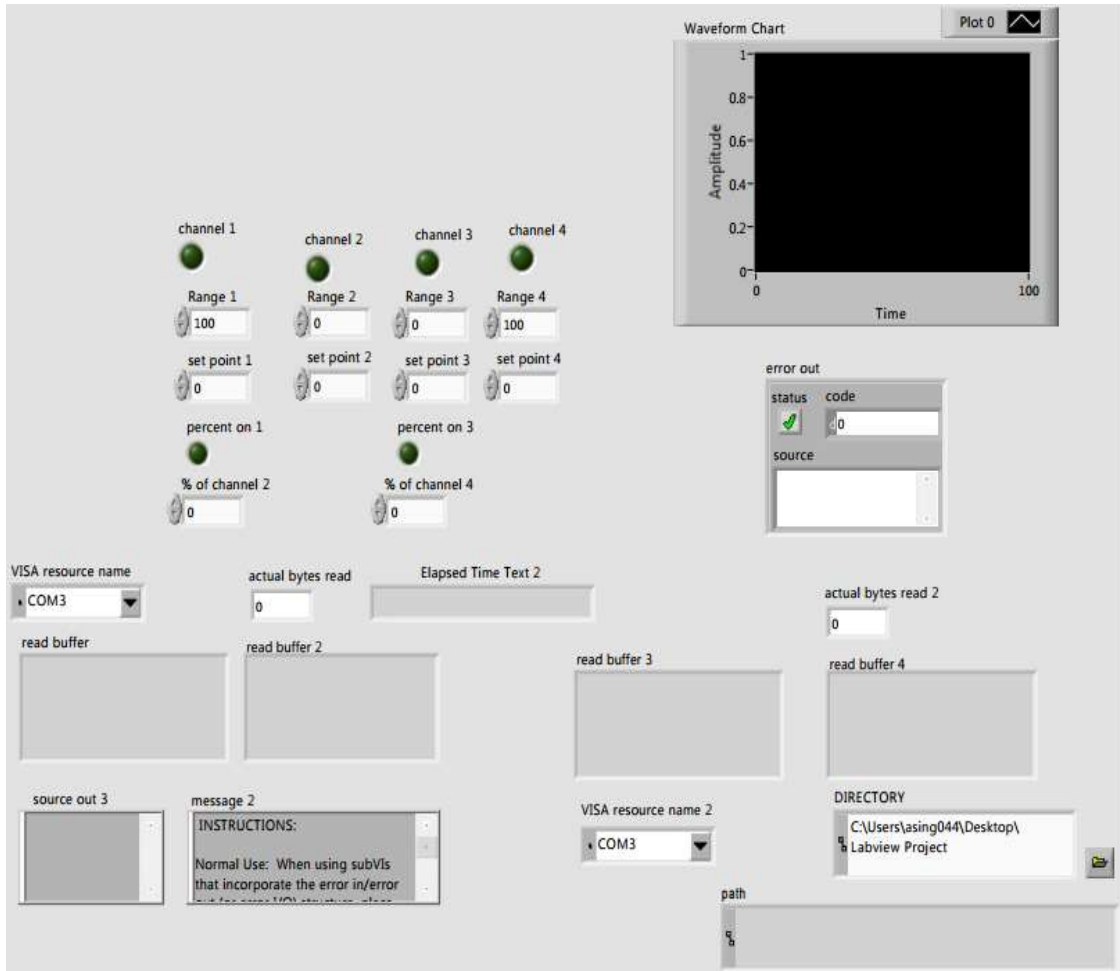                     Birla Institute of Technology & Science-Pilani Campus
                     Pilani, India

2010-2012            Master of Engineering in Microelectronics (M.E.)
                     Birla Institute of Technology & Science-Hyderabad Campus
                     Hyderabad, India

2012-2016            Doctoral Candidate
                     Electrical and Computer Engineering Department
                     Florida International University
                     Miami, Florida

PUBLICATIONS AND PRESENTATIONS

1.  Singh, A., Ratnadurai, R., Kumar, R., Krishnan, S., Emirov, Y., and Bhansali, S. (2015). *Fabrication and current–voltage characteristics of NiOx/ZnO based MIIM tunnel diode*. Applied Surface Science, Vol. 334, pp 197-204.

2.  Singh, A., Pasha, S. K., Manickam, P., and Bhansali, S., (2016). *Single-domain antibody based thermally stable electrochemical immunosensor.* Biosensors and Bioelectronics, Vol 83, pp162-168.

3.  Singh, A., Kaushik, A. K., Kumar, R., Nair, M., and Bhansali, S. (2014). *Electrochemical Sensing of Cortisol: A Recent Update.* Applied Biochemical and Biotechnology, 173(3), pp 1115-1126.

4.  Singh, A., Pasha, S. K., and Bhansali, S. (August, 2016). *Wearable Nano-Enabled Biosensors* in Nanobiotechnology for Sensing Applications: From Lab to Field. Apple Academic Press-CRC Press, ISBN 9781771883283, Edited by Kaushik, A. K. and Dixit, C. K.

5.  Hasnain, A. J., Pasha, S. K., Singh, A., and Bhansali, S. (August, 2016). *Nanobiotechnology: An Abrupt Merger* in Nanobiotechnology for Sensing Applications: From Lab to Field. Apple Academic Press-CRC Press, ISBN 9781771883283, Edited by Kaushik, A. K. and Dixit, C. K.

6.  Singh, A., Ratnadurai, R., Kumar, R., Krishnan, S., and Bhansali, S., (May, 2014). *Fabrication and Current-Voltage characteristics of NiO and NiO/ZnO bilayer dielectrics based MIM Tunnel Junctions*. Poster presented at NANOSMAT (International Conference), Houston, TX.

7. Singh, A., Urban III, FK., and Bhansali, S., (October, 2015). *MIM: Role of Design and Fabrication*. Poster presented at AVS 62nd International Symposium and Exhibition, San Jose.

8. Urban III, FK., Singh, A., Barton, D., and Bhansali, S., (April, 2016). *Numerical Ellipsometry: Analysis of inhomogeneous NiO thin films for metal-insulator-metal tunnel junction diodes*. Paper presented at ICMCTF 43rd International Conference on Metallurgical Coatings and Thin Films, San Diego.

9. Singh, A., Pasha, S. K., and Bhansali, S. (August 28, 2015). *Thermally Stable Electrochemical Sensor With Long Shelf-Life*. Pending Patent, Application Serial No.: 62/211, 172.